

ISSN:1305-130X

e-ISSN:1305-1385

# CELAL BAYAR UNIVERSITY JOURNAL OF SCIENCE



Manisa Celal Bayar Üniversitesi  
Fen Bilimleri Dergisi

2024

VOLUME:20

ISSUE:1



# Journal of Science

Volume: 20, Issue: 1, Year: 2024

## Contact

Manisa Celal Bayar University  
Institute of Natural and Applied Sciences  
Campus of Şehit Prof Dr İlhan Varank 45140 Yunusemre – MANİSA, TÜRKİYE  
Tel: (00 90) 236 201 27 05  
Fax: (00 90) 236 241 21 49  
e-mail: [lee.fendergi@cbu.edu.tr](mailto:lee.fendergi@cbu.edu.tr)  
Web: <https://dergipark.org.tr/tr/pub/cbayarfbe>

“CBU Journal of Science is indexed by ULAKBIM-TUBITAK TR-DIZIN”



ISSN 1305-130X

E-ISSN 1305-1385

CBUJOS is published quarterly at Manisa Celal Bayar University Printing House

“CBU Journal of Science is a refereed scientific journal”



## Celal Bayar University Journal of Science

**Owner** Manisa Celal Bayar University, The Graduate School

**Editor in Chief:** Prof. Dr. Kamil ŞİRİN

**Editor:** Assoc. Prof. Dr. İlker Çetin KESKİN

**Layout Editor & Secretary**

Res. Assist. Gencay TEPE

### Subject Editors

Prof. Dr. Abdullah AKDOĞAN, Pamukkale University, Chemical Engineering

Prof. Dr. Ali DEMİR, Manisa Celal Bayar University, Civil Engineering

Prof. Dr. Fatih KALYONCU, Manisa Celal Bayar University, Biology

Prof. Dr. Kamil ŞİRİN, Manisa Celal Bayar University, Physical Chemistry

Assoc. Prof. Dr. İbrahim Fadıl SOYKÖK, Manisa Celal Bayar University, Mechatronics Engineering

Assoc. Prof. Dr. Serhat ARAS, University of Health Science, Medical Physics

Assoc. Prof. Dr. Sermin ÇAM KAYNAR, Manisa Celal Bayar University, Physics

### International Scientific Advisory Board

Prof. Dr. Arianit REKA; State University of Tetova, Macedonia

Prof. Dr. Tomasz NIEMIEC; Warsaw University of Life Sciences, Poland

Prof. Dr. Alyani ISMAIL; Universiti Putra, Malaysia

Prof. Dr. Iuliana APRODU; Dunarea de Jos University, Romania

Assoc. Prof. Can BAYRAM; University of Illinois, USA

Assoc. Prof. Dr. Johanan Christian PRASANNA; Madras Christian College, South India

Assoc. Prof. Dr. Noureddine ISSAOUI; Université de Monastir, Tunisie.

Assoc. Dr. Edward Albert UECKERMANN; North-West University, South Africa

Assoc. Dr. Zhi-Qiang ZHANG; The University of Auckland, Holland

Assist. Prof. Dr. Young Ki KIM; Pohang University of Science and Technology, South Korea

Assist. Prof. Dr. Mona MIRHEYDARI; Rutgers University, USA

Assist. Prof. Dr. Donatella ALBANESE; Università Degli Studi Di Salerno, Italy

Assist. Prof. Dr. Jinghua JIANG; The University of Memphis, USA

Assist. Prof. Dr. Jens OLDELAND; University of Hamburg, Germany

Dr. Cheng CHENG; Apple Inc., USA

Dr. Sajedeh AFGHAH; Microsoft Corporation, USA

Dr. Jinghua JIANG; The University of Memphis

### National Scientific Advisory Board

Prof. Dr. Mustafa Ersöz; Selçuk University

Prof. Dr. Oğuz Gürsoy; Mehmet Akif University

Prof. Dr. Mehmet Çevik; İzmir Katip Çelebi University

Prof. Dr. Sezgin Çelik; Yıldız Teknik University

Prof. Dr. Osman Dayan; Çanakkale Onsekiz Mart University

Prof. Dr. Serdar İplikçi; Pamukkale University

Prof. Dr. Yasin Üst; Yıldız Teknik University

Prof. Dr. Mahmut Kuş; Konya Teknik University

Prof. Dr. Ertunç Gündüz; Hacettepe University

Prof. Dr. Tülin Aydemir; Manisa Celal Bayar University

Prof. Dr. Sezai Taşkın; Manisa Celal Bayar University

Prof. Dr. Fatma Şaşmaz Ören; Manisa Celal Bayar University

Prof. Dr. Fatih Selimefendigil; Manisa Celal Bayar University

Prof. Dr. Osman Çulha; Manisa Celal Bayar University

Prof. Dr. Ali Konuralp; Manisa Celal Bayar University

Prof. Dr. Erol Akpınar; Abant İzzet Baysal University

Prof. Dr. Ali Demir; Manisa Celal Bayar University

Prof. Dr. Serap Derman; Yıldız Teknik University

Assoc. Prof. Dr. Fatih Doğan; Çanakkale Onsekiz Mart University

Assoc. Prof. Dr. Yeliz Yıldırım; Ege University

Assoc. Prof. Dr. Hayati Mamur; Manisa Celal Bayar University

Assoc. Prof. Dr. Özlem Çağındı; Manisa Celal Bayar University

Assoc. Prof. Dr. Mehmet Söylemez; Adıyaman University

Assoc. Prof. Dr. Nil Mansuroğlu; Ahi Evran University

Assist. Prof. Dr. Zeynep Çipiloğlu Yıldız; Manisa Celal Bayar University



---

## **CBU Journal of Science**

Celal Bayar University Journal of Science (CBUJOS) covers scientific studies in the fields of Engineering and Science and publishes accounts of original research articles concerned with all aspects of experimental and theoretical studies. CBU Journal of Science is a refereed scientific journal published four times annually (March, June, September and December) by Institute of Natural and Applied Sciences of Manisa Celal Bayar University. CBU Journal of Science considers the original research articles written in English for evaluation.

CBU Journal of Science is indexed by TUBİTAK ULAKBİM TR-DİZİN, and also is included in DOAJ, Cite Factor, Journal TOCS, Advanced Science Index and OAJI databases. Digital Object Identifier (DOI) number will be assigned for all the articles being published in CBU Journal of Science.

Instructions for Authors and Article Template can be found on the main page of MCBU Institute of Natural and Applied Sciences (<http://fbe.cbu.edu.tr>)





**Vol: 20, Issue: 1, Year: 2024**

**Contents**

<b><u>Research Article</u></b>	<b><u>Pages</u></b>
A Simple Fluorescence Sensor Based on Merocyanine 540-MnO <sub>2</sub> System to Detect Hypochlorite DOI: 10.18466/cbayarfbe.1384266 Ayşe Merve ŞENOL	1-9
Dosimetric Comparison of The Effects of Different Treatment Plan Techniques on Reduction in Critical Organs in Whole Brain Radiotherapy Application DOI: 10.18466/cbayarfbe.1396284 Hikmettin DEMİR, Gül KANYILMAZ	10-15
Optically Anisotropic Films of Colloidal Nanocrystals/Photoluminescent Dye Doped Polymers DOI: 10.18466/cbayarfbe.1394435 Zeynep DİKMEN	16-22
Electrical Characteristics of Cadmium Sulfide/4-Amino-2-Methyl-Quinoline Heterojunction Structure DOI: 10.18466/cbayarfbe.1396129 Ramazan DEMİR, İsmet KAYA	23-28
Deep Rolling of Al6061-T6 Material and Performance Evaluation with New Type Designed WNMG Formed Rolling Tool DOI: 10.18466/cbayarfbe.1405976 Oktay ADIYAMAN, Feyza AYDIN	29-40
Investigation of Earthquakes in Turkey with Cluster Analysis DOI: 10.18466/cbayarfbe.1416472 Ahmet Murat ŞEN, Zeki YILDIZ	41-48
Comparative Anatomy, Pollen and Seed Morphology of Two Verbascum Varieties (Scrophulariaceae) and Their Taxonomic Significance DOI: 10.18466/cbayarfbe.1433245 Murat KILIÇ, Fatma MUNGAN KILIÇ	49-60
Rhodamine B Hazardous Dye Removal via Adsorption Using Hg(II) Coordination Polymer DOI: 10.18466/cbayarfbe.1413938 Afranur PENDAR, Derya DAVARCI	61-68

# A Simple Fluorescence Sensor Based on Merocyanine 540-MnO<sub>2</sub> System to Detect Hypochlorite

Ayşe Merve Şenol<sup>1\*</sup> 

<sup>1</sup>Program of Medical Laboratory Techniques, Department of Medical Services and Techniques, University of Health Sciences, Istanbul 34668, Türkiye

\*[aysemerve.senol@sbu.edu.tr](mailto:aysemerve.senol@sbu.edu.tr)

\* Orcid No: 0000-0003-3355-8222

Received: 1 November 2023

Accepted: 7 February 2024

DOI: 10.18466/cbayarfbe.1384266

## Abstract

Merocyanine 540 (MC540)- Manganese oxide (MnO<sub>2</sub>) system-based fluorescence sensor is reported as an anion sensor in aqueous solution. MnO<sub>2</sub> was synthesized in the presence of Potassium permanganate (KMnO<sub>4</sub>) and Cetyltrimethylammonium bromide (CTAB) using 3-(N-morpholino) propane sulfonic acid (MOPS) buffer. The formation of MnO<sub>2</sub> was first confirmed by a color change and characterized using X-ray diffraction (XRD), Fourier transform infrared spectroscopy (FTIR), and Ultraviolet-Visible (UV-Vis) absorption spectroscopy techniques. Next, the interaction of MC540 with MnO<sub>2</sub> in aqueous solution was investigated at various conditions by UV-Vis. absorption and fluorescence spectroscopy. The sensing ability of the MC540-MnO<sub>2</sub> was tested to detect hypochlorite (ClO<sup>-</sup>) ion as a “Turn-off” fluorescent sensor. The MC540-MnO<sub>2</sub> revealed to be high selectivity and sensitivity to detect hypochlorite (ClO<sup>-</sup>) ion without being affected by the other thirteen anions. The detection limits for ClO<sup>-</sup> were evaluated in two different concentration ranges and calculated to be 0.14 µM at 0.33-4.46 µM and 0.38 µM at 5.06-14.30 µM, respectively.

**Keywords:** Anionic dye, Anions, Fluorescence quantum yield, Fluorescence quenching, Fluorescence sensor, Hypochlorite, MnO<sub>2</sub>

## 1. Introduction

Organic fluorescent dyes attract the attention of researchers because they have many applications, including organic light-emitting diodes, bioimaging, fluorescence-image, and fluorescence sensors [1-4]. Merocyanine 540 (MC540), a water-soluble organic fluorescent anionic dye, consists of a benzoxazole skeleton and a hexahydropyrimidine-3,5-dione-2-thion ring linked by a conjugated triene (Fig. 1). As with many other fluorescent organic dyes, MC540 has attracted a lot of interest due to its cheap and easy design. The MC540's optical properties could change as a result of interactions with themselves or various semiconductors [5], graphene-based material [6], clays, nanostructures [7], and polyelectrolytes [8]. These changes are determined by absorption and fluorescence spectroscopy [4]. Thus, such newly designed systems can be used in various applications such as solar cells [5], photodynamic therapy[9], chemotherapy [7], and fluorescence sensors [6, 10].

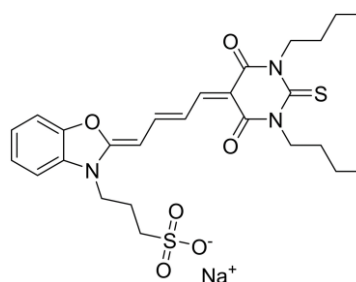


**Figure 1.** Molecular structure of MC540

Manganese oxide (MnO<sub>2</sub>), a prevalent transition metal oxide is absorbed in a wide wavelength range, nontoxic, and readily modified [11]. Moreover, it is one of the most promising conductive materials in various industries such as batteries, water treatment plants, and catalysis due to its low-cost, high-energy density, and ecological compatibility [12]. In addition, when MnO<sub>2</sub> is added to fluorescent materials, it can be subjected to molecular aggregation owing to various molecular interactions (electrostatic, hydrogen bonding, and hydrophobic interactions, etc.) which change the spectral behavior of

the dye [13]. Thus, various new fluorescence probe (dye-MnO<sub>2</sub>) systems can be prepared. In recent years, sensor systems based on molecular aggregation of various fluorescent materials in the presence of MnO<sub>2</sub> have attracted attention. For example; fluorescent perylene-MnO<sub>2</sub> to detect acetylcholinesterase (AChE) [11], fluorescent carbon dots-MnO<sub>2</sub> platform to detect glutathione (GSH) [14, 15], fluorescent polydopamine nanoparticles-MnO<sub>2</sub> to detect alkaline phosphatase [16], fluorescent gold clusters-MnO<sub>2</sub> to detect H<sub>2</sub>O<sub>2</sub> [17], and fluorescent fluorescein dye-MnO<sub>2</sub> to detect H<sub>2</sub>O<sub>2</sub> [18]. However, no fluorescent sensor studies with cyanine-derived dye in the presence of MnO<sub>2</sub> have been found in the literature.

Hypochlorite (ClO<sup>-</sup>) is an important reactive oxygen species that plays a significant role in the biological process of living organisms. ClO<sup>-</sup>, which can be taken directly into our body without being aware of it, is widely used for disinfection and sterilization in swimming pools, tap water, and almost all surfaces. Its deficiency or abundance causes various diseases. Excess ClO<sup>-</sup> can induce kidney, neurological function, cardiovascular system, and cancer, whereas inadequate chlorate can cause many serious diseases as it fails to kill pathogens. Therefore, ClO<sup>-</sup> is very important to detect as quantitative by a practical method [19]. Until now, it has been determined in many methods, including ICP-AES/MS, HPLC, electrochemical, colorimetric, and fluorescence sensors, etc. Among them, the fluorescence sensor technique has drawn attention owing to its high speed, stability, selectivity, and accuracy, as well as economical and practical. In recent years, the design of new fluorescent sensors that can detect various anions and cations, especially in aqueous media, has been of great attention. Therefore, these types of sensors still need to be developed [14].

In the present study, a novel “Turn-off” fluorescence sensor is reported to detect precisely and selectively ClO<sup>-</sup> ions based on the interaction of MC540 with MnO<sub>2</sub> in an aqueous solution. Firstly, MnO<sub>2</sub> was synthesized in the presence of KMnO<sub>4</sub> and CTAB using MOPS buffer. The formation of MnO<sub>2</sub> was first observed by a color change and analyzed by XRD, FTIR, and absorption spectroscopy. Secondly, the interaction of MC540 with

MnO<sub>2</sub> in aqueous solution was investigated using UV-Vis. absorption and fluorescence spectroscopy at various conditions, and the MC540-MnO<sub>2</sub> system as a fluorescent probe was determined. Thirdly, the sensing ability of the MC540-MnO<sub>2</sub> was tested to detect anions as a “Turn-off” fluorescent sensor in the presence of fourteen anions, and LOD values in two different concentration ranges for ClO<sup>-</sup> were calculated. Also, interference tests for ClO<sup>-</sup> were carried out.

## 2. Materials and Methods

### 2.1. Materials

Potassium permanganate (KMnO<sub>4</sub>), Cetyltrimethylammonium bromide (CTAB), MOPS (3-(N-morpholino) propane sulfonic acid) used in MnO<sub>2</sub> synthesis; all anion sodium salts (NaF, NaBr, NaI, NaCl, Na<sub>2</sub>SO<sub>4</sub>, Na<sub>2</sub>CO<sub>3</sub>·H<sub>2</sub>O, Na<sub>3</sub>PO<sub>4</sub>, NaNO<sub>3</sub>, Na<sub>2</sub>S, NaCN, NaSCN, Na<sub>2</sub>C<sub>2</sub>O<sub>4</sub>, CH<sub>3</sub>COONa, and NaClO) used in fluorescence sensor experiments; MC 540 and Rhodamine 101(Rh 101) dyes were purchased from Merck KGaA, Germany. These chemicals were used as received.

### 2.2. Synthesis of MnO<sub>2</sub>

MnO<sub>2</sub> was synthesized in the presence of KMnO<sub>4</sub> and CTAB using MOPS buffer instead of MES(2-(N-morpholino) ethane sulfonic acid) buffer by partially modifying a previous method in the literature [14]. Firstly, KMnO<sub>4</sub> (0.5 g) was dissolved in 0.45 L of distilled water for 30 min. The color of the solution is dark purple. Secondly, CTAB (1.5 g) was added to the solution and mixed for 10 minutes, resulting in a light purple color. Thirdly, MOPS buffer (50 ml at pH 6.5, 0.1 M) was added dropwise over half an hour, and the color of the solution changed from light purple to light brown as MOPS was added. The resulting mixture was stirred for 13 hours and its color was dark brown-black (Fig. 2). The stirring speed is 700 rpm. The obtained MnO<sub>2</sub> solution was centrifuged for 15 min at 9500 rpm. The MnO<sub>2</sub> NPs were collected after centrifugation by washing three times with distilled water and ethanol, respectively.



**Figure 2.** Synthesis of MnO<sub>2</sub>

### 2.3. Instruments

FT-IR spectra were recorded by a Bruker Alpha ATR spectrometer, in the wavenumbers ranging from 400 cm<sup>-1</sup>

to 4000 cm<sup>-1</sup> (Bruker Corporation, U.S.A.). XRD analysis was collected by a PANalytical's X-ray diffractometers in the 2θ range of 10°-90° (Panalytical, Netherlands). Fluorescence spectra were taken on

Agilent Technologies Cary Eclipse Fluorescence Spectrophotometer at an excitation wavelength ( $\lambda_{ex}$ ) of 500 nm (Agilent Technologies, U.S.A.). Absorption spectra were recorded on Shimadzu UV-1800 spectrophotometer (Shimadzu, Japan).

## 2.4. Calculations

The relative fluorescence quantum yields ( $\Phi_f$ ) of the MC540-MnO<sub>2</sub> systems in an aqueous solution were determined by the Parker-Rees method using Rh 101 ( $\Phi_f = 1.0$  in methanol) as reference dye [6].

Also, the ClO<sup>-</sup> sensitivity of the MC540-MnO<sub>2</sub> system is tested by using the Stern-Volmer equation (Eq. 1). The limit of detection (LOD) for ClO<sup>-</sup> was calculated using the slope and standard deviation of this plot.

$$\frac{F_0}{F} = 1 + K_{SV}[Q] \quad (1)$$

Herein,  $K_{SV}$  is the Stern-Volmer constant;  $[Q]$  is a quencher ([ClO<sup>-</sup>] in this study);  $F_0$  and  $F$  are the fluorescence intensity ( $\lambda_{flu}$ ) of the MC540-MnO<sub>2</sub> and MC540-MnO<sub>2</sub>-ClO<sup>-</sup> system, respectively [20].

## 2.5. The procedure to Determine Anions

Initially, stock solutions were prepared for MnO<sub>2</sub> (1 mg/ml) in pure water and MC540 (1x10<sup>-3</sup> M) in methanol. Then, a predetermined quantity of MC540's stock solution was transferred into a glass vial, and its solvent was evaporated using argon gas. The MnO<sub>2</sub> solution, at a specific concentration, was then added to this vial. The solution was left undisturbed for 5 minutes to allow for the interaction between MC540 and MnO<sub>2</sub>. Absorption and fluorescence spectra were recorded. Thus, a specific MC540-MnO<sub>2</sub> system (2.0x10<sup>-6</sup> M MC540 and 2.4 µg/ml MnO<sub>2</sub> in an aqueous solution) was determined for fluorescence sensor studies. Next, various anions (F<sup>-</sup>, Cl<sup>-</sup>, Br<sup>-</sup>, I<sup>-</sup>, S<sup>2-</sup>, NO<sub>3</sub><sup>-</sup>, SO<sub>3</sub><sup>2-</sup>, PO<sub>4</sub><sup>3-</sup>, CO<sub>3</sub><sup>2-</sup>, SCN<sup>-</sup>, CN<sup>-</sup>, AcO<sup>-</sup>, C<sub>2</sub>O<sub>4</sub><sup>2-</sup>, and ClO<sup>-</sup> of 16.7 µM) were added separately to the specific MC540-MnO<sub>2</sub> system. The prepared solutions were mixed, and fluorescence spectra were immediately recorded for each sample.

## 2.6. Interference Tests

Interference tests were performed to determine whether other analytes have a positive or negative effect on the response of the major analyte (ClO<sup>-</sup>) to be determined. The fluorescence responses ( $\lambda_{flu}$ ) of each MC540-MnO<sub>2</sub>-anion (16.7 µM) system were investigated separately in the presence of ClO<sup>-</sup> (16.7 µM).

## 3. Results and discussion

### 3.1. Characterization of MnO<sub>2</sub>

The formation of MnO<sub>2</sub> was primarily manifested with the disappearance of the purple color of potassium

permanganate and its transformation to dark brown-black color (Fig.2). Then, the resulting MnO<sub>2</sub> was characterized using XRD, FTIR, and absorption spectroscopy. The formation of MnO<sub>2</sub> was first confirmed by the XRD pattern (Fig. 3). The faint peak around  $2\theta = 20.63^\circ$  and sharp peaks at  $2\theta = 36.55^\circ$ ,  $65.78^\circ$ , respectively, are reflected (002), (100) and (110) planes of MnO<sub>2</sub> (JCPDS 18-0802) [12, 21-24].

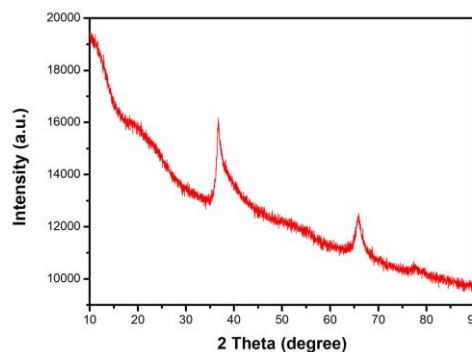


**Figure 3.** XRD pattern of MnO<sub>2</sub>

Secondly, the FTIR spectrum to determine functional groups in the surface of MnO<sub>2</sub> was taken in the wavelength range of 400-4000 cm<sup>-1</sup> (Fig. 4a). In Fig. 4b, the FTIR peaks are more clearly visible. The wide band at 3380 cm<sup>-1</sup> is associated with the vibrational existence in hydroxyl groups. The sharp bands at 2926 and 2853 cm<sup>-1</sup> are due to asymmetric CH<sub>2</sub> stretching vibrations and confirmed that the MnO<sub>2</sub> surface is partially loaded with CTAB. The bands at 1543, 1470, and 1404 cm<sup>-1</sup> are because of a large amount of hydroxyl groups [25].

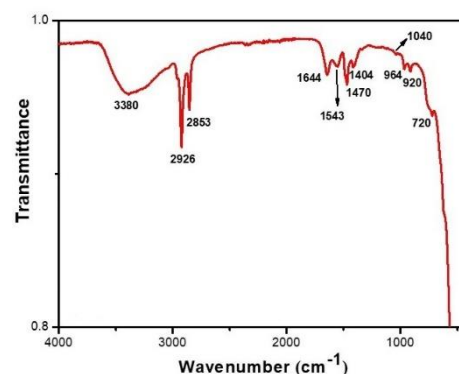


**Figure 4.** The FT-IR spectra of MnO<sub>2</sub>

The band at 1644 cm<sup>-1</sup> is due to O-H bending vibrations combined with Mn atoms. The bands at 1040, 964, and 920 cm<sup>-1</sup> demonstrate vibrations due to the interaction of Mn with OH. Furthermore, the intense shoulder bands at 510 and 476 cm<sup>-1</sup> indicate Mn-O stretching vibrations in the MnO<sub>2</sub> structure [12]. Also, the wide bands at 580 and 720 cm<sup>-1</sup> are due to the stretching and bending vibrations of the oxide group of MnO<sub>2</sub> in the form of O-Mn-O and Mn-O, respectively [25-27]. Consequently, the data

confirm the formation of  $\text{MnO}_2$  NPs and their surface partially loaded with CTAB.

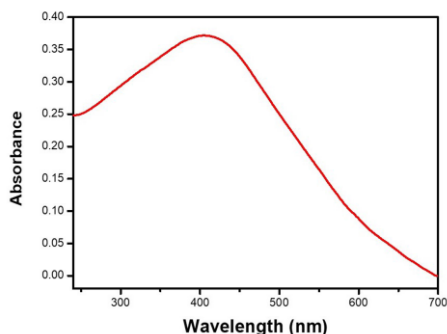


**Figure 5.** Absorbance spectrum of  $\text{MnO}_2$  in aqueous solution (1 mg/ml)

Finally,  $\text{MnO}_2$  aqueous solution was characterized by absorption spectroscopy (Fig. 5). The maximum absorption wavelength ( $\lambda_{\text{abs}}$ ) of  $\text{MnO}_2$ , showing absorption in a wide spectrum range of 240 to 700 nm, was determined as  $\sim 402$  nm [14]. This band is the main characteristic band of  $\text{MnO}_2$  and could be associated with

the electron transition from the valence band to the conduction band [28, 29]. These characterization data are compatible with  $\text{MnO}_2$  structures in the literature.

### 3.2. Photophysical Properties of MC540 in the presence of $\text{MnO}_2$

The effect of  $\text{MnO}_2$  concentration ( $[\text{MnO}_2]$ ) on the molecular behavior of MC540 aqueous dispersion was investigated in the presence of various  $[\text{MnO}_2]$  (0.4 – 3.2  $\mu\text{g/mL}$ ) while MC540 concentration ( $[\text{MC540}]$ ) was kept constant at 2  $\mu\text{M}$ . This effect can be easily understood by comparing it with the MC540's absorption spectrum in pure water.

Here, spectroscopic measurements were performed for 5 min. after mixing  $[\text{MnO}_2]$  with MC540. The absorption spectra of MC540 due to the increasing  $\text{MnO}_2$  concentration are given in Fig. 6a. As seen in Fig. 6a, two intense absorption band ( $\lambda_{\text{abs}}$ ) at 535 nm and 503 nm for MC540 in pure water is assigned to monomeric and H-dimeric MC540 molecules.

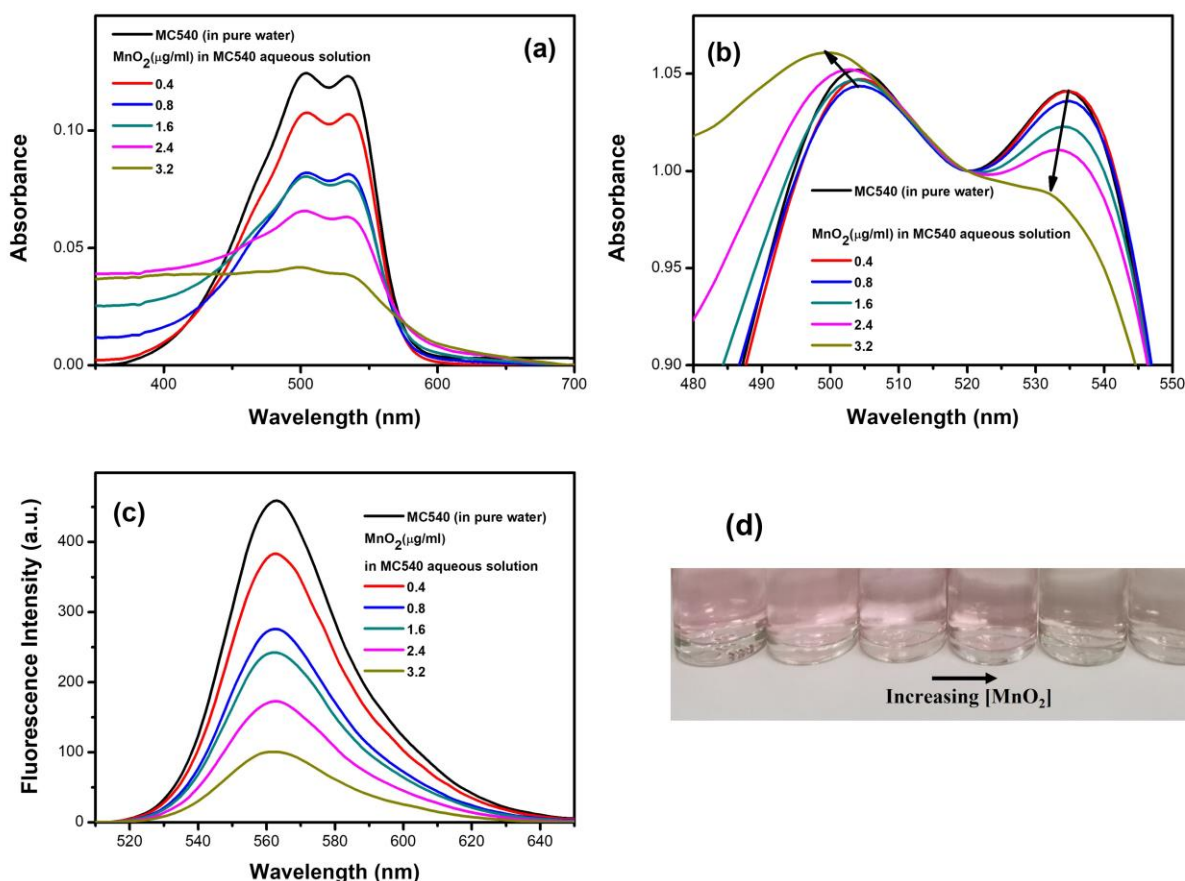


**Figure 6.** (a) The observed form, (b) the normalized form at 520 nm (isosbestic point) of absorption spectra, (c) fluorescence spectra, and (d) a photograph of MC540 (2  $\mu\text{M}$ ) in various  $[\text{MnO}_2]$ . ( $[\text{MnO}_2]$ = 0.04-3.2  $\mu\text{g/mL}$ )

When increasing  $[\text{MnO}_2]$  is added to the MC540 aqueous solution, it is clearly seen that the MC540 dye molecules

aggregate, its monomer band decreases, and its H-dimer band increases (Fig. 6b). Also, it was determined that the

$\lambda_{\text{abs}}$  of each band were shifted to blue and their intensity decreased significantly. This indicates that  $[\text{MnO}_2]$  triggers the dimerization of MC540 by changing its absorption characteristic with strong dipole-dipole interaction in the aqueous medium. Dimers (H-dimer) with low aggregation numbers are commonly referred to as H-aggregates [6]. They are non-fluorescent. For this reason, the effect of  $[\text{MnO}_2]$  on the fluorescence properties of MC540 in aqueous dispersion was investigated in the same way as Fig. 6a (Fig. 6c). In Fig. 6c, the effect of  $[\text{MnO}_2]$  on the fluorescence of MC540 can be explained by comparing it with the fluorescence spectrum of MC540 aqueous solution. As seen in Fig. 6c, the  $\lambda_{\text{flu}}$  of MC540 ( $2.0 \times 10^{-6}$  M) in pure water is  $\sim 562$  nm. The  $\lambda_{\text{flu}}$  of MC540 is blue-shifted to  $\sim 1$  nm, and the fluorescence intensity of the dye decreased due to the nonradiative transitions by increasing  $[\text{MnO}_2]$  in the aqueous dispersions. In addition, the MC540's color change observed with increasing  $[\text{MnO}_2]$  is given in Fig. 6d.

Furthermore, the effect of MC540 concentration ( $[\text{MC540}]$ ) was investigated by absorption and fluorescence spectroscopy in various  $[\text{MC540}]$  in the range of  $1 \mu\text{M}$ - $10 \mu\text{M}$  in the presence of  $\text{MnO}_2$  of  $2.4 \mu\text{g/mL}$ . Absorption spectra of these solutions are given in Fig. 7a. Herein, it is seen that the H-dimer band of the MC540( $1 \mu\text{M}$ ) solution containing  $\text{MnO}_2$  is at  $\sim 499$  nm,

while its monomer band is at 530 nm. When the  $[\text{MC540}]$  was gradually increased, it was determined that its monomeric band red-shifted to 535 nm, while its H-dimer band red-shifted to 503 nm (Fig. 7b). The red shift in the prominent absorption bands of MC540 is due to changes in viscosity, polarity, hydrogen bonding property, and some physical interactions. Moreover, fluorescence spectra of these solutions were taken in the same concentrations (Fig. 7c). In Fig. 7c, when the increase of  $[\text{MC540}]$ , the  $\lambda_{\text{flu}}$  is red-shifted to about 1 nm, and the fluorescence intensity increases. This can be explained by the decrease in  $[\text{MnO}_2]$  that could interact with MC540 when the  $[\text{MC540}]$  increased. Thus, MC540, which is a monomer-dimer equilibrium, shifted to monomer form with increasing MC540 concentration. The MC540's color change observed with increasing  $[\text{MC540}]$  in the presence of  $\text{MnO}_2$  ( $2.4 \mu\text{g/mL}$ ) is given in Fig. 7d. In addition, the fluorescence quantum yields of MC540 at increasing  $\text{MnO}_2$  and dye concentrations were calculated using their absorption and fluorescence data and are given in Table 1. When Table 1 was examined, with the increase of  $\text{MnO}_2$  concentration in MC540 solution, its fluorescence quantum efficiency was seen to be decreased, and thus H-dimerization increased. This is compatible with other data and has proven the interaction of MC540 and  $\text{MnO}_2$  in aqueous solution.

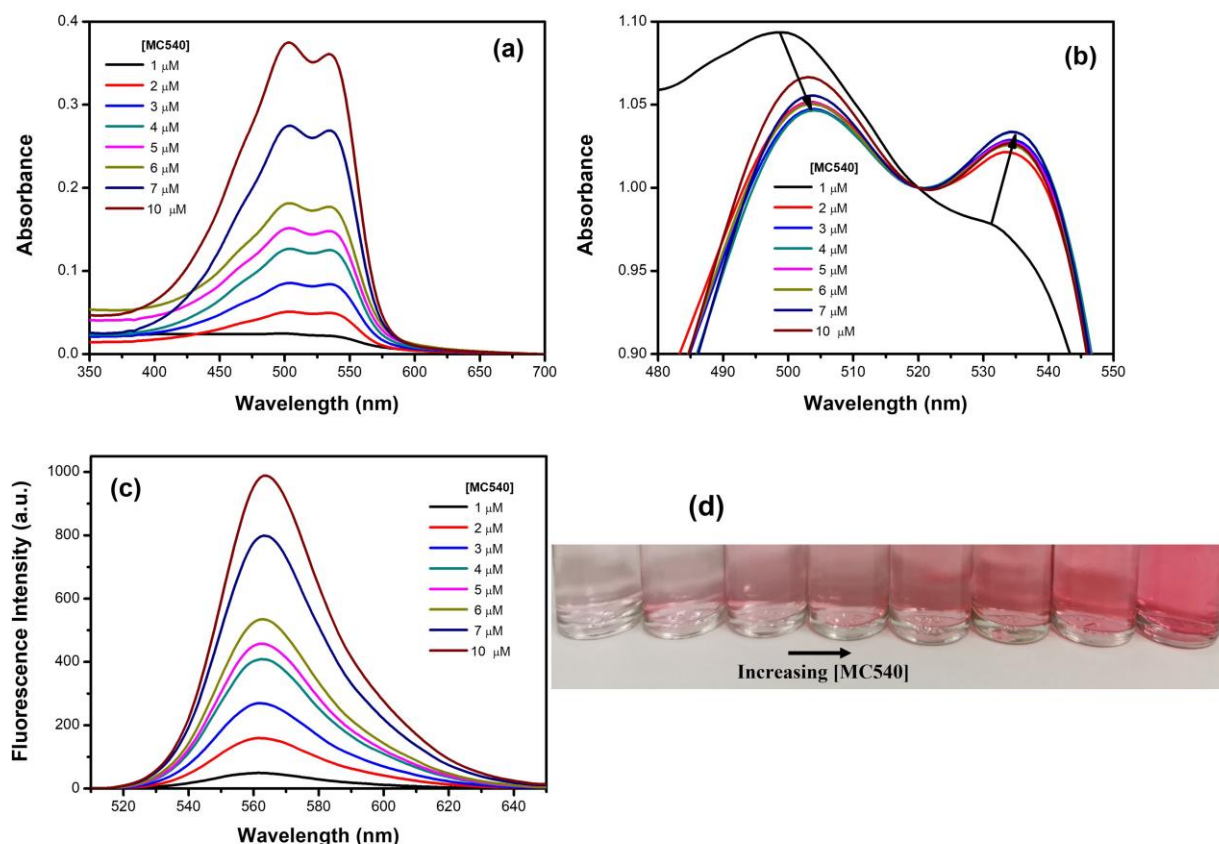


**Figure 7.** (a) The observed form, (b) the normalized form absorption spectra, (c) the fluorescence spectra, and (d) a photograph of various MC540 solutions containing  $\text{MnO}_2$  ( $2.4 \mu\text{g/mL}$ ). ( $[\text{MC540}] = 1$ - $10 \mu\text{M}$ )

**Table 1.** Fluorescence quantum yields ( $\Phi_f$ ) of MC540 in aqueous solution in increasing  $\text{MnO}_2$  and MC540 concentrations

	$\Phi_f$
[MC540]	
$2 \times 10^{-6}$ M	7.50
[ $\text{MnO}_2$ ]( $\mu\text{g/mL}$ ) ([MC540= $2 \times 10^{-6}$ M])	
0.4	7.15
0.8	6.51
1.6	5.86
2.4	4.97
3.2	4.43
[MC540](M) ([ $\text{MnO}_2$ =2.4 $\mu\text{g/mL}$ ])	
$1 \times 10^{-6}$	3.10
$2 \times 10^{-6}$	4.97
$3 \times 10^{-6}$	5.20
$4 \times 10^{-6}$	5.60
$5 \times 10^{-6}$	5.38
$6 \times 10^{-6}$	5.41
$7 \times 10^{-6}$	5.86
$10 \times 10^{-6}$	5.84

It is decided to use the MC540- $\text{MnO}_2$  system containing [MC540] ( $2 \times 10^{-6}$  M) and [ $\text{MnO}_2$ ] (2.4  $\mu\text{g/mL}$ ), in which MC540 partially dimerized, as a fluorescence probe to detect anions. UV-Vis. absorption and fluorescence spectra for  $\text{MnO}_2$ , MC540, and  $\text{MnO}_2$ -MC540 systems at the determined concentrations in aqueous solution are comparatively given in Fig. 8a and 8b, respectively.

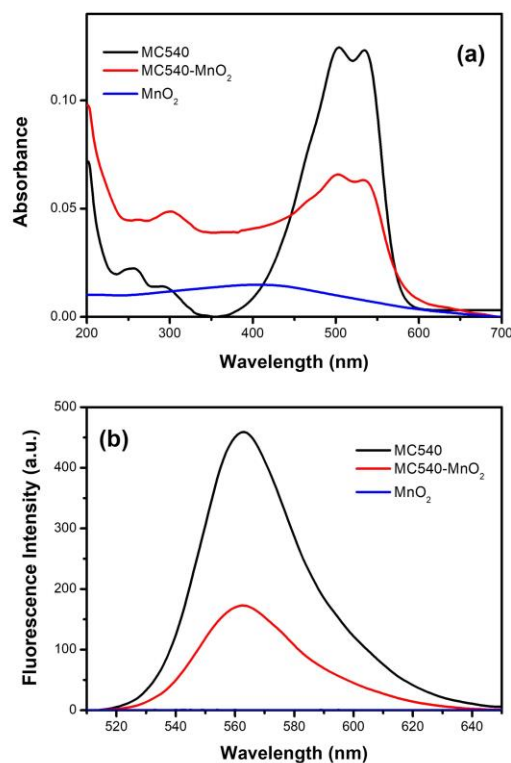


**Figure 8.** (a) UV-Vis. absorption and (b) fluorescence spectra for  $\text{MnO}_2$ , MC540, and MC540- $\text{MnO}_2$  systems

### 3. 3. Hypochlorite Detection Performance of MC540- $\text{MnO}_2$

The fluorescence spectra of the MC540- $\text{MnO}_2$  aqueous solution were separately taken in the presence of 14 different anions ( $\text{F}^-$ ,  $\text{Br}^-$ ,  $\text{I}^-$ ,  $\text{Cl}^-$ ,  $\text{SO}_4^{2-}$ ,  $\text{CO}_3^{2-}$ ,  $\text{PO}_4^{3-}$ ,  $\text{NO}_3^-$ ,  $\text{S}^{2-}$ ,  $\text{CN}^-$ ,  $\text{SCN}^-$ ,  $\text{C}_2\text{O}_4^{2-}$ ,  $\text{CH}_3\text{COO}^-$  ( $\text{AcO}^-$ ), and  $\text{ClO}^-$ ) to determine of MC540- $\text{MnO}_2$ 's selectivity (Fig. 9a). As seen in Fig. 9a, it determined that  $\text{ClO}^-$  ions quenched the fluorescence intensity of MC540- $\text{MnO}_2$ , whereas other anions had little or no effect. Also, the  $\lambda_{\text{flu}}$  was blue-shifted from about  $\sim 18$  nm. This could be due to the formation of a non-radiative complex due to the high affinity of the MC540- $\text{MnO}_2$  fluorescence probe for  $\text{ClO}^-$  ions. The  $\text{ClO}^-$  selectivity of MC540- $\text{MnO}_2$  is more clearly shown in the histogram of  $(F_0-F)/F_0$  vs. anions, as presented in Fig. 9b. Here,  $(F_0-F)/F_0=1$  indicates that the fluorescence intensity of MC540- $\text{MnO}_2$  is completely quenched. When the black columns in Fig. 9b were examined, it was determined that MC540- $\text{MnO}_2$ 's fluorescence intensity in the presence of only  $\text{ClO}^-$  ( $\frac{F_0-F}{F_0} \cong 1$ ) was almost completely quenched. Moreover, interference tests were performed to determine  $\text{ClO}^-$ , and fluorescence responses of MC540- $\text{MnO}_2$  in the presence of other 13 anions were separately recorded (red columns in Fig. 9b). Thus,  $\text{ClO}^-$  ions were proven to be detected independently of the other 13 anions.

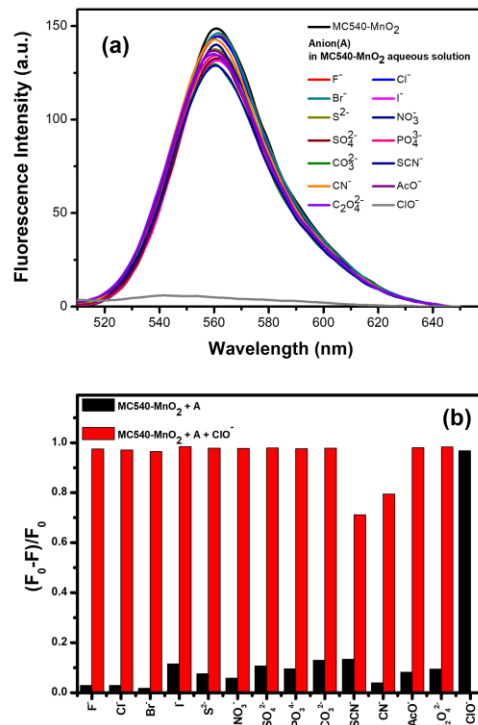


**Figure 9.** (a) Fluorescence spectra, and (b) histograms of  $(F_0-F)/F_0$  vs. anions of MC540- $\text{MnO}_2$  in the absence and presence of various anions, and their  $\text{ClO}^-$  interference histograms ( $\lambda_{\text{ex}} = 500$  nm,  $[A]=16.7$   $\mu\text{M}$ , where  $F_0$  and  $F$

are the fluorescence intensities of the MC540-MnO<sub>2</sub> in the absence and presence of anions, respectively).

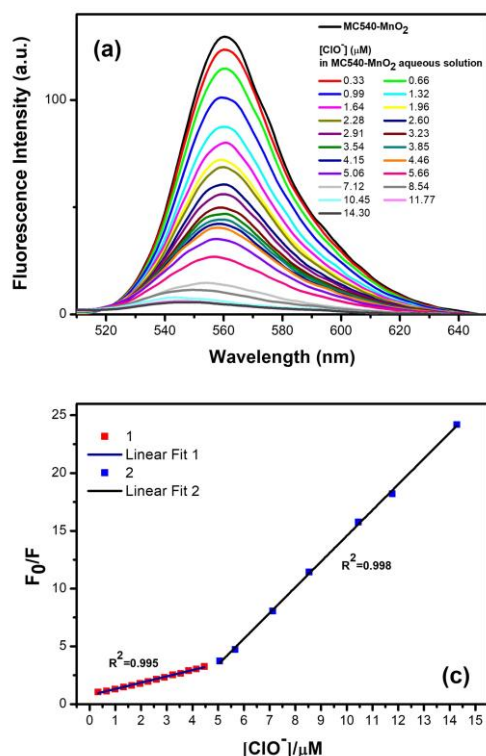


**Figure 10.** (a) Fluorescence spectra of MC540-MnO<sub>2</sub> system in the presence of various [ClO<sup>-</sup>], and (b) plot of F<sub>0</sub>/F vs. [ClO<sup>-</sup>] in the range of 0.33 µM to 14.30 µM.

To test the sensitivity of the MC540-MnO<sub>2</sub> system, the fluorescence spectra of MC540-MnO<sub>2</sub> in ClO<sup>-</sup> concentration ([ClO<sup>-</sup>]) in the range of 0.33 µM-14.30 µM were recorded (Fig. 10a). In Fig. 10a, it is seen that the fluorescence intensity of MC540-MnO<sub>2</sub> was sensitive to ClO<sup>-</sup> ions and decreased with increasing [ClO<sup>-</sup>]. In addition, according to Eq. 1, F<sub>0</sub>/F vs. [ClO<sup>-</sup>] graph was plotted (Fig. 10b). This graph was non-linear. Therefore, the LOD values were separately determined at two concentration ranges where the F/F<sub>0</sub> vs. [ClO<sup>-</sup>] plot showed high linearity. Each concentration range is indicated in a different color in Fig. 10b, and the correlation coefficients (R<sup>2</sup>) are given in the graph. The LOD values were calculated as 0.14 µM, and 0.38 µM at [ClO<sup>-</sup>] in the range of 0.33-4.46 µM (1, red) and 5.06-14.30 µM (2, blue), respectively. This indicates that even low concentrations of hypochlorite can be easily detected. Table 2 summarizes the detected ion/molecules, solvent, linear range and LOD values for some fluorescence probes developed for ClO<sup>-</sup> detection in the literature. In this study, it can be seen that the performance values found for ClO<sup>-</sup> are better compared to the literature given in Table 2. Consequently, it is determined that the MnO<sub>2</sub>-MC540 fluorescence probe in pure water could be a highly accurate and selective "Turn-off" Fluorescence sensor to determine ClO<sup>-</sup>.

**Table 2.** Various fluorescence probes and their detected ions/molecules in the literature.

Fluorescence probe	Detected ion/molecule	Solvent	Linear range	LOD (µM)	Ref
A coumarin–dihydroperimidine dye	ClO <sup>-</sup>	Water/MeCN	0-100 µM	3.3 µM	[30]
3-Formyl-10-Methylphenothiazine	ClO <sup>-</sup>	Water	0-100 µM	0.45 µM	[31]
Red emissive carbon dots	ClO <sup>-</sup>	Ethanol	0-300 µM	4.95 µM	[32]
N', N'''-((1Z,1'Z)-[2,2'-bithiophene]-5,5'-diylbis(methanylylidene)) bis(furan-2-carbohydrazide)	ClO <sup>-</sup>	Bis-tris buffer	-	4.2 µM	[33]
Phenothiazine-coumarin platform	ClO <sup>-</sup>	PBS/ Triton X-100	0-6.5 equiv.	0.321 µM	[34]
MC540-MnO <sub>2</sub>	ClO <sup>-</sup>	Water	(1) 0.33-4.46 µM (2) 5.06-14.30 µM	(1) 0.14 µM (2) 0.38 µM	This study

#### 4. Conclusions

A new "Turn-off" fluorescence sensor is reported to determine precisely and selectively ClO<sup>-</sup> based on the interaction of MC540 with MnO<sub>2</sub> in an aqueous solution. Firstly, MnO<sub>2</sub> was synthesized in the presence of KMnO<sub>4</sub> and CTAB using MOPS buffer. The formation of MnO<sub>2</sub> was observed by a color change, and characterized by XRD, FTIR, and absorption spectroscopy. Analysis results showed that it was successfully synthesized. Next, the interaction of MC540 with MnO<sub>2</sub> in various [MnO<sub>2</sub>] and [MC540] was studied using UV-Vis. absorption and

fluorescence spectroscopy. The MC540-MnO<sub>2</sub> system containing [MC540] (2x10<sup>-6</sup> M) and [MnO<sub>2</sub>](2.4 µg/ml), in which MC540 partially dimerized system, was determined as a fluorescence probe. The sensing ability of the MC540-MnO<sub>2</sub> was separately recorded for their fluorescence responses in the presence of 14 different anions. MC540-MnO<sub>2</sub>'s fluorescence intensity was effectively quenched in the presence of only ClO<sup>-</sup>. LOD values for ClO<sup>-</sup> were evaluated at linear concentration intervals of F<sub>0</sub>/F vs. [ClO<sup>-</sup>] plot, and calculated to be 0.14 µM at 0.33-4.46 µM and 0.38 µM at 5.06-14.30 µM, respectively. Interference experiments also showed that

$\text{ClO}^-$  could be determined independently of other anions. Thus, it is determined that the  $\text{MnO}_2$ -MC540 fluorescence probe in pure water could be a fast and easily applicable, highly accurate, and selective "Turn-off" Fluorescence sensor to determine  $\text{ClO}^-$ .

### Author's Contributions

**Ayşe Merve Şenol:** Designed the investigation, performed the experiments, and wrote the manuscript.

### Ethics

There are no ethical issues after the publication of this manuscript.

### References

- [1]. Traven, VF, Cheptsov, DA, and Lodeiro, C. 2023. Control of Fluorescence of Organic Dyes in the Solid-State by Supramolecular Interactions. *J Fluoresc*; 33: 799-847.
- [2]. Korshunov, VM, Mikhailov, MS, Chmovzh, TN, Vashchenko, AA, Gudim, NS, Mikhilchenko, LV, Taydakov, IV, and Rakitin, OA. 2021. Novel D-A-D Fluorescent Dyes Based on 9-(p-Tolyl)-2,3,4,4a,9,9a-hexahydro-1H-carbazole as a Donor Unit for Solution-Processed Organic Light-Emitting-Diodes. *Molecules*; 26: 2872.
- [3]. Tian, Y, Yin, D, and Yan, L. 2023. J-aggregation strategy of organic dyes for near-infrared bioimaging and fluorescent image-guided phototherapy. *Wiley Interdiscip Rev Nanomed Nanobiotechnol*; 15: e1831.
- [4]. Saleem, M, Rafiq, M, Hanif, M, Shaheen, MA, and Seo, S-Y. 2017. A Brief Review on Fluorescent Copper Sensor Based on Conjugated Organic Dyes. *Journal of Fluorescence*; 28: 97-165.
- [5]. Jabeen, U, Shah, SM, Aamir, M, and Ahmad, I. 2021. Grafting and co-grafting of dyes on Cd-doped ZnS nanocrystals and their application on dye-sensitized solar cells. *Bulletin of Materials Science*; 44: 1-9.
- [6]. Bayraktutan, T and Meral, K. 2016. Merocyanine 540 adsorbed on polyethylenimine-functionalized graphene oxide nanocomposites as a turn-on fluorescent sensor for bovine serum albumin. *Phys Chem Chem Phys*; 18: 23400-23406.
- [7]. Su, Y, Mao, Y, Wu, S, Liu, L, and Wen, S. 2023. Silica Coated Upconversion Nanoplatfor for Ag-Based Chemo-/Photodynamic Therapy against Drug-Resistant Bacteria. *ACS Applied Nano Materials*; 6: 8685-8694.
- [8]. Bayraktutan, T, Onganer, Y, and Meral, K. 2016. Polyelectrolyte-induced H-aggregation of Merocyanine 540 and its application in metal ions detection as a colorimetric sensor. *Sensors and Actuators B: Chemical*; 226: 52-61.
- [9]. Wang, H, Liu, Z, Wang, S, Dong, C, Gong, X, Zhao, P, and Chang, J. 2014. MC540 and upconverting nanocrystal coloaded polymeric liposome for near-infrared light-triggered photodynamic therapy and cell fluorescent imaging. *ACS Appl Mater Interfaces*; 6: 3219-25.
- [10]. Valeur, B. 2002. Molecular Fluorescence Principles and Applications; Wiley-Vch Verlag GmbH, Weinheim.
- [11]. Zhang, Y, Zhang, C, Chen, J, Li, Y, Yang, M, Zhou, H, Shahzad, SA, Qi, H, Yu, C, and Jiang, S. 2017. A real-time fluorescence turn-on assay for acetylcholinesterase activity based on the controlled release of a perylene probe from  $\text{MnO}_2$  nanosheets. *Journal of Materials Chemistry C*; 5: 4691-4694.
- [12]. Mylarappa, M, Lakshmi, VV, Mahesh, KRV, Nagaswarupa, HP, and Raghavendra, N. 2016. A facile hydrothermal recovery of nano sealed  $\text{MnO}_2$  particle from waste batteries: An advanced material for electrochemical and environmental applications. *International Conference on Advances in Materials and Manufacturing Applications (Iconamma-2016)*; 149: 12178.
- [13]. Şenol, AM, Metin, Ö, and Onganer, Y. 2019. A facile route for the preparation of silver nanoparticles-graphene oxide nanocomposites and their interactions with pyronin Y dye molecules. *Dyes and Pigments*; 162: 926-933.
- [14]. Xu, Y, Chen, X, Chai, R, Xing, C, Li, H, and Yin, XB. 2016. A magnetic/fluorometric bimodal sensor based on a carbon dots- $\text{MnO}_2$  platform for glutathione detection. *Nanoscale*; 8: 13414-21.
- [15]. Wang, Y, Jiang, K, Zhu, J, Zhang, L, and Lin, H. 2015. A FRET-based carbon dot- $\text{MnO}_2$  nanosheet architecture for glutathione sensing in human whole blood samples. *Chem Commun (Camb)*; 51: 12748-51.
- [16]. Xiao, T, Sun, J, Zhao, J, Wang, S, Liu, G, and Yang, X. 2018. FRET Effect between Fluorescent Polydopamine Nanoparticles and  $\text{MnO}_2$  Nanosheets and Its Application for Sensitive Sensing of Alkaline Phosphatase. *ACS Appl Mater Interfaces*; 10: 6560-6569.
- [17]. Sheng, J, Jiang, X, Wang, L, Yang, M, and Liu, YN. 2018. Biomimetic Mineralization Guided One-Pot Preparation of Gold Clusters Anchored Two-Dimensional  $\text{MnO}_2$  Nanosheets for Fluorometric/Magnetic Bimodal Sensing. *Anal Chem*; 90: 2926-2932.
- [18]. Ali, HRH, Hassan, AI, Hassan, YF, and El-Wekil, MM. 2020. One pot fabrication of fluorescein functionalized manganese dioxide for fluorescence "Turn OFF-ON" sensing of hydrogen peroxide in water and cosmetic samples. *RSC Adv*; 10: 17506-17514.
- [19]. Zhou, B, Han, Y, Liu, J, Cheng, K, Dong, M, and Tang, X. 2023. Design and Synthesis of Novel Fluorescent Probe Based on Cyanobiphenyl and its Application in Detection of Hypochlorite. *J Fluoresc*; 33: 575-586.
- [20]. Şenol, AM and Bozkurt, E. 2023. A green "off-on" fluorescent sensor to detect  $\text{Fe}^{3+}$  and ATP using synthesized carbon dots from Rosehip. *Research on Chemical Intermediates*; 49: 2175-2189.
- [21]. Zhang, X, Miao, W, Li, C, Sun, X, Wang, K, and Ma, Y. 2015. Microwave-assisted rapid synthesis of birnessite-type  $\text{MnO}_2$  nanoparticles for high performance supercapacitor applications. *Materials Research Bulletin*; 71: 111-115.
- [22]. Zhou, J, Yu, L, Liu, W, Zhang, X, Mu, W, Du, X, Zhang, Z, and Deng, Y. 2015. High Performance All-solid Supercapacitors Based on the Network of Ultralong Manganese dioxide/Polyaniline Coaxial Nanowires. *Sci Rep*; 5: 17858.
- [23]. Agrawal, R, Adelowo, E, Baboukani, AR, Villegas, MF, Henriques, A, and Wang, C. 2017. Electrostatic Spray Deposition-Based Manganese Oxide Films-From Pseudocapacitive Charge Storage Materials to Three-Dimensional Microelectrode Integrands. *Nanomaterials (Basel)*; 7: 198.
- [24]. Dinh, V-P, Le, N-C, Nguyen, T-P-T, and Nguyen, N-T. 2016. Synthesis of a  $\text{MnO}_2$  Nanomaterial from a Precursory- $\text{MnO}_2$ : Characterization and Comparative Adsorption of  $\text{Pb}(\text{II})$  and  $\text{Fe}(\text{III})$ . *Journal of Chemistry*; 2016: 1-9.
- [25]. Mahmoud, ME, Khalifa, MA, El-Mallah, NM, Hassouba, HM, and Nabil, GM. 2021. Performance of  $\text{MnO}_2$  nanoparticles-

- coated cationic CTAB for detoxification and decolorization of sulfonated remazol red and reactive black 5 dyes from water. *International Journal of Environmental Science and Technology*; 19: 141-158.
- [26]. Said, MI, Rageh, AH, and Abdel-Aal, FAM. 2018. Fabrication of novel electrochemical sensors based on modification with different polymorphs of MnO(2) nanoparticles. Application to furosemide analysis in pharmaceutical and urine samples. *RSC Adv*; 8: 18698-18713.
- [27]. Xie, Y, Yu, Y, Gong, X, Guo, Y, Guo, Y, Wang, Y, and Lu, G. 2015. Effect of the crystal plane figure on the catalytic performance of MnO<sub>2</sub> for the total oxidation of propane. *CrystEngComm*; 17: 3005-3014.
- [28]. Sorouri, F, Gholibegloo, E, Mortezaazadeh, T, Kiani, S, Foroumadi, A, Firoozpour, L, and Khoobi, M. 2023. Tannic acid-mediated synthesis of flower-like mesoporous MnO(2) nanostructures as T(1)-T(2) dual-modal MRI contrast agents and dual-enzyme mimetic agents. *Sci Rep*; 13: 14606.
- [29]. Godlaveeti, SK, Komatikunta, VK, Somala, AR, Sangaraju, S, Alshgari, RA, Mushab, MSS, Maseed, H, and Nagireddy, RR. 2023. Different Phase and Morphology of the MnO<sub>2</sub> on Various Substrates and Electrolytes for Electrochemical Performance. *Journal of Cluster Science*; 34: 2725-2736.
- [30]. Shiraishi, Y, Yamada, C, and Hirai, T. 2019. A coumarin-dihydroperimidine dye as a fluorescent chemosensor for hypochlorite in 99% water. *RSC Adv*; 9: 28636-28641.
- [31]. Song, H, Zhou, Y, Xu, C, Wang, X, Zhang, J, Wang, Y, Liu, X, Guo, M, and Peng, X. 2019. A dual-function fluorescent probe: Sensitive detection of water content in commercial products and rapid detection of hypochlorite with a large Stokes shift. *Dyes and Pigments*; 162: 160-167.
- [32]. Zhu, Y, Li, G, Li, W, Luo, X, Hu, Z, and Wu, F. 2023. Facile synthesis of efficient red-emissive carbon quantum dots as a multifunctional platform for biosensing and bioimaging. *Dyes and Pigments*; 215: 111303.
- [33]. Kim, PA, Choe, D, So, H, Park, S, Suh, B, Jeong, S, Kim, KT, Kim, C, and Harrison, RG. 2021. A selective fluorescence sensor for hypochlorite used for the detection of hypochlorite in zebrafish. *Spectrochim Acta A Mol Biomol Spectrosc*; 261: 120059.
- [34]. Wang, W, Ning, J-Y, Liu, J-T, Miao, J-Y, and Zhao, B-X. 2019. A mitochondria-targeted ratiometric fluorescence sensor for the detection of hypochlorite in living cells. *Dyes and Pigments*; 171: 107708.

# Dosimetric Comparison of The Effects of Different Treatment Plan Techniques on Reduction in Critical Organs in Whole Brain Radiotherapy Application

Hikmettin Demir<sup>1\*</sup> , Gül Kanyılmaz<sup>2</sup> 

<sup>1</sup>Department of Radiation Oncology, Faculty of Medicine, Van Yuzuncu Yıl University, Konya, Türkiye  
<sup>2</sup>Department of Radiation Oncology, Faculty of Medicine, Necmettin Erbakan University, Konya, Türkiye

\*[hikmettindemir@yyu.edu.tr](mailto:hikmettindemir@yyu.edu.tr)

\* Orcid No: 0000-0002-1171-4821

Received: 26 November 2023

Accepted: 17 February 2024

DOI: 10.18466/cbayarfbe.1396284

## Abstract

Different radiotherapy treatment techniques can be used in whole-brain radiotherapy (WBRT). This study aims to investigate the dosimetric advantages of the anterior isocentric (AI) technique which is produced as an alternative to the central isocentric (CI) technique. 25 whole brain patients were included in this retrospective study. Plans were made with two treatment techniques for each patient. One central isocenter (CI) was made using a conventional helmet field (HF) to center the whole brain, which is the isocenter of the target volume. An automatic margin of 5 mm was given to the planning target volume (PTV) with multileaf collimators (MLC) for both plans. For CI and AI techniques, a total dose of 30 Gy was given in 10 fractions with 6 MV photon energy. The two planning techniques were compared dosimetrically. The dose homogeneity index (DHI) had lower values in the AI plan according to CI plans significantly ( $p=0.049$ ). There was a 6,57% difference between CI and AI planning techniques for the maximum dose of the right lens. For the minimum dose and mean dose AI plans significantly had lower values according to the CI plan ( $p=0.001$  and  $p=0.028$  respectively). In this dosimetric study, we found that the AI treatment technique for WBRT was superior to the CI technique for DHI and organs at risk. We recommended to use the AI technique, especially to better protect organs at risk in WBRT.

**Keywords:** Anterior isocenter, brain, radiotherapy, central isocenter

## 1. Introduction

Although developments in the field of radiotherapy used in the treatment of cancer patients are very rapid, conventional approaches are still frequently used in whole-brain (WB) irradiation. Brain metastases, one of the most common intracranial tumors in adults, are 10 times more common than brain tumors and are seen in 24% of autopsies of all cancer patients [1]. Palliative WB radiotherapy is one of the main treatment methods in the treatment of metastatic brain tumors [2]. WBRT is also the main treatment method for patients with intracranial metastases and the average life expectancy of these patients is between 4 and 6 months [3]. Long-term side effects such as dementia, neurocognitive disorders and radionecrosis are important in increasing the survival rates of patients receiving WBRT and these complications are more important for patients with longer life expectancy [2]. Therefore, better targeting and critical organ protection are important for WB patients.

In addition, the International Commission on Radiation Units (ICRU) recommends that the PTV in WB irradiation should be between a minimum of 95% and a maximum of 107% dose distribution [4] and it is not always possible to reach this dose distribution [5,6].

On the other hand diagnostic devices such as Computed Tomography (CT), Magnetic Resonance Imaging (MRI) and positron emission tomography (PET) can be used to delineate critical organs and tumor. For example, if PET/CT is available it can be used for determining the localization of the hidden disease in early detection, distant metastasis and synchronous cancer plays an important role in its definition [7].

Currently, several WB irradiation techniques are used to improve dosimetric dose distributions. These include therapy techniques such as physical compensators, electronic compensators, and intensity-modulated radiotherapy, Helical tomotherapy (HT) [8-17]. These techniques can be selected based on availability

according to the number of devices, number of patients and planning systems [2].

In our study we aimed to make new WB treatment plan across the CI plan which named AI plan. The CI plan standart helmet field which two opposite lateral beam to the icocenter. The plan we offer is AI plan which isocenter point close to anterior of PTV to decrease divergency. In AI plan we expected that make plan dose distribution homogenusly and less dose to the critical structures.

## 2. Materials and Methods

### 2.1. Patients

25 WB patients with an average age of 53 years, who had previously been treated with a standard 3D-conformal plan were selected for the retrospective study. The simulation of these patients was performed using a thermoplastic head mask, in the supine position and with the arms at the side. We used CT (Siemens Somatom Duo, Germany) with a 5 mm section interval, covering the entire brain, up to the end of the cervical vertebra. The data obtained from CT transferred dia with Digital İmaging and Commication in Medicine (DICOM) to Eclipse™ treatment planning system (TPS), (version 8.9.08, Eclipse, Varian Medical Systems, Palo Alto, CA, USA).

### 2.2. Planning target volumes and critical structure

The body contour was drawn automatically by the planning system and the critical organs, the eyes, lenses and optic nerves were drawn by radiation oncologists according to the Radiation Therapy Oncology Group (RTOG) guidelines. When defining the planning target volume a 3 mm margin was given to WB tissue determined as the target tissue but arrangements were made in the organ at risk (OAR) regions formed by lenses, eyes and optic nerves.

### 2.3. Treatment planning

All plans for all the WB patients that we selected were re-made with the Eclipse TPS. First, the plan named central isocenter (CI) was made using a conventional helmet-field (HF) to center of the WB which is the isocenter of target volume. Plans were calculated by giving 5 mm automatic margins to the PTV with multi-leaf collimators (Figure 1a and Figure 1b.). While making the second plan, the isocenter was placed close to the eye level and named the AI plan was calculated by automatically giving 5 mm margin to the PTV in all directions by MLC. Figure of beams eye view (BEV) showed in Figure 2a and Figure 2b. The maximum dose

of the AI plan was normalized to the same value as the CI plan for the sake of same comparison conditions. In both techniques, three-dimensional conformal treatment plans were made using 6 MV photon energy. To ensure the same plan conditions no manual shaping was done in MLC in the two planning techniques.

### 2.4. Dosimetric Evaluation

In the study, the treatment dose was administered as 30 Gy in 10 fractions at the isocenter. A linear accelerator with 82 leaf (Siemens Primus Plus, Germany) treatment device was used for the planning. To help compare the dosimetric parameters of the CI plan and AI plans under the same conditions, the AI plan, which always has a lower maximum dose but less PTV coverage, was normalized to obtain plans with the same maximum dose. Additionally, dose volume histograms (DVH) were created for both plan groups. Dose homogeneity index for PTV were compared for both plans. Dose homogeneity Index (DHI) was calculated for all plans as D5/D95 (minimum dose at five percent of PTV/ minimum dose at ninety-five percent of PTV) [16]. The value of DHI close to 1 means the better homogeneous dose distribution in the plan. Minimum, maximum, and mean doses for lenses, eyes and optic nerves in each plane were compared.

### 2.5. Statistical Analysis

The Statistical Package for Social Sciences (SPSS) v.25.0 was used for statistics (SPSS Inc. Chicago, IL, USA). A paired samples t-test was used for comparison. The minimum, maximum and average doses to the OAR; lens, eye and optic nerves were compared for both plans. It was considered significant because the p value was less than 0.05.

## 3. Results and Discussion

DVH for a patient is shown in Fig.3. On the other side  $p$  values for both plans are listed in Table 1. There was a 6,57% difference between CI and AI planning technique for maximum dose of the right lens. But also there was a significant difference between two techniques for the minimum and mean dose of right lens. AI planning technique had less minimum right lens dose according to CI technique ( $p=0.001$ ) and also AI technique had less mean right lens dose according to CI technique ( $p=0.028$ ). On the other hand we have significant difference for the minimum, maximum and mean dose of the left lens. For these doses AI planning technique had less doses due to CI planning technique. Mean doses for both right and left eyes had differences 0.27% and 0.039 respectively for two techniques.

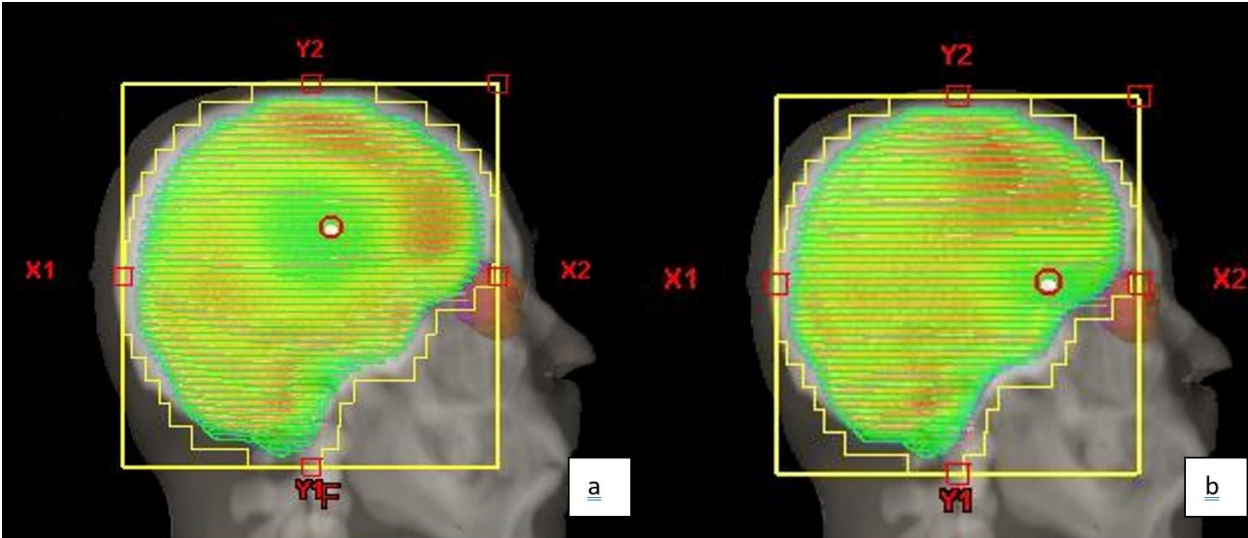


Figure 1. BEV for an example patient (a) CI technique, (b) AI technique.

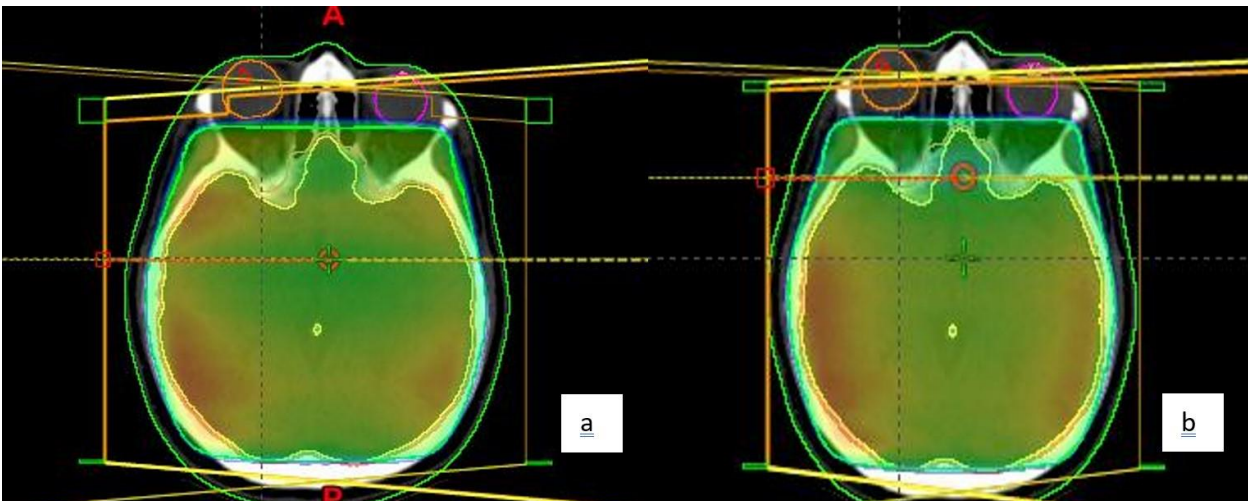


Figure 2. The dose distribution of sagittal view for a patient (a) CI technique (b) AI technique.

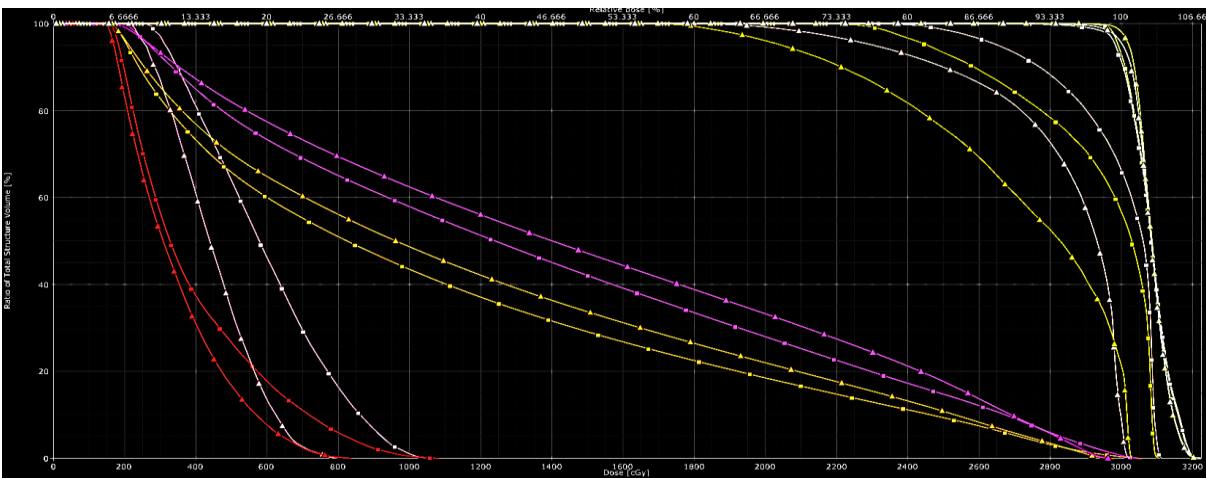


Figure 3. Dose-volume histogram comparison of a patient for two techniques; red: right lens, pink: left lens, yellow: right eye, purple: left eye, open green: right optic nerve, open pink: left optic nerve and white: PTV

**Table 1.** Comparison of dosimetric parameters between CI and AI plans.

Parameters		CI Plan (cGy) (Mean±SD)	AI Plan (cGy) (Mean±SD)	ΔMean±SD (CI-AI)	P
RT Lens	D <sub>max</sub>	809.67±283.54	756.46±319.13	53.21±99.08	0.056
	D <sub>min</sub>	238.33±111.55	221.27±108.63	17.07±16.61	<b>0.001</b>
	D <sub>mean</sub>	448.07±192.19	422.07±198.39	25.99±41.21	<b>0.028</b>
LT Lens	D <sub>max</sub>	780.21±330.63	715.39±329.54	64.82±102.88	<b>0.029</b>
	D <sub>min</sub>	253.69±127.41	225.47±101.30	28.22±46.36	<b>0.033</b>
	D <sub>mean</sub>	456.93±188.39	409.99±172.55	46.95±71.32	<b>0.023</b>
RT Eye	D <sub>max</sub>	3087.15±109.42	3031.58±94.99	55.57±39.22	<b>&lt;0.001</b>
	D <sub>min</sub>	139.23±45.57	130.83±42.50	8.40±5.78	<b>&lt;0.001</b>
	D <sub>mean</sub>	1338.19±388.19	1334.48±392.22	3.70±46.25	0.761
LT Eye	D <sub>max</sub>	3076.77±59.32	3034.90±59.12	41.87±39.83	<b>0.001</b>
	D <sub>min</sub>	144.09±54.13	133.39±60.73	10.69±14.91	<b>0.015</b>
	D <sub>mean</sub>	1420.45±349.58	1419.90±358.92	0.55±59.83	0.972
RT Optic Nerve	D <sub>max</sub>	3110.98±40.30	3032.21±39.35	78.76±21.84	<b>&lt;0.001</b>
	D <sub>min</sub>	2022.56±774.08	1972.73±764.26	49.83±160.29	0.249
	D <sub>mean</sub>	2843.35±263.97	2775.16±253.31	68.19±58.48	<b>&lt;0.001</b>
LT Optic Nerve	D <sub>max</sub>	3091.62±38.88	3028.83±34.85	62.79±23.61	<b>&lt;0.001</b>
	D <sub>min</sub>	2289.71±492.94	2253.08±476.74	36.63±184.68	<b>0.455</b>
	D <sub>mean</sub>	2899.07±158.23	2842.06±136.48	57.01±50.79	<b>0.001</b>
HI		1.0724±0.0107	1.0701±0.0092	0.0022±0.004	<b>0.049</b>
MU		317.67±4.53	316.00±6.11	1.67±3.98	0.127

CI: Central isocentric, AI: anterior isocentric

The minimum and maximum doses for two techniques were significant and AI technique had lower doses than CI technique. For the optic nerves, maximum and mean doses significantly had lower dose in the AI plan technique than CI technique. The homogeneity index of the AI plan significantly had a lower value due to CI plan (p=0,049).

In this study, when the CI and AI plans were compared, which were brought to the same maximum dose plan value, the beam deviation that would occur by moving the treatment isocenter, the source of the plan difference, upwards from the target volume center was reduced in order to ensure that the lens and eye doses were lower with lower dose limits and the target volume received a better dose. In addition, the planner can make some changes to the MLCs and change a small isocenter, then a better plan can be obtained, but to try to provide equivalent conditions, the isocenter puts randomly and also the MLC coverage is done automatically. The average life expectancy of metastatic WB patients is around one year [17]. Studies show that in the long term, WB irradiation causes symptoms such as memory loss, motor control impairment and urinary incontinence [18-21]. In these cases, the better dose coverage of plans and less critical organ doses have an important role for the remaining quality of life. The dose distribution and critical organ doses changes with anatomy of patients. But statistically we saw that standard AI gave less critical organ doses and had better dose homogeneity in PTV.

Fujita and his colleagues compare two WBRT techniques to compare dosimetric parameters of plans [3]. They

chose twenty patients that had already been treated to made retrospective planning using irregular surface compensator (ISC) and compare it with conventional radiotherapy techniques. They found ISC technique had lower DHI and mean and maximum lenses and eyes doses (p<0.05) were also reduced. In this study AI plan had lower values of maximum, minimum and mean doses according to CI plan technique. It was also observed that the AI technique had more dose homogeneity.

Yavas and his colleagues aimed in their study that compared two standard HT plan and classical technique with collimator changed plans (CT) according to OAR such as lenses, eye-balls and optic nerves [22]. And also differences in DHI and monitor units (MU). They found that there were no differences for DHI (p:0.182) and MU (p:0.167) with two techniques. But for maximum and mean doses of the right lens, left lens and right eye-ball were significantly lower in CT technique (p values for maximum doses 0.007, 0.012 and 0.010 respectively; for mean doses 0.027, 0.046 and 0.002 respectively). However, significant differences in DHI were found in this study. Better DHI results were achieved with the AI planning technique than with the CI planning technique. Doses to critical organs (both lenses and eyes) in the AI technique were lower than in the CI technique. Another study on metastatic WBRT was conducted by Andic and colleagues. Compared dosimetric data of 30 patients for conventional two-dimensional (2D) helmet-field with three-dimensional conformal radiotherapy (3D-CRT) techniques to compare dose coverage to the brain and Retro-orbital area (RO) [23]. On the other side they looked for the ocular lens protection. They found the minimum doses mean for RO areas statistically higher in 3D-CRT plans than 2D plans

( $p=0.008$ ). On the other hand the mean values of maximum doses in clinic target volume (CTV), RO areas and lenses had no differences for two plan techniques. They concluded that 3D-CRT planning improved dose coverage of RO areas and the dose homogeneity in WB and protected ocular lenses when compared with 2D conventional radiotherapy planning technique. In this study, DHI was lower on the AI plan than on the CI plan, and lower doses were used for all critical organs.

James B. Yu and his colleague compared conventional helmet-field planning technique with two field intensity modulated radiation therapy (IMRT) techniques for 10 patients in WBRT [1]. They found that IMRT improved dose uniformity across External Beam Radiation Therapy (EBRT) for WBRT. The conventional technique increases the dose into superior frontal region of the brain. These hot points didn't occur in IMRT technique. But they also reported that IMRT technique increased the number of MU to deliver necessary doses. The more dose homogeneity and this increases the more total body dose including scattering and leakage. This may increase second malignancies probability [24]. There were also studies conducted by Hall et al., which stated that the likelihood of second malignancy was significantly increased in children who received long curative treatment and survived [25]. The AI technique used in this study had better treatment results in terms of homogeneous dose distribution but was not as good as the IMRT technique. On the other hand, less MU and less treatment time were obtained compared to the two-field IMRT technique. It can be stated that sometimes the treatment period of a WBRT patient may be very limited.

#### 4. Conclusion

AI treatment technique had more advantages according to CI technique for WBRT treatment with respect to lower DHI and critical organ doses such as lenses, eyes and optical nerves. That is what we expect from this study. Thus in WBRT treatments changing isocenter close to the optical zone had less organ doses and more homogeneity. If a clinic is going to perform 3D-CRT for WBRT, we recommend that they consider the AI technique.

#### Author's Contributions

**Hikmettin Demir:**

**Gül Kanyılmaz:**

#### Ethics

There are no ethical issues after the publication of this manuscript.

#### Acknowledgement

There are no financial declarations. This work is not grant funded.

#### References

- [1]. Yu, J., S. Shiao, and J. Knisely, 2003: A *Dosimetric Evaluation of Conventional Helmet Field Irradiation Versus Two Field Intensity Modulated Radiation Therapy Technique*. International Journal of Radiation Oncology, Biology, Physics, 2006. 66(3): p. S255-S256.
- [2]. Yu, J., S. Shiao, and J. Knisely, 2003: A *Dosimetric Evaluation of Conventional Helmet Field Irradiation Versus Two Field Intensity Modulated Radiation Therapy Technique*. International Journal of Radiation Oncology, Biology, Physics, 2006. 66(3): p. S255-S256.
- [3]. Fujita, H., et al., *Improvement of dose homogeneity with irregular surface compensator in whole brain radiotherapy*. Journal of Radiotherapy in Practice, 2016. 15(3): p. 269-275.
- [4]. Murray, K.J., et al., *A randomized phase III study of accelerated hyperfractionation versus standard in patients with unresected brain metastases: a report of the Radiation Therapy Oncology Group (RTOG) 9104*. International journal of radiation oncology, biology, physics, 1997. 39(3): p. 571-574.
- [5]. Gul OV. *Experimental evaluation of out-of-field dose for different high-energy electron beams and applicators used in external beam radiotherapy*. Radiation Physics and Chemistry. 2024;215.
- [6]. Gul OV, Duzova M. *Effect of different CTV shrinkage and skin flash margins on skin dose for left chest wall IMRT: A dosimetric study*. Radiation Physics and Chemistry. 2024;216.
- [7]. Jones, D., *ICRU report 50—prescribing, recording and reporting photon beam therapy*. 1994, Wiley Online Library.
- [8]. Kanyılmaz, G., Baş-boyun kanserlerinde radyoterapi planlamasında 18f-fdg pet/bt kullanımı. Mevlana Tıp Bilimleri Dergisi, 2021. 1(3): p. 85-88.
- [9]. Lerch, I.A. and J. Newall, *Adjustable compensators for whole-brain irradiation*. Radiology, 1979. 130(2): p. 529-532.
- [10]. Keall, P., et al., *The development and investigation of a prototype three-dimensional compensator for whole brain radiation therapy*. Physics in Medicine & Biology, 2008. 53(9): p. 2267.
- [11]. Goyal, S., et al., *Improvement in dose homogeneity with electronic tissue compensation over IMRT and conventional RT in whole brain radiotherapy*. Radiotherapy and Oncology, 2008. 88(2): p. 196-201.
- [12]. Gondi, V., et al., *Hippocampal-sparing whole-brain radiotherapy: a "how-to" technique using helical tomotherapy and linear accelerator-based intensity-modulated radiotherapy*. International Journal of Radiation Oncology\* Biology\* Physics, 2010. 78(4): p. 1244-1252.
- [13]. Marsh, J., et al., *Sparing of the hippocampus and limbic circuit during whole brain radiation therapy: a dosimetric study using helical tomotherapy*. Journal of Medical Imaging and Radiation Oncology, 2010. 54(4): p. 375-382.
- [14]. van Kesteren, Z., et al., *A practical technique to avoid the hippocampus in prophylactic cranial irradiation for lung cancer*. Radiotherapy and Oncology, 2012. 102(2): p. 225-227.
- [15]. Rong, Y., et al., *Dosimetric evaluation of intensity-modulated radiotherapy, volumetric modulated arc therapy, and helical tomotherapy for hippocampal-avoidance whole brain radiotherapy*. PloS one, 2015. 10(4): p. e0126222.

- [16]. Kao, J., et al., *Tumor directed, scalp sparing intensity modulated whole brain radiotherapy for brain metastases*. *Technology in cancer research & treatment*, 2015. 14(5): p. 547-555.
- [17]. Gong, Y., et al., *Conventionally-fractionated image-guided intensity modulated radiotherapy (IG-IMRT): a safe and effective treatment for cancer spinal metastasis*. *Radiat Oncol*, 2008. 3: p. 11.
- [18]. Narita, Y. and S. Shibui, *Strategy of surgery and radiation therapy for brain metastases*. *International Journal of Clinical Oncology*, 2009. 14(4): p. 275-280.
- [19]. DeAngelis, L.M., J.-Y. Delattre, and J.B. Posner, *Radiation-induced dementia in patients cured of brain metastases*. *Neurology*, 1989. 39(6): p. 789-789.
- [20]. Twijnstra, A., et al., *Neurotoxicity of prophylactic cranial irradiation in patients with small cell carcinoma of the lung*. *European Journal of Cancer and Clinical Oncology*, 1987. 23(7): p. 983-986.
- [21]. Laukkanen, E., et al., *The role of prophylactic brain irradiation in limited stage small cell lung cancer: clinical, neuropsychologic, and CT sequelae*. *International Journal of Radiation Oncology\* Biology\* Physics*, 1988. 14(6): p. 1109-1117.
- [22]. Yavaş, G., et al., *Dosimetric comparison of two different whole brain radiotherapy techniques in patients with brain metastases: How to decrease lens dose?* *International Journal of Radiation Research*, 2014.
- [23]. Andic, F., et al., *Dosimetric comparison of conventional helmet-field whole-brain irradiation with three-dimensional conformal radiotherapy: dose homogeneity and retro-orbital area coverage*. *The British Journal of Radiology*, 2009. 82(974): p. 118-122.
- [24]. Hall, E.J. and C.-S. Wu, *Radiation-induced second cancers: the impact of 3D-CRT and IMRT*. *International Journal of Radiation Oncology\* Biology\* Physics*, 2003. 56(1): p. 83-88.
- [25]. Hall, E.J., *Intensity-modulated radiation therapy, protons, and the risk of second cancers*. *International Journal of Radiation Oncology\* Biology\* Physics*, 2006. 65(1): p. 1-7.

# Optically Anisotropic Films of Colloidal Nanocrystals/Photoluminescent Dye Doped Polymers

Zeynep Dikmen\* 

Eskisehir Osmangazi University, Faculty of Engineering, Department of Biomedical Engineering, Eskisehir 26040, Türkiye

\*[zeynilmaz@ogu.edu.tr](mailto:zeynilmaz@ogu.edu.tr)

\* Orcid No: 0000-0002-1365-6573

Received: 22 November 2023

Accepted: 9 March 2024

DOI: 10.18466/cbayarfbe.1394435

## Abstract

Semiconductor colloidal nanocrystals are attractive materials since they can be adapted to polymers to form hybrid materials and are compatible with many optical applications. Here, synthesis of CdSe/CdS nanorods (NRs) via hot injection method is carried out, followed by preparation of hybrid polymer films from polyethylene glycol monomethyl ether-*block*-poly(glycidyl methacrylate)-*block*-poly[2-(diethylamino)ethyl methacrylate] triblock copolymer (MPEG-*b*-PGMA-*b*-DEAEMA) at a liquid-air interface. The optical properties of the films are finely adjusted to form optically anisotropic (i.e. dual-color emissive) films by using dyes for the other emitter as desired. Thiazolo[5,4-*d*] thiazole (TTz)-based dye and 6-carboxy fluorescein were used for this purpose. Tunable emission of TTz dye from blue to green dependent on changing pH value resulted in blue-green emissive polymer films, while red emission of CdSe/CdS NRs caused red emissive films. Phase separation of these materials is achieved by the hexane-insoluble nature of MPEG-*b*-PGMA-*b*-DEAEMA and the high solubility of NRs in it. These dual emissive films are promising candidates for waveguides and optical sensors.

**Keywords:** Optically anisotropic film, CdSe/CdS nanorods, dual emissive films, confocal microscopy

## 1. Introduction

Colloidal nanocrystals can be described as a hybrid material consisting of an inorganic core coated with a layer of organic molecules (ligands). Semiconductor nanocrystals are unique materials with extended optical properties such as high quantum yield, narrow full-width half maximum, and tunable emission wavelength. Such materials are great as dopants for various matrixes to get functional materials. Polymers are quite advantageous as matrix materials for nanocrystals due to their low cost, simple processability, and availability on an industrial scale. Dielectric polymers such as polydimethylsiloxane, polystyrene, and polyacrylates can be used as a matrix for semiconductor nanocrystals due to their optical transparency in the visible region, mechanical strength, flexibility, and their well-known chemical behavior. There are various strategies for incorporating colloidal nanocrystals into polymer matrixes without substantially altering their initial photophysical properties. One of the most widely used and simplest ways is to mix hydrophobic nanocrystals directly as-synthesized with a polymer solution in nonpolar solvents and then evaporate

the solvent to form the mixture to form a solid matrix. Another approach is to disperse nanoparticles in monomers or pre-polymerized oligomers and perform in-situ polymerization to obtain nanocomposites with embedded nanocrystals<sup>1</sup>. The most used polymer matrix materials, such as polyacrylates and polystyrene derivatives, limit the potential applications of nanocrystals because of their solid matrixes. Polymethylmethacrylate (PMMA) is used as a matrix for CdSe colloidal quantum wells,<sup>2</sup> a homogenous CuZnInS (CZIS) nanocrystal-embedded polystyrene with high quantum yield is reported in the earlier studies<sup>1,3</sup>. In addition to these solid matrixes, CdSe/CdS nanorods were embedded into the flexible polymer to form a film to orient the nanorods by stretching the film, resulting in a higher emission intensity<sup>4</sup>. CdS quantum dot doped polymers were investigated effectively for further applications<sup>5</sup>. Polymer / nanocrystal-based hybrid structures with unique optical properties were also obtained by encapsulating nanocrystals with amphiphilic polymers<sup>6,7</sup>. Photoluminescent polymers have been prepared by various approaches in the early reports. In the 1980s, Dy<sup>3+</sup>, Er<sup>3+</sup>, Eu<sup>3+</sup>, Tb<sup>3+</sup>, and Sm<sup>3+</sup> doped

copolymers were prepared to prepare fluorescence polymer materials, and their optical properties, which vary with the thickness and dopant amount of the films were examined<sup>8-10</sup>. Combining copolymers with fluorescent structures such as N-vinyl carbazole-containing vinyl groups has been another strategy to prepare fluorescent polymers in these years<sup>11,12</sup>. In other reports, fluorescence polymers were prepared by adding dyes to polymers to investigate the effect of the polymer matrix on the Stokes shifts of the fluorophore<sup>13,14</sup>. By enabling the radical formation of polymers with an initiator such as 9-fluorenyl lithium or by reacting a polymer with a polymeric active end group such as poly(styryl)lithium with a fluorescence monomer such as 1-phenyl-1-(1-pyrenyl)ethylene, the fluorescence molecule is attached to the polymers as an end group<sup>15,16</sup>. Organic small photoluminescent dyes are well-known materials to prepare highly emissive polymer materials<sup>17</sup>. Thiazolo[5,4-*d*]thiazole (TTz)-based fluorophores are one of the most attractive fluorophores since they have exhibited solvatochromic effect<sup>18</sup>, excited-state intramolecular proton transfer (ESIPT)<sup>19</sup>, and optical properties varying in tautomer form. TTz-based fluorophores consisting of two adjacent thiazole rings, have been among the topics of interest in organic electronics due to their planar and rigid structure and superior optical-electronic properties. Interest in TTz compounds has increased dramatically in the last decade, after the reporting of effective studies on their use in optoelectronic devices such as organic light-emitting diodes (OLEDs)<sup>20</sup> and organic field effect transistors (OFETs)<sup>21,22</sup>. After these initial reports, an increasing number of small molecule compounds and polymeric materials containing the thiazolo[5,4-*d*]thiazole unit have been described in the literature. Their applications in various fields, including photovoltaics, have been investigated<sup>23-29</sup>. Photoluminescent polymeric films with solvatochromic memory<sup>30</sup>, having phosphorescence at room temperature<sup>31</sup>, radiation-sensitive polymer films as dosimeters<sup>32</sup>, the use of in-situ SiO<sub>2</sub> synthesized biodegradable films in food packaging<sup>33</sup>, fluorescence films for enzyme-free H<sub>2</sub>O<sub>2</sub> detection<sup>34</sup>, temperature sensitive polymer films<sup>35,36</sup>, polymer films for TNT detection<sup>37</sup>, erasable fluorescence imaging<sup>38</sup> are some intriguing reports showing different applications of such films.

Herein, a new approach is reported to prepare optically anisotropic films having dual color emission in the two sides of the films consisting of nanocrystals and photoluminescent organic dyes. CdSe/CdS NRs were used as orange-red emitter while the 2,5-bis(4-hydroxyphenyl)thiazolo[5,4-*d*]thiazole (HPhTT) molecule was used as blue / green emitter. The synthesized NRs and optically anisotropic films were characterized with TEM imaging, ATR-IR, Raman spectroscopy, spectrophotometric / spectrofluorometric analysis and confocal microscopy. These films are

unique materials for various optical applications such as waveguides or sensors.

## 2. Materials and Method

### 2.1. Materials

All chemical solvents and reagents were supplied commercially and used without any further purification. ethanol (96%), 2-(diethylamino)ethyl methacrylate (DEAEMA, 98%), 4-hydroxy benzaldehyde (98%), polyethylene glycol monomethyl ether, glycidyl methacrylate (GMA, 97%), CuCl (99%), and KOH (%85) were purchased from Sigma-Aldrich. CdO (Sigma-Aldrich, 99.9%), trioctyl phosphine (TOP, abcr, 97%), ODPa (abcr, 97%), Se (Sigma-Aldrich, 99.99%), trioctyl phosphine oxide (TOPO, Alfa Aesar, 98%), S (Sigma-Aldrich, 90%), ethanol (Sigma-Aldrich, 99.8%), methanol (Alfa Aesar, 99.9%), THF (Sigma-Aldrich, 99.9%), hexane (Honeywell), toluene (Merck, anhydrous), ethylene glycol (EG, Sigma-Aldrich, 99%) diethylene glycol (DEG, Sigma-Aldrich, 99%) were used. Toluene (99.8%) was from Interlab. Dithiooxamide (98%),  $\alpha$ -bromoisobutyryl bromide (BIBB, 98%) were purchased from Acros Organics. Pyridine (99%), triethylamine (99%), tetrahydrofuran (THF, 99%) and hexane (95%) were purchased from Merck. 2,2'-Bipyridine (BPy, 99%) was from Alfa Aesar. Acetic acid (AcOH, 100 %) and KH<sub>2</sub>PO<sub>4</sub> (99%) was supplied from Reidel-de Haen. Poly(ethylene glycol) methyl ether (MPEG, 2000 g/mol) was supplied from Fluka.

### 2.2. Method

#### 2.2.1. Preparation of Se precursor

0.058 g of Se powder and 1.2 g of TOP is put in a 2 ml vial and mixed for 1 hour at 80 °C till all Se powder is dissolved. A colorless homogeneous solution formation indicates the dissolution of Se in TOP.

#### 2.2.2. Synthesis of CdSe seed

Hot injection method was performed by injecting a cold chalcogenide precursor into a high-temperature metal precursor for CdSe quantum dots synthesis. 3.00 g of TOPO, 0.06 g CdO and 0.28 g ODPa are put in a three necked flask inside the glove box for further attachment to the Schenk line in the fumehood. The mixture was melted in N<sub>2</sub>(g) atmosphere, then the mixture was stirred for 1 hour under vacuum (4.10<sup>-2</sup> Torr) at 170 °C to remove the oxygene and water in the environment and the chemicals that will inhibit the reaction. Later, the reactants are allowed to interact at 300 °C to form a colorless solution. The temperature is increased to 380 °C for injecting 1.5 g TOP and then Se-TOP precursor. The heating mantle is quickly removed when the color of the solution turns brownish red. The flask is rapidly cooled, and 5 mL of anhydrous toluene is injected. Then, the

quantum dot colloidal solution is precipitated by adding 2 mL of anhydrous methanol twice by centrifugating at 3000 rpm for 10 minutes.

### 2.2.3. Preparation of S precursor

0.12 g of S powder and 1.5 g of TOP was placed in a 2 ml vial, and stirred at 80 °C for 1 hour to dissolve all S in the TOP. A colorless solution was obtained.

### 2.2.4. Synthesis of CdSe/CdS NRs

CdSe/CdS NRs were synthesized via seeded growth approach. 0.06 g CdO, 3 g TOPO, 0.34 g OHPA were weighted to put in a three-necked flask. The reactants were kept under vacuum for approximately 1 hour at 170 °C. The mixture was heated to 355 °C. 1.5 g of TOP was injected when it reached the injection temperature, followed by injection of S-TOP and CdSe quantum dot precursors. Crystals were allowed to grow for 6 minutes at this temperature. Rapid cooling of the reaction flask was achieved by water bath. 10 mL of toluene was injected when the temperature dropped to 60 °C. The product was transferred to vials using a syringe. Purification was achieved by centrifugation at 3000 rpm by adding methanol solution<sup>39</sup>.

### 2.2.5. Preparation of optically anisotropic films

Optically anisotropic films were prepared at liquid air interface. Ethylene glycol (EG) containing 0.05 g HPhTT dye and 0.005g hexamethylene diamine was used as subphase to form interface. A mixture of NRs and polymer was prepared by dissolving 0.6 g of synthesized MPEG-*b*-PGMA-*b*-DEAEMA block copolymer that is described in our earlier report<sup>29</sup> and 200  $\mu$ L NRs in 5 mL hydrophobic solvent (i.e. toluene). The mixture was put on top of EG and the solvent was evaporated slowly to form a solid film. The film was removed from the top of the solution and washed with isopropanol to remove unreacted dyes and EG, then they are dried at room temperature.

## 3. Results and Discussions

Here hot injection method modified by seeded growth approach was used for the synthesis of CdSe/CdS core/shell nanorod by using CdSe QD as seed. Strong and tunable light emission from green to red can be obtained from these CdSe/CdS nanorods having narrow size distributions by this method<sup>39, 40</sup>. CdSe/CdS NRs with red emission were synthesized by using well-defined CdSe QDs as seed. TEM images of the CdSe QDs and NRs are given in Figure 1-a,b, respectively.

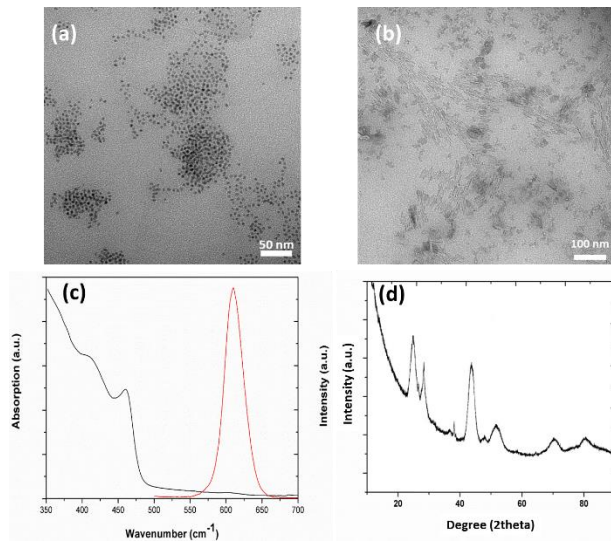


**Figure 1.** TEM image of CdSe seed (a), CdSe/CdS NRs (b), absorption and PL spectra (c), XRD spectrum (d) of CdSe/CdS NRs (Reference code: 98-065-9045)

The absorption from CdS shell as the high-energy peaks and the lowest energy peak originated from electronic transitions from holes confined in the CdSe seed is given in the absorption spectrum (Figure 2c). Photoluminescence (PL) peak of the NRs is located at 610 nm as shown in Figure 2c [37, 38].

The absorption from CdS shell as the high-energy peaks and the lowest energy peak originated from electronic transitions from holes confined in the CdSe seed is given in the absorption spectrum (Figure 2c). Photoluminescence (PL) peak of the NRs is located at 610 nm as shown in Figure 2c<sup>39, 41</sup>.

The synthesized NRs were also characterized by X-ray diffraction analysis (Figure 1-d). Cadmium chalcogenide peaks are observed at  $2\theta = 24.86^\circ, 26.45^\circ, 28.21^\circ, 36.61^\circ, 43.78^\circ, \text{ and } 51.88^\circ, 71.03^\circ, 83.354^\circ$  which can be assigned to the, (010), (002), (011), (012), (110), (112), (121), (123) reflections, respectively<sup>42</sup>.

The synthesized NRs were used to prepare composite films in the liquid-air interface. In the literature, preparation of colloidal nanocrystal doped polymer films is performed via casting method onto a Petri dish without any phase separation. However, the polymers are consist of commercially available, single chain polymers<sup>6, 43, 44</sup>. Even there are some reported composite examples of colloidal semiconductor nanocrystals/block copolymers, the films of the composites were prepared via casting method<sup>45</sup>. Here amphiphilic behavior of the block copolymers is used to manage phase separation to get dual-wavelength emission. Dual wavelength emissive materials of colloidal nanocrystals can be prepared by using silica nanoparticles with a sequential deposition method as reported before<sup>46</sup>. Such dual wavelength emissive materials have great attention due to their high

demand in many application fields, such as photonic circuits<sup>47</sup> biosensors<sup>48</sup>, on-chip optical communication<sup>49</sup> and bioimaging<sup>50</sup>. In this new method one-step preparation of dual emissive films is achieved by managing solution behavior of block copolymers and nanorods. The nanorods and polymer solution in hydrophobic solvents such as hexane and toluene was used for further slowly evaporation of the solvent to form a solid film on the top of liquid subphase.

HPhTT dye addition to subphase resulted in diffusion of the dye in the polymer films. The diffusion rate is expected to be higher in the contact layer of polymer with the subphase (i.e. liquid interface). The diffusion of the dye decreases at the air interface.

This diffusion gradient results in a phase separated green emission of HPhTT. On the other hand, the highly hydrophobic ligands around the NRs and the amphiphilic behaviour of the polymer limits the interaction of NRs with the subphase.

So, amphiphilic polymer molecules assemble on top of subphase (i.e. liquid interface) similar to surfactant behaviour resulting in the phase separation of NRs from green emission. Digital images of the experimental set up of optically anisotropic film preparation under daylight and UV-light excitation are given in Figure 2 (top) with dual color emission.

The solid films obtained by this method are given in Figure 2 (bottom). The dual color emission from both layers of the films can be seen under UV-light excitation. It is clearly seen that this method results in an anisotropy when the z-axis (i.e. thickness) of the film is observed. HPhTT dye and NRs distribution in the thickness of the film cause an emission or optical anisotropy.

So the films with dual color emission are named as “optically anisotropic films”.

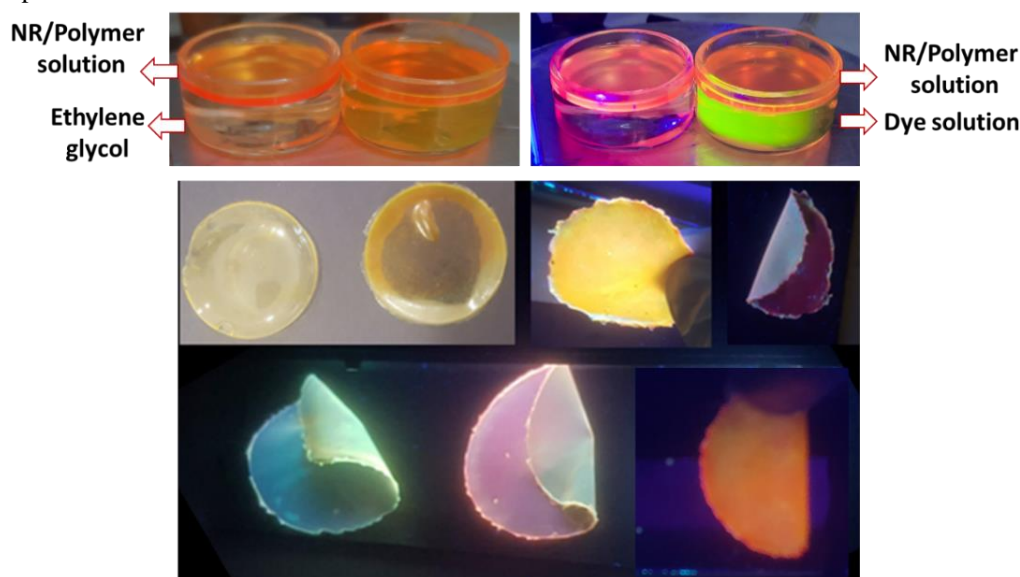


**Figure 2.** Digital images of optically anisotropic film preparation (top), and the final product films under UV-light excitation (bottom).

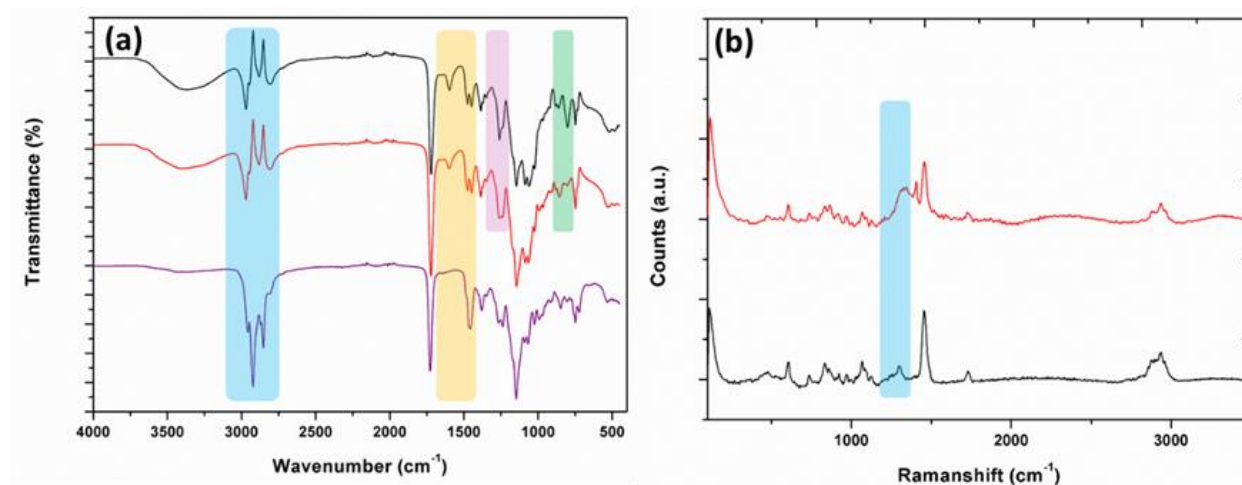


**Figure 1.** ATR-IR spectra of polymer film (black line), dye loaded film (red line) and dye/NR loaded film (purple line) (a), Raman shift of dye loaded film (black line) and dye/NR loaded film (red line) (b).

The films were investigated by ATR-IR and Raman spectroscopies as given in Figure 3a and b, respectively. Since diffused HPhTT dye amount is too less, the vibrations of the molecule was not observed in ATR-IR spectrum while it is interacted with polymer as observed in the fingerprint region (green and lilac signs). ATR-IR spectrum of the NRs containing optically anisotropic films is given in Figure 3a (purple line). The hydrophobic long chain ligands around the NRs can be observed with the stretching of C-H groups at 2900-3000  $\text{cm}^{-1}$ .  $\text{-C=O}$  stretching is at 1729  $\text{cm}^{-1}$ , C-O-C and O-CH<sub>2</sub> stretching is at 1100-1200  $\text{cm}^{-1}$ . The two bands at 1387  $\text{cm}^{-1}$  and 75  $\text{cm}^{-1}$  can be attributed to the  $\alpha$ -methyl group vibrations.

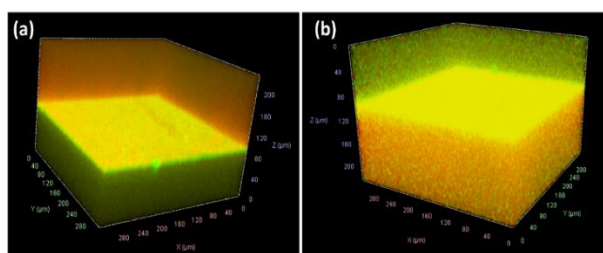


**Figure 3.** Three dimensional confocal micrographs of optically anisotropic film obtained by z-axis scanning

The confocal micrographs of the dual emissive film obtained by z-scanning of the films from both side (i.e. dye rich or nanorod rich regions) is given in Figure 4a-b. The NR rich region is observed by red area while dye rich region is observed as green region. The yellow color is seen because of overlapping of both colors. It is obviously seen successfully achievement of phase separation of the colors can be obtained by this approach.

#### 4. Conclusion

In conclude, a new method to prepare optically anisotropic films is reported. In this study, it has been shown that new materials can be prepared by subphase modification at the liquid-air interface for various nanostructures. For this purpose, colloidal nanocrystals are synthesized and characterized by spectrophotometric, spectrofluorometric analysis, TEM imaging and X-Ray analysis. The prepared films are also characterized by ATR-IR and Raman spectroscopies.

The bending vibration of the C-H bonds of the  $\text{-CH}_3$  group is at 1459  $\text{cm}^{-1}$ . Raman shifts of the dye (black line) and dye/NR (red line) loaded films are given in Figure 3b. The peaks between 440 - 465  $\text{cm}^{-1}$  are due to the bending vibration of the carbonyl group ( $\text{-C=O}$ ). The epoxide asymmetric ring deformation of PGMA is located at 923  $\text{cm}^{-1}$  as a weak band may be attributed to C-H groups of the polymer and ligands around NRs are observed at 2900-3000  $\text{cm}^{-1}$  <sup>51</sup>.

The confocal micrographs are given in Figure 4a,b. The two sides of optically anisotropic film is scanned and dye

rich region is shown as green while NR rich region is shown as red.

It is clearly seen that the film is divided to two region because of the forming dye rich and NR rich areas as a result of diffusion rate of dye, hydrophobic nature of NRs and amphiphilic behavior of the polymer. This new method and novel optically anisotropic films pave the way for many optical applications.

Confocal microscopy is also shown to be used effectively for three dimensional imaging of hybrid materials. This method can be adopted for many other materials and such optically anisotropic films are great candidate for optical sensors and waveguides.

#### The Declaration of Conflict of Interest/ Common Interest

No conflict of interest or common interest has been declared by the author.

#### Author's Contributions

**Zeynep Dikmen:** Visualization, Methodology, Conceptualization, Writing – Review & Editing, Validation, Writing – Original Draft, Data Curation Funding Acquisition, Resources.

#### Ethics

There are no ethical issues after the publication of this manuscript.

#### Acknowledgement

This study was supported by the Scientific Research Projects Coordination Unit of Eskisehir Osmangazi University (ESOGU BAP) within the scope of the project numbered FCD-2023-2764.

#### References

- [1]. A. Prudnikau, D. I. Shiman, E. Ksendzov, J. Harwell, E. A. Bolotina, P. A. Nikishau, S. V. Kostjuk, I. D. W. Samuel and V. Lesnyak. 2021. Design of cross-linked polyisobutylene matrix for efficient encapsulation of quantum dots. *Nanoscale Adv*; 3: 1443-1454.
- [2]. B. M. Saidzhonov, V. B. Zaytsev and R. B. Vasiliev. 2021. Effect of PMMA polymer matrix on optical properties of CdSe nanoplatelets. *J Lumin*; 237: 118175.
- [3]. R. Lesyuk, B. Cai, U. Reuter, N. Gaponik, D. Popovych and V. Lesnyak. 2017. Quantum-Dot-in-Polymer Composites via Advanced Surface Engineering. *Small Methods*; 1: 1700189.
- [4]. P. D. Cunningham, J. B. Souza, I. Fedin, C. She, B. Lee and D. V. Talapin. 2016. Assessment of Anisotropic Semiconductor Nanorod and Nanoplatelet Heterostructures with Polarized Emission for Liquid Crystal Display Technology. *Acs Nano*; 10: 5769-5781.
- [5]. İ. Ç. Keskin, M. Türemiş, M. İ. Katı, R. Kibar and A. Çetin. 2019. Effects of CdS quantum dot in polymer nanocomposites: In terms

- of luminescence, optic, and thermal results. *Radiation Physics and Chemistry*; 156: 137-143.
- [6]. S. Cho, J. Kwag, S. Jeong, Y. Baek and S. Kim. 2013. Highly Fluorescent and Stable Quantum Dot-Polymer-Layered Double Hydroxide Composites. *Chem Mater*; 25: 1071-1077.
- [7]. İ. Ç. Keskin, M. Türemiş, M. İ. Katı, R. Kibar, K. Şirin, M. A. Çipiloğlu, M. Kuş, S. Büyükcşelebi and A. Çetin. 2017. The radioluminescence and optical behaviour of nanocomposites with CdSeS quantum dot. *Journal of Luminescence*; 185: 48-54.
- [8]. E. Banks, Y. Okamoto and Y. Ueba. 1980. Synthesis and Characterization of Rare-Earth Metal-Containing Polymers .1. Fluorescent Properties of Ionomers Containing Dy<sup>3+</sup>, Er<sup>3+</sup>, Eu<sup>3+</sup>, and Sm<sup>3+</sup>. *J Appl Polym Sci*; 25: 359-368.
- [9]. H. Lu, G. F. Li, S. B. Fang and Y. Y. Jiang. 1990. Fluorescent Properties of Polymer Rare-Earth Ion Complexes .2. Poly(Acrylic Acid-Co-Acrylamide) Rare-Earth Ion Complexes. *J Appl Polym Sci*; 39: 1389-1398.
- [10]. K. J. Smit and K. P. Ghiggino. 1991. Effect of Polymer Binding on the Spectroscopic Properties of Stilbene-Based Fluorescent Dyes. *J Polym Sci Pol Phys*; 29: 1397-1405.
- [11]. E. Chiellini, R. Solaro, G. Galli and A. Ledwith. 1980. Optically-Active Vinyl-Polymers Containing Fluorescent Groups .8. Synthesis and Properties of Co-Polymers of N-Vinylcarbazole and (-)-Menthyl Acrylate and (-)-Menthyl Methacrylate. *Macromolecules*; 13: 1654-1660.
- [12]. M. Delfini, M. E. Dicocco, M. Paci, R. Solaro and E. Chiellini. 1985. Optically-Active Vinyl-Polymers Containing Fluorescent Groups .9. C-13-Nmr Spectra of Copolymers of (-)-Menthyl Vinyl Ether with N-Vinylcarbazole. *Eur Polym J*; 21: 723-726.
- [13]. R. E. Sah. 1981. Stokes Shift of Fluorescent Dyes in the Doped Polymer Matrix. *J Lumin*; 24-5: 869-872.
- [14]. C. D. Eisenbach. 1983. Characteristic Features of the Matrix Effect on the Stokes Shift of Fluorescent Dye Molecules in Pure and Plasticized Polymers. *J Appl Polym Sci*; 28: 1819-1827.
- [15]. E. T. B. Altakrity, A. D. Jenkins and D. R. M. Walton. 1990. The Synthesis of Polymers Bearing Terminal Fluorescent and Fluorescence-Quenching Groups .2. The Incorporation of Fluorescent and Fluorescence-Quenching Groups by Means of a Direct Termination Process. *Makromol Chem*; 191: 3069-3072.
- [16]. R. P. Quirk, J. G. Kim, K. Rodrigues and W. L. Mattice. 1990. Anionic Synthesis and Characterization of Poly(Styrene-Block-Ethylene Oxide) Polymers with Fluorescent-Probes at the Block Junctions. *Abstr Pap Am Chem S*; 199: 403-Poly.
- [17]. R. P. Quirk, J. Kim, K. Rodrigues and W. L. Mattice. 1991. Anionic Synthesis and Characterization of Poly(Styrene-Block-Ethylene Oxide) Polymers with Fluorescent-Probes at the Block Junctions. *Makromol Chem-M Symp*; 42-3: 463-473.
- [18]. A. Woodward, N. Sayresmith, J. Sailer, K. Sandor and M. Walter. 2019. Fluorescent thiazolothiazole viologen materials for energy storage: Photochemistry, electrochromism, and photoluminescence. *Abstr Pap Am Chem S*; 257.
- [19]. Z. Y. Zhang, Y. A. Chen, W. Y. Hung, W. F. Tang, Y. H. Hsu, C. L. Chen, F. Y. Meng and P. T. Chou. 2016. Control of the Reversibility of Excited-State Intramolecular Proton Transfer (ESIPT) Reaction: Host-Polarity Tuning White Organic Light Emitting Diode on a New Thiazolo[5,4-d]thiazole ESIPT System. *Chem Mater*; 28: 8815-8824.
- [20]. Q. Peng, J. B. Peng, E. T. Kang, K. G. Neoh and Y. Cao. 2005. Synthesis and electroluminescent properties of copolymers based on fluorene and 2,5-di(2-hexyloxyphenyl)thiazolothiazole. *Macromolecules*; 38: 7292-7298.
- [21]. S. Ando, J. Nishida, Y. Inoue, S. Tokito and Y. Yamashita. 2004. Synthesis, physical properties, and field-effect transistors of novel thiophene/thiazolothiazole co-oligomers. *J Mater Chem*; 14: 1787-1790.
- [22]. I. Osaka, G. Sauve, R. Zhang, T. Kowalewski and R. D. McCullough. 2007. Novel thiophene-thiazolothiazole copolymers for organic field-effect transistors. *Adv Mater*; 19: 4160-+.
- [23]. D. Bevk, L. Marin, L. Lutsen, D. Vanderzande and W. Maes. 2013. Thiazolo[5,4-d]thiazoles - promising building blocks in the synthesis of semiconductors for plastic electronics. *Rsc Adv*; 3: 11418-11431.
- [24]. G. Reginato, A. Mordini, L. Zani, M. Calamante and A. Dessi. 2016. Photoactive Compounds Based on the Thiazolo[5,4-d]thiazole Core and Their Application in Organic and Hybrid Photovoltaics. *Eur J Org Chem*; 2016: 233-251.
- [25]. Z. Dikmen and V. Bütün. 2021. Thiazolo thiazole based cross-linker to prepare highly fluorescent smart films with tunable emission wavelength and their multi-responsive usage. *European Polymer Journal*; 159: 110759.
- [26]. Z. Dikmen and V. Bütün. Multi-Analyte Sensitive Fluorophore Cross-Linked Nanofibers Based Antimicrobial Surface Enabling Bacterial Detection and Their Usage as Crystal Growth Template. *Macromolecular Materials and Engineering*; n/a: 2300226.
- [27]. O. Turhan, Z. Dikmen and V. Bütün. 2023. Novel approach to increase chemosensing ability of fluorophore via cross-linked hydrogel film formation. *Journal of Photochemistry and Photobiology A: Chemistry*; 443: 114828.
- [28]. Z. Dikmen, G. Dikmen and V. Bütün. 2023. Fluorophore-assisted green fabrication of flexible and cost-effective Ag nanoparticles decorated PVA nanofibers for SERS based trace detection. *Journal of Photochemistry and Photobiology A: Chemistry*; 445: 115074.
- [29]. Z. Dikmen, O. Turhan, A. Özbal and V. Bütün. 2022. In-situ formation of fluorophore cross-linked micellar thick films and usage as drug delivery material for Propranolol HCl. *Spectrochimica Acta Part A: Molecular and Biomolecular Spectroscopy*; 279: 121452.
- [30]. N. Yamada, H. Noguchi, Y. Orimoto, Y. Kuwahara, M. Takafuji, S. Pathan, R. Oda, A. Mohammadali Rahimli, M. Ahmed Ramazanov and H. Ihara. 2019. Emission-Color Control in Polymer Films by Memorized Fluorescence Solvatochromism in a New Class of Totally Organic Fluorescent Nanogel Particles. *Chemistry – A European Journal*; 25: 10141-10148.
- [31]. Y. Su, S. Z. F. Phua, Y. Li, X. Zhou, D. Jana, G. Liu, W. Q. Lim, W. K. Ong, C. Yang and Y. Zhao. 2018. Ultralong room temperature phosphorescence from amorphous organic materials toward confidential information encryption and decryption. *Sci Adv*; 4: eaas9732.
- [32]. Y. S. Soliman, A. A. Abdel-Fattah, A. A. Hamed and A. M. M. Bayomi. 2018. A radiation-sensitive monomer of 2,4-hexadiyn-1,6-bis(p-toluene sulphonyl urethane) in PVA as a radiochromic film dosimeter. *Radiat Phys Chem*; 144: 56-62.
- [33]. Z. Yu, B. Li, J. Chu and P. Zhang. 2018. Silica in situ enhanced PVA/chitosan biodegradable films for food packages. *Carbohydr Polym*; 184: 214-220.
- [34]. D. Kumar, S. Umrao, H. Mishra, R. R. Srivastava, M. Srivastava, A. Srivastava and S. K. Srivastava. 2017. Eu:Y2O3 highly dispersed fluorescent PVA film as turn off luminescent probe for enzyme free detection of H2O2. *Sensor Actuat B-Chem*; 247: 170-178.



- [35]. H. Kim and J. Y. Chang. 2014. Reversible Thermochromic Polymer Film Embedded with Fluorescent Organogel Nanofibers. *Langmuir*; 30: 13673-13679.
- [36]. G. Kwak, S. Fukao, M. Fujiki, T. Sakaguchi and T. Masuda. 2006. Temperature-Dependent, Static, and Dynamic Fluorescence Properties of Disubstituted Acetylene Polymer Films. *Chem Mater*; 18: 2081-2085.
- [37]. G. He, N. Yan, J. Y. Yang, H. Y. Wang, L. P. Ding, S. W. Yin and Y. Fang. 2011. Pyrene-Containing Conjugated Polymer-Based Fluorescent Films for Highly Sensitive and Selective Sensing of TNT in Aqueous Medium. *Macromolecules*; 44: 4759-4766.
- [38]. S.-J. Lim, B.-K. An and S. Y. Park. 2005. Bistable Photoswitching in the Film of Fluorescent Photochromic Polymer: Enhanced Fluorescence Emission and Its High Contrast Switching. *Macromolecules*; 38: 6236-6239.
- [39]. L. Carbone, C. Nobile, M. De Giorgi, F. D. Sala, G. Morello, P. Pompa, M. Hytch, E. Snoeck, A. Fiore, I. R. Franchini, M. Nadasan, A. F. Silvestre, L. Chiodo, S. Kudera, R. Cingolani, R. Krahne and L. Manna. 2007. Synthesis and Micrometer-Scale Assembly of Colloidal CdSe/CdS Nanorods Prepared by a Seeded Growth Approach. *Nano Letters*; 7: 2942-2950.
- [40]. Z. Dikmen. 2024. Gold-tipped CdSe/CdZnS colloidal quantum wells as non-quenching plasmonic particles for optical applications. *Optical Materials*; 147: 114761.
- [41]. X. Peng, M. C. Schlamp, A. V. Kadavanich and A. P. Alivisatos. 1997. Epitaxial Growth of Highly Luminescent CdSe/CdS Core/Shell Nanocrystals with Photostability and Electronic Accessibility. *Journal of the American Chemical Society*; 119: 7019-7029.
- [42]. T. Duan, J. Ai, X. Cui, X. Feng, Y. Duan, L. Han, J. Jiang and S. Che. 2021. Spontaneous chiral self-assembly of CdSe@CdS nanorods. *Chem*; 7: 2695-2707.
- [43]. W.-C. Wang, H.-Y. Wang, T.-Y. Chen, C.-T. Tsai, C.-H. Cheng, H.-C. Kuo and G.-R. Lin. 2019. CdSe/ZnS core-shell quantum dot assisted color conversion of violet laser diode for white lighting communication. *Nanophotonics*; 8: 2189-2201.
- [44]. N. Yin, S. Zhao, P. Li and L. Liu. 2018. One-pot synthesis of Ag nanoparticle/Ag-doped SiO<sub>2</sub> composite film and their enhancement effect for CdSe QDs. *Functional Materials Letters*; 11: 1950008.
- [45]. J. Wang, C. Guo, Y. Yu, H. Yin, X. Liu and Y. Jiang. 2015. Self-doped 3-hexylthiophene-b-sodium styrene sulfonate block copolymer: synthesis and its organization with CdSe quantum dots. *RSC Advances*; 5: 17905-17914.
- [46]. A. T. Isik, F. Shabani, F. Isik, S. Kumar, S. Delikanli and H. V. Demir. 2023. Simultaneous Dual-Color Amplified Spontaneous Emission and Lasing from Colloidal Quantum Well Gain Media in their Own Layered Waveguide and Cavity. *Laser & Photonics Reviews*; 17: 2300091.
- [47]. M. Athanasiou, R. M. Smith, J. Pugh, Y. Gong, M. J. Cryan and T. Wang. 2017. Monolithically multi-color lasing from an InGaN microdisk on a Si substrate. *Scientific Reports*; 7: 10086.
- [48]. M. Schubert, L. Woolfson, I. R. M. Barnard, A. M. Dorward, B. Casement, A. Morton, G. B. Robertson, P. L. Appleton, G. B. Miles, C. S. Tucker, S. J. Pitt and M. C. Gather. 2020. Monitoring contractility in cardiac tissue with cellular resolution using biointegrated microlasers. *Nature Photonics*; 14: 452-458.
- [49]. S. Han, W. Zhang, B. Qiu, H. Dong, W. Chen, M. Chu, Y. Liu, X. Yang, F. Hu and Y. S. Zhao. 2018. Controlled Assembly of Organic Composite Microdisk/Microwire Heterostructures for Output Coupling of Dual-Color Lasers. *Advanced Optical Materials*; 6: 1701077.
- [50]. T. Pan, D. Lu, H. Xin and B. Li. 2021. Biophotonic probes for bio-detection and imaging. *Light: Science & Applications*; 10: 124.
- [51]. C. Tapeinos, E. K. Efthimiadou, N. Boukos, C. A. Charitidis, M. Koklioti and G. Kordas. 2013. Microspheres as therapeutic delivery agents: synthesis and biological evaluation of pH responsiveness. *Journal of Materials Chemistry B*; 1: 194-203.

# Electrical Characteristics of Cadmium Sulfide/4-Amino-2-Methylquinoline Heterojunction Structure

Ramazan Demir<sup>1\*</sup> , İsmet Kaya<sup>2</sup> 

<sup>1</sup> Çanakkale Onsekiz Mart University, Vocational School of Technical Science, Çanakkale, Türkiye

<sup>2</sup> Çanakkale Onsekiz Mart University, Faculty of Science, Department of Chemistry, Polymer Synthesis and Analysis Laboratory, Çanakkale, Türkiye

\* [rdemir@comu.edu.tr](mailto:rdemir@comu.edu.tr)

\* Orcid No: 0000-0003-4130-4927

Received: 26 November 2023

Accepted: 13 March 2024

DOI: 10.18466/cbayarfbe.1396129

## Abstract

We fabricated a heterojunction structure composed of n-CdS and p-C<sub>10</sub>H<sub>10</sub>N<sub>2</sub> films. The CdS film was prepared using the CBD method, while the C<sub>10</sub>H<sub>10</sub>N<sub>2</sub> film was prepared using the spin coating method. Later, we performed the current-voltage (*I-V*) measurement of this PN diode which we made using Keithley 2400 sourcemeter. As can be seen from the *logI-V* diagram, this heterojunction structure exhibits rectifying properties. Using traditional methods, an ideality factor (*n*) of 1.93 and a barrier height value ( $\Phi_b$ ) of 0.79 eV were determined. An ideality factor of more than one indicates non-ideal *I-V* behavior in the CdS/C<sub>10</sub>H<sub>10</sub>N<sub>2</sub> heterojunction diode formed. The interface layer, interface states and series resistance are some of the causes of this deviation. Moreover, Cheung's functions and a modified Norde function were used to determine the diode parameters, such as ideality factor, barrier height, and series resistance. With the Cheung method, *n*=4.33, series resistance (*R<sub>S</sub>*)=168.65 kΩ and  $\Phi_b$ =0.62 eV were found. Additionally, *R<sub>S</sub>*=686.08 kΩ and  $\Phi_b$ =0.78 eV were found by the Norde method. Consistent barrier height values were found in all methods through comparison, suggesting compatibility. However, it was discovered that the series resistance values yielded by the Norde function exceeded those obtained by the Cheung functions.

**Keywords:** 4-Amino-2-Methylquinoline, C<sub>10</sub>H<sub>10</sub>N<sub>2</sub>, CdS, Heterojunction Diode, Thin Film

## 1. Introduction

Currently, there is a growing interest in II-VI semiconductor materials due to their potential applications in the optoelectronic and photovoltaic industries. One particularly promising option is the thin film of cadmium sulfide (CdS), which is an n-type chalcogenide semiconductor with a direct energy band gap ranging from 2.28 eV to 2.45 eV. These thin films possess unique structural, optical, and electrical properties that differ greatly from those of bulk materials. As a result, they are used in various technologies, including solar cell window layers, optical sensors, transistors, diodes, and more. Different methods, such as electro-deposition, spray pyrolysis, successive ionic layer adsorption and reaction (SILAR), pulsed-laser deposition, vacuum evaporation, and chemical bath deposition (CBD), are employed to produce CdS thin films [1, 2].

A quinoline derivative, or 4-amino-2-methylquinoline (4-aminoquinoline), is an organic compound with amine and methyl functional groups [3]. 4-amino-2-methylquinoline (C<sub>10</sub>H<sub>10</sub>N<sub>2</sub>) is a quinoline derivative to have similar to structure such as naphthalene and 4-aminoquinoline [4]. Aminoquinolines are important as building blocks for the production of medicines and dyes, which are mostly used to prevent different illnesses [5, 6].

In this study, we used the CBD method to produce thin films of CdS. We then used the spin-coating technique to produce 4-amino-2-methylquinoline (C<sub>10</sub>H<sub>10</sub>N<sub>2</sub>) films. A Keithley 2400 sourcemeter was used to record the electrical characteristics of the diodes in an atmospheric environment.

## 2. Materials and Methods

### 2.1. Materials and Synthesis methods

In this study, a Keithley 2400 sourcemeter was used to characterize the diodes electrically in an atmospheric setting. A thin layer of CdS was applied using the CBD method to a 76 x 26 x 1 mm<sup>3</sup> indium tin oxide (ITO) substrate. The substrates were cleaned by rinsing them with ethanol and deionized water after being washed with a soap solution. After another rinse in deionized water, they were let to air dry. In order to deposit thin CdS films, a solution was made up of 8 mL of ammonia/ammonium chloride buffer solution (NH<sub>3</sub>/NH<sub>4</sub>Cl; pH=11.50), 1 M 10 mL thiourea (CS(NH<sub>2</sub>)<sub>2</sub>), and 0.2 M 10 mL cadmium acetate dihydrate (Cd(CH<sub>3</sub>COO)<sub>2</sub> 2H<sub>2</sub>O). The mixture was then diluted with deionized water to reach a total volume of 50 ml. Thiourea was selected as the sulfur source (S), 82 °C was set as the solution temperature, and 60 minutes was the deposition time in order to prepare the CdS film [1, 2, 7]. After gathering in this manner, the CdS/ITO films were annealed for 30 minutes at 350 °C in room temperature.

CdS is categorized as an n-type semiconductor material [8], whereas C<sub>10</sub>H<sub>10</sub>N<sub>2</sub> behaves like a p-type semiconductor material, similar to 8-hydroxyquinoline (8HQ) [9], because they share functional groups. C<sub>10</sub>H<sub>10</sub>N<sub>2</sub> has an optical band gap energy of 3.5 eV [10].

It's time to finish the experiment's second step, which involves creating a diode by filming a C<sub>10</sub>H<sub>10</sub>N<sub>2</sub> layer on a CdS film. The C<sub>10</sub>H<sub>10</sub>N<sub>2</sub> film was prepared by dissolving powdered C<sub>10</sub>H<sub>10</sub>N<sub>2</sub> with a molecular weight of 158.20 g/mol in ethanol for 90 minutes at room temperature (22 °C). This solution was then used in the spin-coating process. There were 0.2 M of solution concentration and 30 mL of total solution volume. Using a plastic dropper, 10 drops of C<sub>10</sub>H<sub>10</sub>N<sub>2</sub> solution were applied to the CdS film prior to each rotation. The spin coater was attached to the CdS film that a C<sub>10</sub>H<sub>10</sub>N<sub>2</sub> solution was dropped onto. The spin coater was then turned on. The resulting film was allowed to stand at room temperature for five minutes after the spin coater was turned off after sixty seconds. The spin coater was restarted after five minutes, and the procedure was carried out eight times. The spin coater rotates at a speed of 1100 rpm for one minute during each rotation. As a result, a C<sub>10</sub>H<sub>10</sub>N<sub>2</sub> film was applied to the CdS film that had previously been prepared on ITO.

### 2.2. Electrical Characterization of the Heterojunction Structure

Using a Keithley 2400 sourcemeter, the electrical properties of the CdS/C<sub>10</sub>H<sub>10</sub>N<sub>2</sub> diodes were thoroughly characterized in this study.

## 3. Results and Discussion

As shown in Figure 1, electrical conductivity measurements were made on CdS/C<sub>10</sub>H<sub>10</sub>N<sub>2</sub> heterojunction structures using a two-point probe technique and a Keithley 2400 sourcemeter device. By using specialized computer software that was connected to the Keithley 2400 sourcemeter, current (*I*) values corresponding to applied voltage (*V*) were recorded. By applying a direct voltage (*V*) between -3 and 3 volts, the current (*I*) was obtained. Investigating the photosensitivity of the heterojunction diode we created was not the aim of this study. Because of this, *I-V* measurements were only carried out in the daytime at a temperature of 22 °C in a laboratory setting.

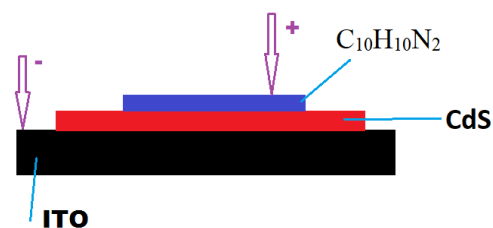


**Figure 1.** Measurement of electrical conductivity of CdS/C<sub>10</sub>H<sub>10</sub>N<sub>2</sub> heterojunction structure

Forward and reverse *I-V* measurements were made in the range of ± 3 V to ascertain the electrical properties of the sample; the corresponding graphics are displayed in Figures 2 and 3. These graphs demonstrate that the sample has a rectifying property and a potential barrier at the *I-V* interface.

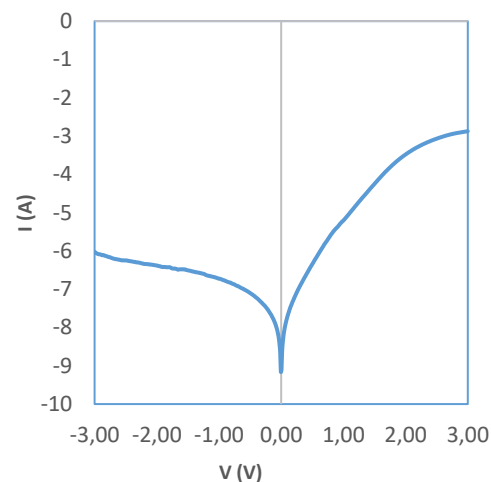


**Figure 2.** Semi-logarithmic reverse and forward bias *I-V* characteristics of CdS/C<sub>10</sub>H<sub>10</sub>N<sub>2</sub> heterojunction structure at room temperature

The unique current-voltage characteristic of the CdS/C<sub>10</sub>H<sub>10</sub>N<sub>2</sub> heterojunction diode is shown in Figure 2. When the voltage increases exponentially, the forward diode current also increases, indicating that the diode is rectifying. This suggests that a Schottky diode is analogous to how the heterojunction diode functions. The following formula 3.1 can be used to analyze the CdS/C<sub>10</sub>H<sub>10</sub>N<sub>2</sub> diode's current-voltage characteristics.

The electrical *I-V* characteristic of the n-CdS/4-amino-2-methylquinoline contact at room temperature was used in this study to obtain and compare diode parameters such as the ideality factor (*n*), barrier height ( $\Phi_b$ ), and series resistance value (*R<sub>S</sub>*) of the structure. The Norde, Cheung Function, and conventional bias forward *I-V* approaches were applied for this. Similar to the *R<sub>S</sub>* series resistance, the *R<sub>sh</sub>* shunt resistance has also been calculated and published in a few places [11]. Here, we are only concerned with *R<sub>S</sub>*'s series resistance computation.

The relationship between the voltage applied to the contact and the current flowing through a Schottky barrier is given by Equation 3.1, which takes into account the series resistance (*R<sub>S</sub>*) effect. This is expressed as follows:

$$I = I_0 \left[ \exp \left( q \frac{(V - IR_S)}{nkT} - 1 \right) \right] \quad (3.1)$$

The ideality factor, denoted by *n*, has a value of 1 for an ideal diode. The value of 1 in parenthesis can be ignored in the equation if  $V > 3kT/q$ . *T* is the ambient temperature in Kelvin, *I<sub>0</sub>* is the extrapolated saturation current value, and *k* is the Boltzmann constant in this expression.

Here,

$$I_0 = AA^*T^2 \exp \left( - \frac{\Phi_{b0}}{kT} \right) \quad (3.2)$$

given in the form. *q* is the fundamental electric charge ( $=1.6 \times 10^{-19}$  C), *V* applied voltage, *A* diode area ( $10.00 \times 10^{-3}$  cm<sup>2</sup>), *A\** effective Richardson constant for CdS is  $45 \text{ Acm}^{-2}\text{K}^{-2}$  [12].

Using Equation 3.1 to calculate the ideality factors of the diodes, the following expression can be obtained:

$$n = \frac{q}{kT} \frac{dV}{d(\ln I)} \quad (3.3)$$

The value of the term  $\frac{dV}{d(\ln I)}$  in this expression is obtained by measuring the slope of the linear portion on the right-bias side of Figure 3's *lnI-V* graph.

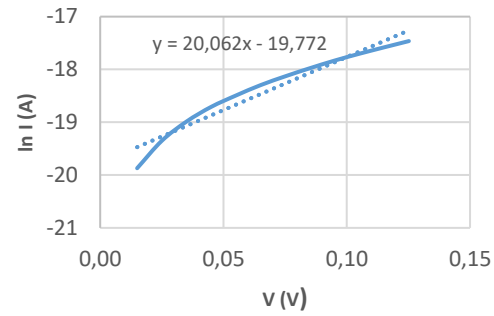


**Figure 3.** *lnI-V* characteristic of CdS/C<sub>10</sub>H<sub>10</sub>N<sub>2</sub> heterojunction diode in the range of 0.00 V- 0.13 V

The zero feed barrier height can be expressed as follows when equation 3.2 is rearranged:

$$\Phi_{b0} = \frac{kT}{q} \ln \left( \frac{AA^*T^2}{I_0} \right) \quad (3.4)$$

As demonstrated in Figure 3, the *lnI-V* graph has been fitted linearly using the so-called traditional *I-V* method; diode parameters *n*, *I<sub>0</sub>* and  $\Phi_{b0}$  are obtained with the aid of equations 3.2, 3.3, and 3.4. These parameters are 1.93, respectively; it was discovered to be  $2.64 \times 10^{-9}$  A and 0.79 eV. Table 1 lists the electrical characteristics that were acquired using conventional techniques.

**Table 1.** Electrical Characteristics Obtained by Traditional Methods

	<b>n</b>	<b>I<sub>0</sub> (A)</b>	<b>Φ<sub>b</sub> (eV)</b>
<b>I-V :</b>	1.93	$2.64 \times 10^{-9}$	0.79

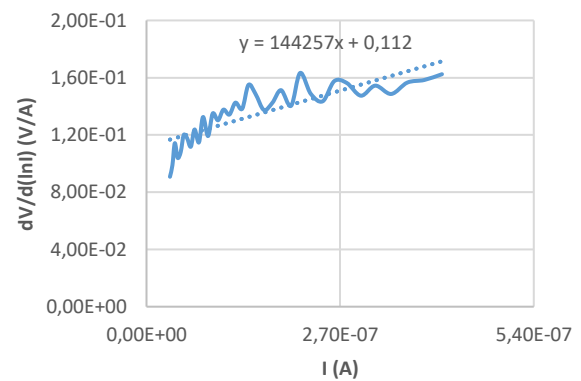


**Figure 4.** *dV/d(lnI)-I* graph of CdS/C<sub>10</sub>H<sub>10</sub>N<sub>2</sub> heterojunction diode at room temperature

In the literature, equations 3.5, 3.6, and 3.7 that are derived by taking into account the fundamental current equation 3.1 are referred to as Cheung functions [13]. In

addition to  $R_S$ , values for  $n$  and  $\Phi_b$  were also obtained using these equations.

$$\frac{dV}{d(\ln I)} = IR_S + \frac{nkT}{q} \quad (3.5)$$

$$H(I) = V - \frac{nkT}{q} \ln\left(\frac{I}{AA^*T^2}\right) \quad (3.6)$$

$$H(I) = IR_S + n\Phi_b \quad (3.7)$$

Figure 4 displays the  $dV/d(\ln I)$ - $I$  graph of the sample's Cheung functions. Here, as Equation 3.5 makes abundantly evident, the line's slope indicates the value of  $R_S$ , and the point where the line crosses the vertical axis indicates the value of  $nkT/q$ . Thus, the diode's  $n$  value is 4.33, and the value of  $R_S$  was found to be 144.26 k $\Omega$ . Table 2 presents the electrical characteristics that were obtained using Cheung methods.

**Table 2.** Electrical Characteristics Obtained by Cheung Methods

	$n$	$R_s$ (k $\Omega$ )	$\Phi_b$ (eV)
<b>dV/dlnI-I :</b>	4.33	144.26	
<b>H(I)-I :</b>		168.65	0.62

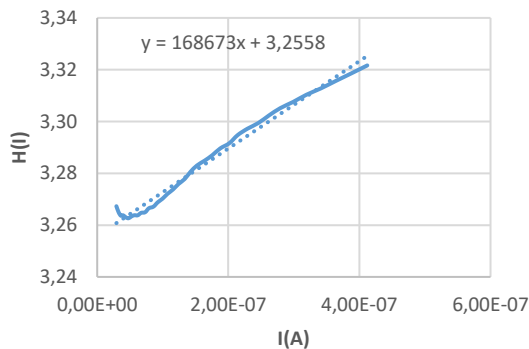


**Figure 5.** H(I)-I plot of CdS/C<sub>10</sub>H<sub>10</sub>N<sub>2</sub> heterojunction diode at room temperature

Figures 4 and 5 show an analysis of the Cheung function curves derived from the data in the nonlinear region of the CdS/C<sub>10</sub>H<sub>10</sub>N<sub>2</sub> Schottky diode's  $I$ - $V$  curve. The diode's  $H(I)$ - $I$  graph is drawn while taking Equation 3.6's Cheung function into account. Equation 3.7 was used to obtain  $\Phi_b$  and  $R_S$  values after a linear fit was made to the  $H(I)$ - $I$  graph shown in Figure 5. From this point on, the series resistance value was 168.65 k $\Omega$  and the barrier height value was 0.62 eV.

In addition, Norde put forth a different approach for figuring out the series resistance. The modified Norde method [14-16] defines the following function:

$$F(V) = \frac{V}{\gamma} - \frac{kT}{q} \ln\left(\frac{I(V)}{AA^*T^2}\right) \quad (3.8)$$

In this case,  $\gamma$  stands for a dimensionless integer larger than the ideality factor ( $\gamma > n$ ). According to this method, the barrier height and series resistance values can be obtained by applying the following relationships after locating the minimum point on the  $F(V)$  versus  $V$  plot:

$$\Phi_{b0} = F(V_0) + \frac{V_0}{\gamma} - \frac{kT}{q} \quad (3.9)$$

From the Norde functions,  $R_S$  value can be established as:

$$R_0 = \frac{kT(\gamma-n)}{qI_0} \quad (3.10)$$

Here, the corresponding bias voltage and current are indicated by  $V_0$  and  $I_0$ , respectively, and the minimum point on the  $F(V)$  versus  $V$  plot is represented by  $F(V_0)$ .

Figure 6 shows the  $F(V)$  - $V$  plot of the structure.

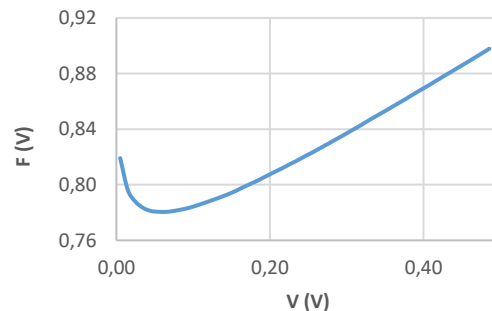


**Figure 6.**  $F(V)$ - $V$  plot of CdS/C<sub>10</sub>H<sub>10</sub>N<sub>2</sub> heterojunction diode at room temperature.

Using Eq. (3.9) and (3.10), from the  $F(V)$ - $V$  plot, the parameters of the structure were determined as  $\Phi_b = 0.78$  eV,  $R_S = 686.08$  k $\Omega$  by using  $F(V_0) = 0.78$  V,  $V_0 = 0.06$  V values. Electrical characteristics obtained by Norde methods are given in Table 3.

**Table 3.** Electrical Characteristics Obtained by Norde Methods

	$R_s$ (k $\Omega$ )	$\Phi_b$ (eV)
<b>F(V) -V :</b>	686.08	0.78

Table 2 makes it evident that the  $R_s$  values derived from the  $dV/d\ln I$ - $I$  and  $H(I)$ - $I$  lines were relatively near to one another. This shows that Cheung functions are

compatible. A diode's series resistance can originate from various sources. The development of an insulating layer between the metal and semiconductor interface and the diodes' series resistance are particularly important factors that affect the performance and dependability of these diodes [17]. Several factors contribute to this, including the resistance of the semiconductor, the contact resistance of the metals deposited on it, the distribution of interface states, and the presence of an insulator between the semiconductor and the metal. The  $dV/dlnI-I$  graph in Table 2 yielded a value for  $n=4.33$  that is higher than the value obtained using the conventional method. The Cheung functions take into account a different area of the  $I-V$  curve, which is one of the causes of this discrepancy. The data from the nonlinear region of the  $I-V$  characteristic is used by Cheung functions.

#### 4. Conclusion

We have produced a  $CdS/C_{10}H_{10}N_2$  heterojunction diode for our investigation. By using forward bias  $I-V$ , Cheung's functions, and Norde's functions, the electronic parameters of the Schottky diode, such as ideality factor, barrier height, and series resistance, were extracted. The series resistance values acquired using each method differ from one another, but they generally agree with the barrier height values.

At room temperature, it was discovered that the  $I-V$  characteristic of  $CdS/C_{10}H_{10}N_2$  exhibited rectifying behavior, with an ideality factor value of 1.93 and a barrier height value of 0.79 eV. The  $n$  value is greater than one. This indicates that the diode is exhibiting non-ideal behavior. Among the factors contributing to this deviation are the interface layer, interface states, and series resistance. Moreover, the ideality factor, barrier height, and series resistance of the diode were ascertained using Cheung's functions and a modified Norde function. With the Cheung method,  $n=4.33$ ,  $R_s=168.65$  k $\Omega$  and  $\Phi_b=0.62$  eV were found. Additionally,  $R_s=686.08$  k $\Omega$  and  $\Phi_b=0.78$  eV were found by the Norde method.

Comparison of all approaches revealed consistent barrier height values, indicating compatibility. The series resistance values produced by the Norde function, however, were found to be higher than those produced by the Cheung functions. With our study, we aimed to introduce the electrical properties of an organic compound,  $C_{10}H_{10}N_2$ , and an inorganic compound,  $CdS$ , as a diode, which has not been encountered previously in the literature.

#### Author's Contributions

**Ramazan Demir:** He produced and investigated the  $CdS$  film and heterojunction structure.

**İsmet Kaya:** He investigated some properties of the substance 4-amino-2-methylquinoline.

R. Demir and İ. Kaya revised the manuscript; and all authors read and approved the final manuscript.

#### Ethics

There are no ethical issues after the publication of this manuscript.

#### References

- [1]. Demir, R. and F. Gode, *Structural, optical and electrical properties of nanocrystalline CdS thin films grown by chemical bath deposition method*. Chalcogenide Letters, 2015. 12: p. 43-50.
- [2]. Demir, R. and F. Göde, *Preparation and Characterization of Polycrystalline CdS Thin Films Deposited by Chemical Bath Deposition*. Materials Focus, 2018. 7(3): p. 351-355.
- [3]. Braun, D.E., et al., *Solid state forms of 4-aminoquinoline - From void structures with and without solvent inclusion to close packing*. CrystEngComm, 2015. 17(12): p. 2504-2516.
- [4]. Puviarasan N., A.V., Mohan S., *FTIR and FT-Raman Spectral Investigations on 4-Aminoquinoline and 5-Aminoquinoline*. Turk J Chem, 2004. 28: p. 53-65.
- [5]. Arjunan, V., et al., *Ab initio, density functional theory and structural studies of 4-amino-2-methylquinoline*. Spectrochim Acta A Mol Biomol Spectrosc, 2009. 74(2): p. 375-84.
- [6]. Kovi Peter J., C.A.C., Schulman Stephen G., *Electronic Spectra of 2-Aminoquinoline and 4-Aminoquinoline Evidence for the Cyclic Amidine Structures of the Singly Protonated Cations*. Analytical Chemistry, 1972. 44: p. 1611-1615.
- [7]. Demir, R. and İ. Kaya, *Comparison of electrical characteristics of zinc oxide and cadmium sulfide films covered with 8-hydroxyquinoline for diode applications*. Journal of Materials Science: Materials in Electronics, 2019. 30(7): p. 7103-7109.
- [8]. Aybek A. Ş., R.H., *Some Physical Properties of FTO/n-CdS/Au Structure*. Chalcogenide Letters, 2018. 15: p. 583-590.
- [9]. Demir, H.Ö., et al., *Synthesis, characterization and diode application of poly(4-(1-(2-phenylhydrazono)ethyl)phenol)*. Journal of Materials Chemistry C, 2015. 3(22): p. 5803-5810.
- [10]. Kaya, İ., et al., *Synthesis and characterization of imine polymers of aromatic aldehydes with 4-amino-2-methylquinoline via oxidative polycondensation*. Designed Monomers and Polymers, 2015. 18(1): p. 89-104.
- [11]. Coşkun, E., et al., *Device behavior of an In/p-Ag(Ga,In)Te2/n-Si/Ag heterojunction diode*. Materials Science in Semiconductor Processing, 2015. 34: p. 138-145.
- [12]. Dey, S.K., S. Baglari, and D. Sarkar, *Junction characteristics of ITO/PANI-ZnS/Ag and ITO/PANI-CdS/Ag Schottky diodes: a comparative study*. Indian Journal of Physics, 2015. 90(1): p. 29-34.
- [13]. Cheung, S.K. and N.W. Cheung, *Extraction of Schottky diode parameters from forward current-voltage characteristics*. Applied Physics Letters, 1986. 49(2): p. 85-87.
- [14]. Norde, H., *A modified forward I-V plot for Schottky diodes with high series resistance*. Journal of Applied Physics, 1979. 50(7): p. 5052-5053.



- [15]. Turut, A., *Determination of barrier height temperature coefficient by Norde's method in ideal Co/n-GaAs Schottky contacts*. Turkish Journal of Physics, 2012.
- [16]. Karataş, Ş. and F. Yakuphanoglu, *Analysis of electronic parameters of nanostructure copper doped cadmium oxide/p-silicon heterojunction*. Journal of Alloys and Compounds, 2012. 537: p. 6-11.
- [17]. Karataş, Ş. and F. Yakuphanoglu, *Effects of illumination on electrical parameters of Ag/n-CdO/p-Si diode*. Materials Chemistry and Physics, 2013. 138: p. 72-77.

# Deep Rolling of Al6061-T6 Material and Performance Evaluation with New Type Designed WNMG Formed Rolling Tool

Oktaı Adıyaman<sup>1\*</sup> , Feyza AYDIN<sup>2</sup> 

<sup>1,2</sup> Batman University, Institute Of Graduate Studies, Batman, Türkiye

\*[oktay.adiyaman@batman.edu.tr](mailto:oktay.adiyaman@batman.edu.tr)

\* Orcid No: 0000-0002-2674-3836

Received: 17 December 2023

Accepted: 15 March 2024

DOI: 10.18466/cbayarfbe.1405976

## Abstract

In deep rolling, ball and roller type burnishing tools are generally used. It is generally difficult to deep roll contours with curved and conical shapes with the existing rolling tools. The aim of this study is to design experiments with a roller insert that will be an alternative to deep rolling inserts being used now and that can be fixed on the present tool holders; and to investigate the usability of them including curve and conical formed workpieces with the help of this designed tool. For this purpose, a spherical insert with a radius of 1 mm in the form of WNMG was designed based on the WNMG insert model and used in deep rolling of Al6061-T6 material using different forms and parameters. 143, 330, 495 N rolling force, 0.04, 0.08, 0.12 mm/rev feed and 400, 600, 800 rpm spindle speed were selected as rolling parameters. By examining the microhardness and surface structure of deep-rolled Al6061 parts, the achievability of the results of existing tools in deep rolling was investigated. At the end of the study, it was determined that the new type of rolling tool produced results similar to the existing tools in deep rolling in terms of microhardness and surface morphology, which enabled that the workpieces with curve and conical forms could also be rolled, and that this rolling tool could be used as an alternative in deep rolling.

**Keywords:** Al6061, deep rolling, microhardness, surface roughness, tribology

## 1. Introduction

In order to correct the negative effects on the machined surfaces of the materials, many finishing applications such as grinding, honing, lapping [1], and ultrasound-aided deep rolling [2] are used. Prabhu et al. divided the methods applied for surface smoothing into two main categories. The first of these is the method that involves material loss, such as grinding method, while the second is the method that works by redistributing the material on the surface and plastic compression of the surface and does not involve material loss, such as ball burning and deep rolling methods [3].

The process of smoothing the surfaces of the machined parts by rolling them without removing any chips from their surfaces is defined as rolling. After the rolling process, the surface quality (Ra, etc.) of the work pieces is improved, as well as the mechanical properties of the workpieces, such as microhardness, fatigue resistance, wear resistance. Thanks to this treatment role of the rolling process, this method is preferred more than the

other surface improvement methods such as grinding [4]. In order to improve the surfaces of the machined elements, the deep rolling technique, which is based on the plastic deformation of the surfaces without removing the chips by means of a rolling insert or roller, is mostly applied to the inner and outer surfaces of the turned and ground workpieces [5, 6]. As a result of the process, the surface roughness (Ra) of the material decreases significantly, and the surface hardness increases. Additionally, at the end of the process, the tensile strength on the surface turns into compressive stresses, resulting in a high improvement in fatigue life [7]. Deep rolling process can be applied to steel materials as well as other light metals (brass, aluminum (Al), etc.).

In addition to the studies investigating the effect of process parameters on the results, there are also similar studies on the tools used in rolling. For this purpose, the effects of three different apparatus designed for using different parameters (rolling force, feed and number of passes) and the process parameters were investigated, and compared depending on the surface hardness and Ra

of Al-6061-T6 material. It was observed that the best Ra and surface hardness values were obtained with the apparatus with a ball-rolling insert [4].

Studies on deep and ball rolling were also applied to aluminum and its alloys. Analysis and research were carried out on the application of the rolling process of Al and its alloys, both on cylindrical surfaces in turning applications [8-14] and on planar surfaces in milling applications [15-17]. The circularity of the inner surfaces of hole was examined and compared with the machining methods in terms of Ra after rolling [18]. In another similar study [19], changes in Ra, microstructure and surface hardness of the inner surface of the hole of Al-6061 alloy were compared as a result of different machining methods such as drilling, internal turning, hole-grinding, honing, reaming and deep rolling processes. In addition, the effects of the process parameters (rolling pressure and number of passes) applied in the rolling method on fatigue, residual stress, microhardness and Ra were investigated experimentally. It was determined that ball rolling method improved the Ra; and the number of passes had a 41% effect on Ra. It was determined that the applied force and number of passes increased the microhardness of the material, and depending on the increase in force and number of passes, the microhardness of the workpiece increased by approximately 20 Hv. It was established that with the increase in rolling force, the subsurface residual stress in the material also increased. It was seen that not only the fatigue strength was improved but also the fatigue life was increased [18]. In addition to the effect of process parameters on the results, there are also similar studies on the tools used in rolling. For this purpose, the effects of three different apparatus designed for using different parameters (rolling force, feed and number of passes) and the process parameters were investigated and compared depending on the surface hardness and surface roughness of Al-6061-T6 material. It was observed that the best Ra and surface hardness were obtained with the apparatus with a ball-rolling insert [4]. In a different study, the effect of the rolling insert at different diameters was examined, and the surface of 5083 Al-Mg material was subjected to rolling using different parameters with ball diameters of 11.112 mm, 13.494 mm, 15.081 mm and 16.669 mm [20]. Regarding the rolling process applied in the form of milling application, the polishing process was carried out by using different process parameters with a simple rolling tool [21], and the resulting residual stresses were examined and the results were compared with the results in the numerical analysis program. It was established that there were compressive residual stresses on all rolled surfaces. Besides the process parameters, the effect of rolling direction and lubricant usage was also examined.

The analysis of the method continues in many different ways such as studies on deep rolling including simulation studies [22], analysis of deep rolling with the finite

element method [23,24], testing of deep rolling applications in different working environments (e.g. cryogenic) [23] and deep rolling with rolling tools of different diameters using methods such as regression, response surface method (RSM), ANOVA etc. [3, 25-30], Blasón et al. examined the strength increase of D38MnV5 S steel with a roller type toll [31].

There are many parameters that affect the results obtained in deep rolling method. It is both difficult and complex to examine the effects of these parameters on each mechanical property of the material simultaneously. In order to save time and cost in studies, Taguchi orthogonal experimental design method is one of the preferred methods instead of full factorial experimental design [7, 32, 3]. With Taguchi DOE, the number of experiments can be reduced and the effect of the parameters on the results can be examined. In addition, the subject can be examined with analyzes such as Artificial Neural Networks (ANN) [27], Response Surface Methodology (RSM) etc. [33].

When all previous studies were examined, it was observed that in majority of the studies, ball and roller type rolling tools were used; and generally, flat contours were deep rolled. In a previous study [34, 35], deep rolling process was applied to Al6061-T6 material with the designed rolling tool; thus, the effect of rolling parameters (speed, rolling pressure and feed) on the surface roughness obtained on conical and cylindrical surfaces was investigated. In this study, deep rolling process was applied to the cylindrical and conical surfaces of Al6061-T6 material with the designed and manufactured rolling insert, and as a result, the effects of the parameters on microhardness and surface morphology were investigated.

## 2. Materials and Methods

All turning operations were performed on a SMARC model CAK6166B X 200 CNC lathe. According to process, planning and process steps are shown in Figure 1.

The design of the rolling tool was referenced on WNMG 080408 type insert used in the industry, and a WNMG type rolling insert with a spherical nose shape and 1 mm radius was manufactured. Polishing process was applied to the spherical nose and friction was minimized (Figure 2).

A special tool holding apparatus was designed to fix the spherical edged rolling insert with the radius shown in Figure 2, and the tool holder to which this insert will be mounted to the turret of the CNC lathe machine for use in deep rolling with different rolling pressures (Figure 3 a), and then rolling process was carried out. (Figure 3 b). The rolling force was adjusted by moving the pressure adjustment spring length with the pre-load thread (Figure 3 a).

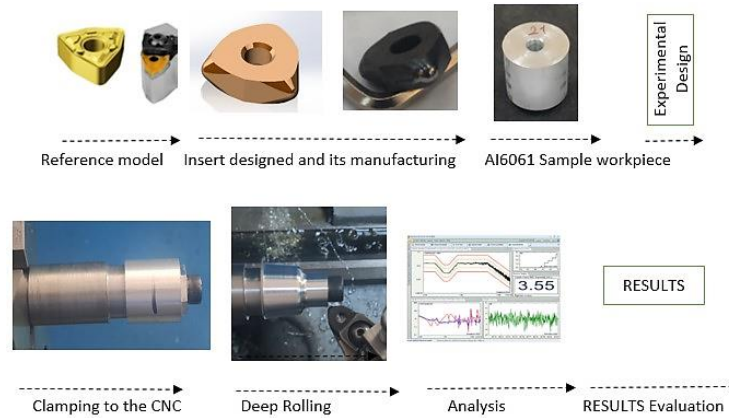


**Figure 1.** Schematic figure of the experimental setup and process steps



**Figure 2.** Designed insert, its manufacturing and assembling on the tool holder

The spring length and the pressure forces that can be obtained were determined by considering the tables suggested by the company [36]. In order to measure the mechanical properties and obtain accurate results, samples of appropriate sizes and dimensions were prepared. The process rolling parameters to be applied in the experiments are given in Table 1.

**Table 1.** Parameters and levels

Parameters	Level 1	Level 2	Level 3
Rolling Force (N)	143	330	495
Feed (mm/rev)	0.04	0.08	0.12
Spindle Speed (rpm)	400	600	800
Number of Pass	1		
Rolling conditions	Coolant (Lubricant)		

SKF LUBRIFLUID brand synthetic universal lubricant was used in the experiments. This lubricant is a new kind of coolant, lubricant and thin film spray lubricant, which does not contain mineral oils or chlorine. The properties of the lubricant are given in Table 2.

**Table 2.** Properties of lubricant [37]

Color	Flashpoint	Viscosity 40 °C	Density 20 °C
Light	184 °C	25 mm <sup>2</sup> /s	0.84 g/ml

The Taguchi method is a powerful, high-quality experimental design tool. Through this method, using a simple, effective, and systematic approach, the optimal burnishing parameters and robust-quality parameter setting can be derived. Furthermore, though incurring

minimum experimental cost, this approach improved the quality characteristics rapidly and efficiently by reducing the effect of the source of variation. Many successful applications of Taguchi methods have been reported to improve several processes and product reliability and quality [38, 39, 40].

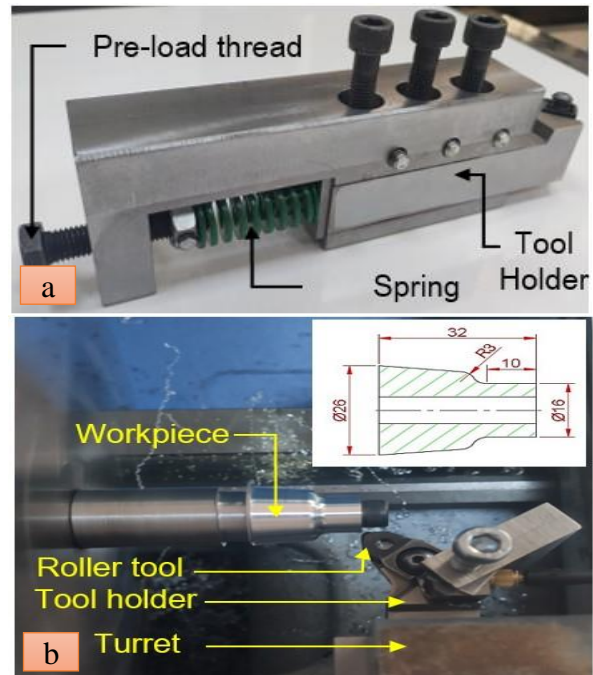


**Figure 3.** Deep rolling a) Tool holder apparatus b) Deep rolling process

In this paper, Taguchi experimental design was preferred as the experimental design and analysis method. L27 orthogonal design was used in the experiments and combinations were created. Three parameters in total and, in connection with them, 3 levels were determined for each parameter (Table 3). For the microhardness measurements of the test samples, samples were taken from cylindrical and conical surfaces and the microhardness values of these samples were measured with AOB brand Vickers microhardness device. Measurements were taken according to the Vickers hardness measurement method and applied under a load of 30 g. On each sample, 3 hardness measurements of cylindrical and conical surfaces from different points (Figure 4 a) and 3 measurements were taken from the radial, and then the arithmetic mean of these values was recorded as the hardness value of that sample (Figure 4).

**Table 3.** L27 experimental design

Exp. No	Rolling Force (N)	Feed (mm/rev)	Spindle Speed (rpm)
1	143	0.04	400
2	143	0.08	400
3	143	0.12	400
4	143	0.04	600
5	143	0.08	600
6	143	0.12	600
7	143	0.04	800
8	143	0.08	800
9	143	0.12	800
10	330	0.04	400
11	330	0.08	400
12	330	0.12	400
13	330	0.04	600
14	330	0.08	600
15	330	0.12	600
16	330	0.04	800
17	330	0.08	800
18	330	0.12	800
19	495	0.04	400
20	495	0.08	400
21	495	0.12	400
22	495	0.04	600
23	495	0.08	600
24	495	0.12	600
25	495	0.04	800
26	495	0.08	800
27	495	0.12	800

In order to view the surface properties of deep rolled surfaces, surface images were taken with an optical microscope. In the optical photographs taken, horizontal lines represent the direction perpendicular to the workpiece axis. Optical photographs were taken from the vertices of cylindrical surfaces. SEM analyzes were carried out to examine the carbide, groove, scratch and microstructures of the deep rolled surfaces in more detail. For this purpose, images were taken using the SEM device.

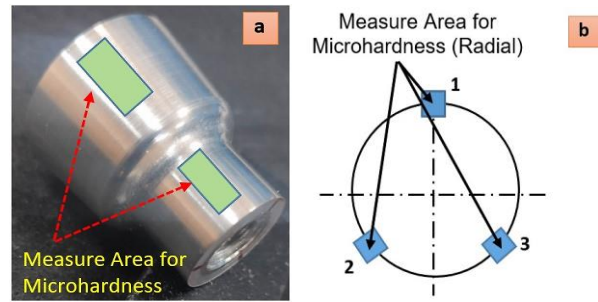


**Figure 4.** Measure of microhardness

### 3. Results and Discussion

According to the designed insert and the results of the previous study [34, 35] on the processing of Al6061-T6 material with this insert and Ra, it was found that the ideal parameter for Ra is 495 N in rolling force, 0.12 mm/rev in feed value and 600 rev in rotational speed. In addition, it was determined that the newly designed insert was suitable for using in deep rolling and could be used in conical, radius and longitudinal rolling operations at the same time. It was found that the most effective parameter on Ra was the feed value [34, 35]. Microhardness measurement values obtained from deep rolling test samples are given in Table 4.

**Table 4.** Values of microhardness

Exp. No	A	B	C	Microhardness (Hv <sub>0.3</sub> )
1	1	1	1	158
2	1	2	1	163.53
3	1	3	1	165.26
4	1	1	2	154.8
5	1	2	2	164.1
6	1	3	2	169.6
7	1	1	3	162.73
8	1	2	3	163.7
9	1	3	3	158.76
10	2	1	1	164.46
11	2	2	1	173.26
12	2	3	1	164.86
13	2	1	2	151.8
14	2	2	2	165.66
15	2	3	2	158.63
16	2	1	3	167.13
17	2	2	3	155.9
18	2	3	3	160.7
19	3	1	1	168.1
20	3	2	1	159.53
21	3	3	1	161.46
22	3	1	2	165.4
23	3	2	2	174.7
24	3	3	2	164.96
25	3	1	3	162.63
26	3	2	3	156.86
27	3	3	3	157.5

In Table 4, symbols A, B and C express rolling force (N), feed (mm/rev) and spindle speed (rpm), respectively. The numbers 1, 2 and 3 express the level of each parameter. Before the statistical analysis, it was analyzed whether the microhardness values obtained in Table 4 showed a normal distribution; hence, the graph in Figure 5 was obtained.

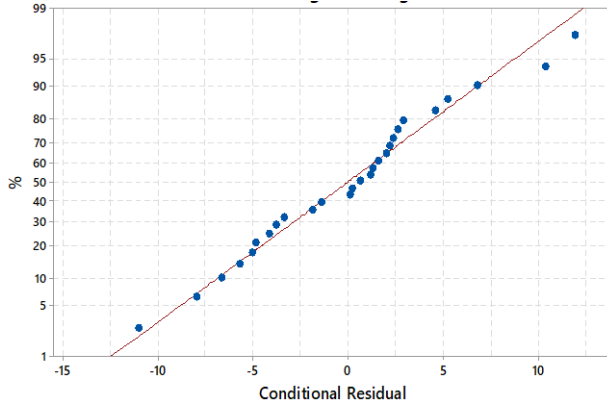


**Figure 5.** Probability of microhardness

The results obtained (Figure 5) show a normal distribution. It is known that surface hardness increases on surfaces subjected to rolling [33, 7]. In this study, the increase in microhardness values was measured before and after the rolling process in order to observe this effect of rolling. The graphical representation of the measurement results can be seen in the graph in Figure 6.

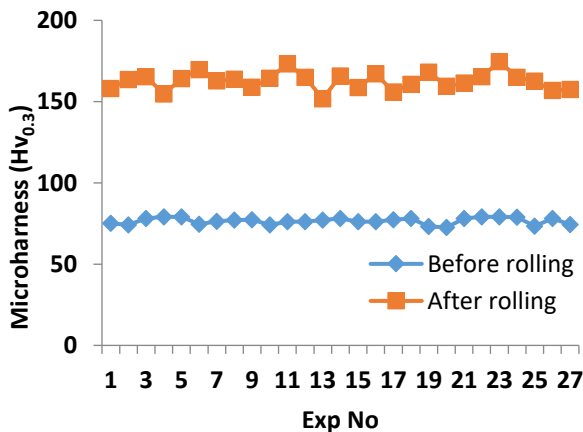


**Figure 6.** Microhardness graph before and after rolling

The microhardness values, which were in the range of 70-75  $Hv_{0.3}$  before rolling, increased by nearly 100% with the effect of rolling, thus hardness values in the range of 160-180  $Hv_{0.3}$  were obtained (Figure 6). From this, it can be concluded that rolling process increases the surface hardness under all conditions. Tayeb et al. stated that when the rolling polishing process was applied to Al6061 material, they found a microhardness of 78-92 HRB (150-200 Hv) depending on different process parameters [41]. Egea et al. found that the surface hardness of Al2050 material increased by 37.5% after rolling and

polishing, resulting in a micro hardness value of 140-160 Hv [42]. In his study, Koçak found a 10% hardness increase for Al6013 material and a 20% hardness increase for MS 58 material. The microhardness values found after the process are similar to the values in the literature [43, 18, 7]. Akkurt and Ovalı [18] obtained the hardness value in the range of 110-130  $Hv_{0.01}$  in deep rolling of Al6061 material. Additionally, Akyuz [7] obtained hardness values as 160-180  $Hv_{0.02}$  in deep rolling of AA7075-T6 material. Axir et al. [33] obtained hardness values in the range of 180-230 Hv for Al alloy 2014 material. The alloying of Al material with different metals is a phenomenon that also increases the hardness value [33]. Signal noise analysis was performed to see at what level the process parameters affected the micro hardness values obtained. In calculating the signal-to-noise (S/N) ratio, the "greatest is best" principle was taken as reference. The graph obtained from this analysis is seen in Figure 7.

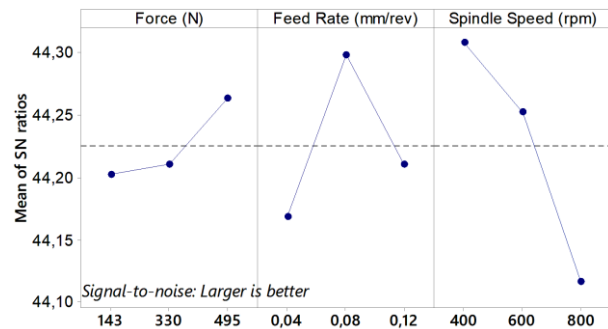


**Figure 7.** Plot of signal to noise ratios

The graph affecting microhardness is shown in Figure 7. As Figure 7, the most ideal parameter values on Ra are 495 N in rolling force, 0.08 mm/rev in feed, and 400 rpm in number of revolutions. In the experiments where the rolling pressure was 495 N, it was observed that hardness increased above the occurred average values, but hardness values below the average occurred at 143 N and 330 N. In terms of feed, it can be said that the values of 0.04 mm/rev and 0.12 mm/rev did not constitute the desired value in terms of hardness and that the value of 0.08 mm/rev was the optimum level for hardness. It is seen that there is an inverse proportion between the spindle speeds and the hardness. Here, it was concluded that there was an increase in hardness due to friction-related temperature and this value was obtained at 400 rpm. In order to see the change between processing parameters and microhardness, the evaluations were made; hence, the graphs in Figure 8 were obtained.

When previous studies on deep rolling are examined, it is seen that a definitive relationship between microhardness and process parameters cannot be obtained in most studies. This result is mostly similar for Figure 8 as well. When all parameters and parameter levels and both Ra and microhardness results are evaluated together, it is seen that the most important problem in the studies in the

literature, the inability to reach definite conclusions, has emerged the same as in our study. Although general conclusions have been obtained, further studies on ball and deep rolling are required to form conclusions with accuracy similar to those in surface smoothing operations such as machining or grinding.

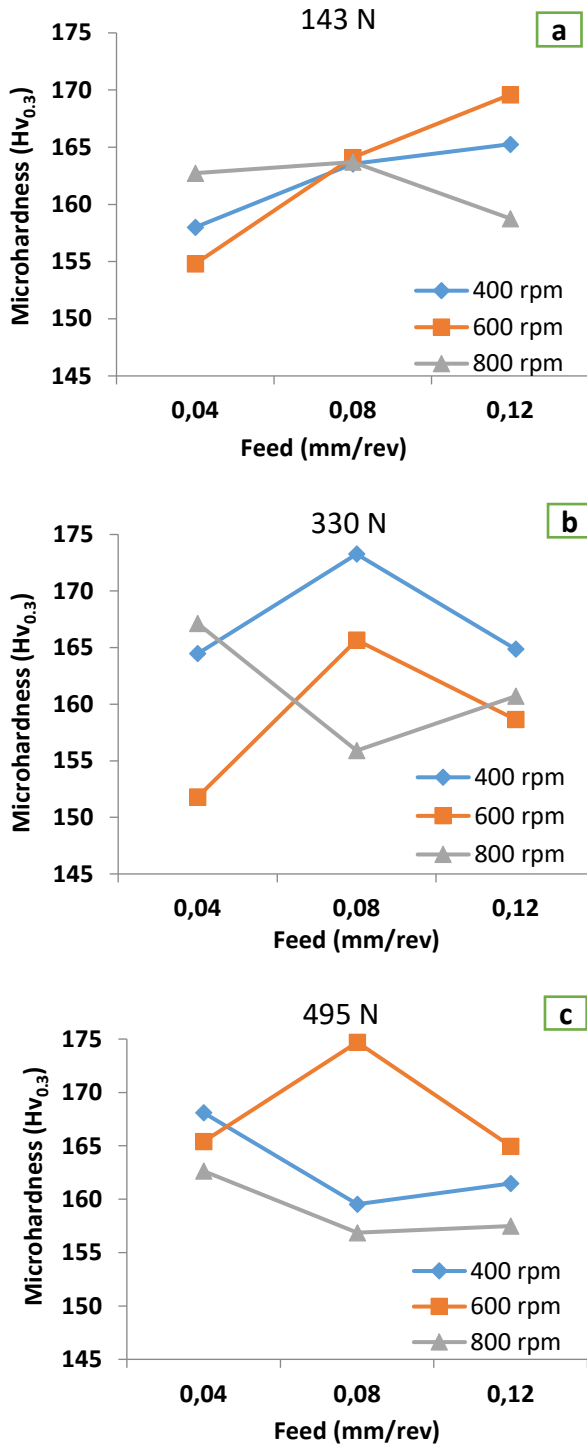


**Figure 8.** Relationship graph between machining parameters and microhardness

Axir et al. [33] observed that with the increase in feed and number of passes, microhardness increases up to certain values (for feed: 0.015 to 0.035 mm/rev and for the number of passes: 1 to 3) and then decreases.

Similarly, Basak et al. [27] obtained hardness values between 150-190 Hv at different rolling forces (100 N to 400 N) in the rolling of Al-Mg alloy. They observed that the increase in rolling force and feed caused an increase in hardness.

### 3.1 Optical Microscope Images

In order to examine the surface properties after deep rolling, both optical microscope images and SEM images were taken. In optical photographs, the horizontal lines represent the direction perpendicular to the workpiece axis. Optical photographs were taken from the top points of cylindrical surfaces. The surface image with finish turning operation before rolling is seen in Figure 9.

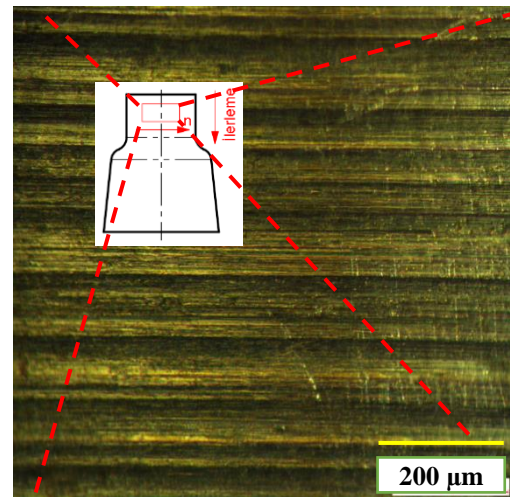


**Figure 9.** Surface optic view before deep rolling

When Figure 9 is examined, it can be seen that the normal appearance that is generally seen in the literature [44, 18, 45] as a result of the turning operation is also formed here. The images in Figure 10 were obtained from the images obtained after rolling.

The samples were taken at 200x magnification as shown in Figure 9 and Figure 10. In the images, it can be seen that the particles are generally distributed homogeneously. It is seen that Al6061 aluminum alloy has micro-pores of small sizes. When looking at the microscope images in Figure 10, it is seen that the bright surfaces are brighter because they are in the shape of cylindrical surfaces, while the dark areas are subject to erosion in the form of deep grooves. In deep rolling, debris and grooves may occur due to friction. Surface irregularities such as debris, grooves etc. have also been found by different researchers [46, 47]. Generally, the surface structure seen in Figure 10 in deep rolling is also

seen in previous studies [48, 49]. Additionally, when Figure 10 is examined, it is clearly seen that deformations occur on the surface as the feed rate increases. In the literature [3], it is stated that surface roughness increases as the pressure force increases in deep rolling.

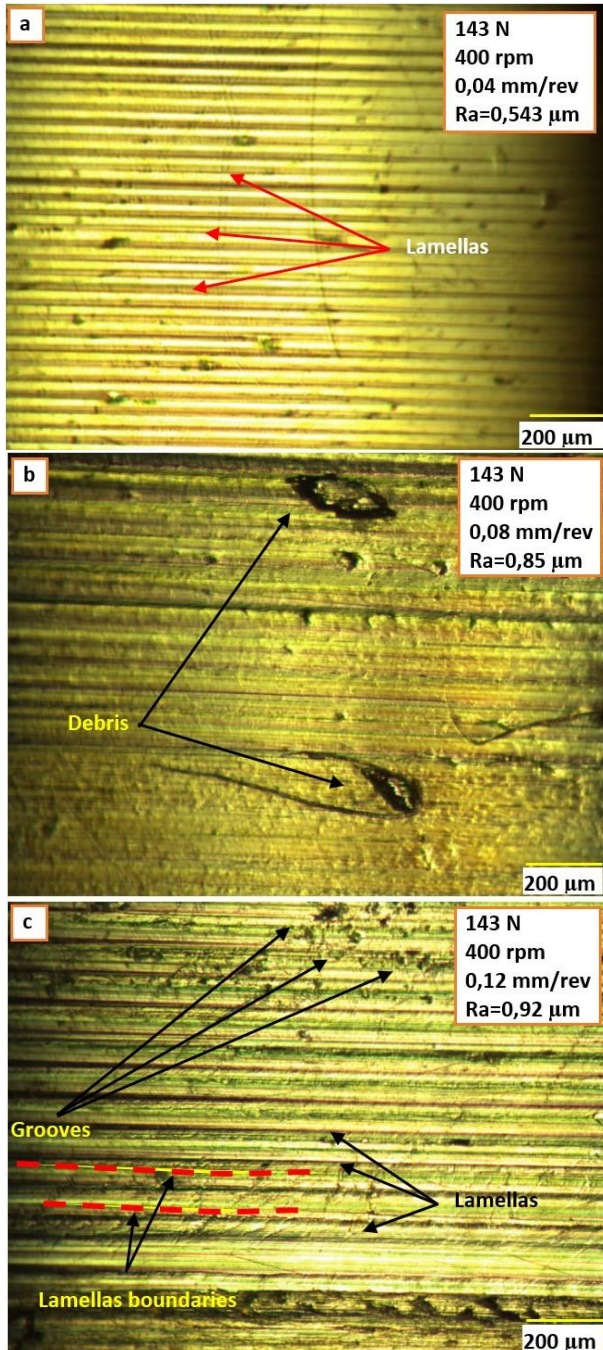


**Figure 10.** Optical photographs obtained at a rolling force of 143 N a)  $R_a=0,543$  b)  $R_a=0,85$  c)  $R_a=0,92$

### 3.2 SEM Images

SEM analyzes were performed to analyze the surfaces obtained after deep rolling and to evaluate the surface morphology. First of all, for comparison purposes, a

finish turning operation was applied before deep rolling, and then SEM images of the surface were taken (Figure 11), thus, it was aimed to examine and compare it after deep rolling.

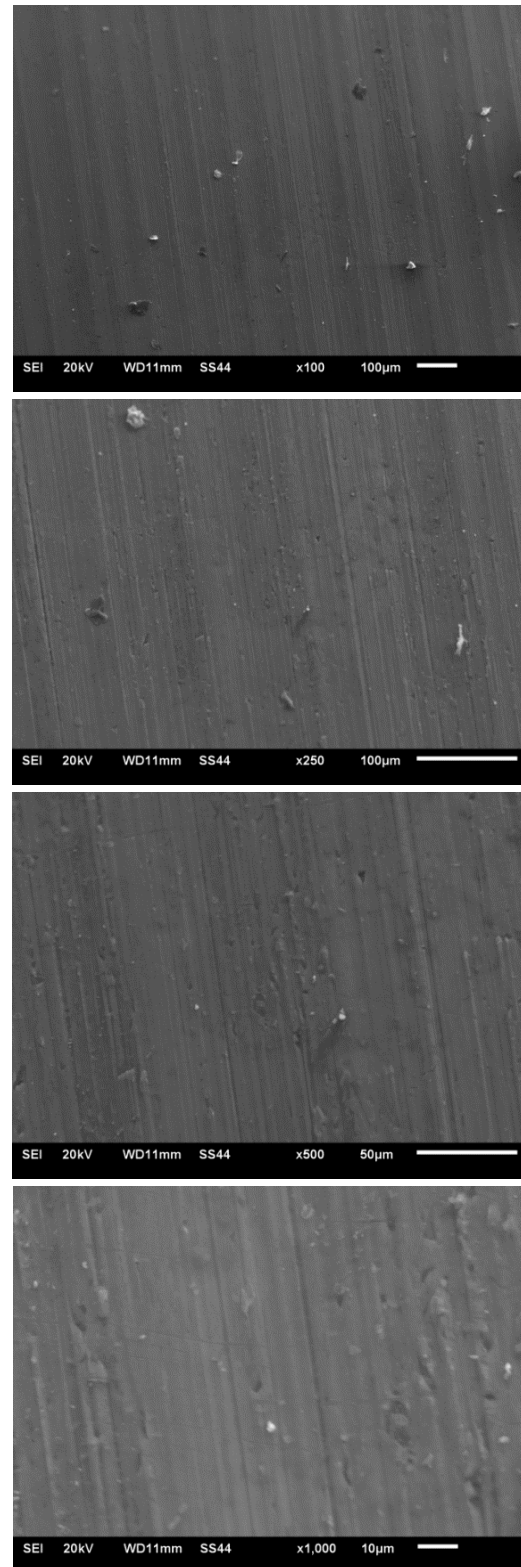


**Figure 11.** Images of deep-rolled finishing turning surfaces

In the deep rolling process, especially in the deep rolling of materials such as Al, it is seen that some particles (debris, BUE, etc.) are formed on the surface [46]. These debris can be seen in Figure 11. Here, the structures in Figure 12 were obtained in the SEM images taken to see the effect of the rolling force.

Depending on the increase in feed, it is seen that dents, scratches and residues on the surfaces increase (Figure 12).

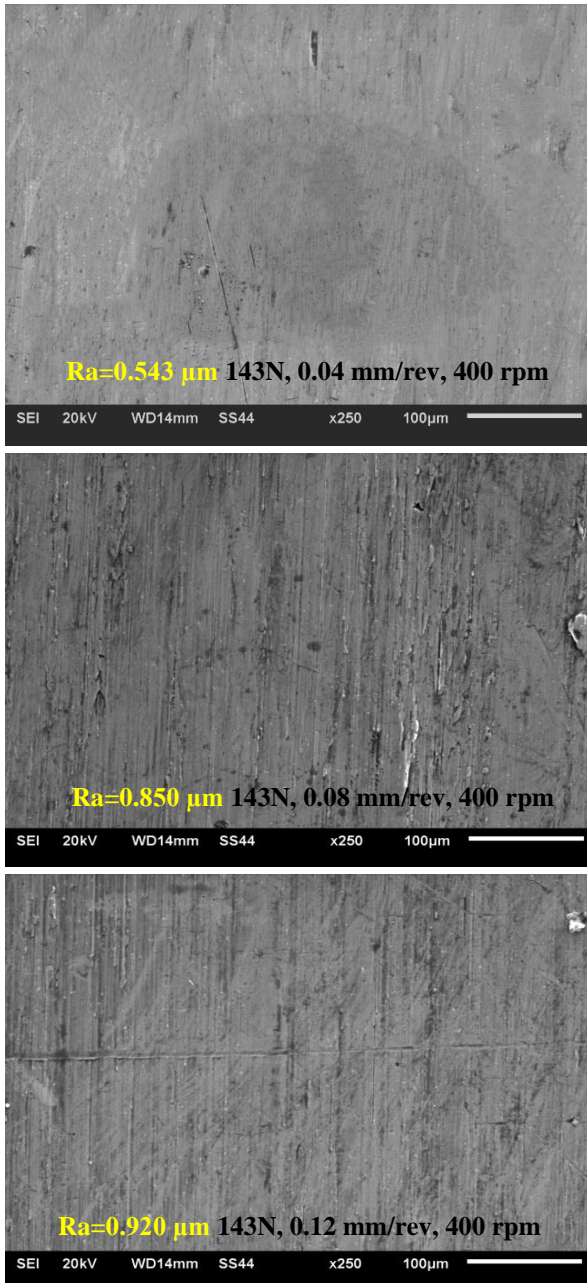


**Figure 12.** SEM images at a deep rolling force of 143 N

As a result of this situation, it is noted that there is an increase in Ra values. When the deep rolling mechanics are examined, it is seen that plastic deformation occurs

due to rolling. It is certain that this plastic deformation is shaped according to the process parameters, and deep rolling produces formations such as grooves and debris, and the surface topography arises depending on the effect of each parameter.

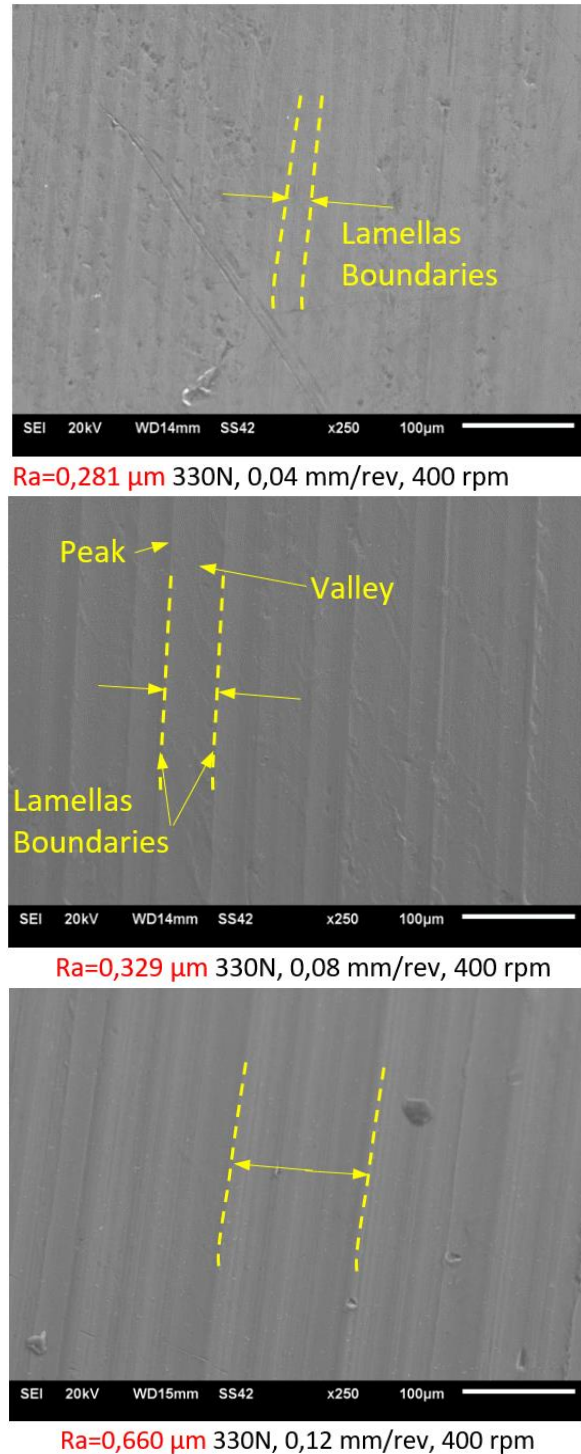


**Figure 13.** SEM images at 330 N rolling force

This is a type of process which is mechanically very complex, resulting from the type of material, friction behavior, heat, etc., and has not been proven by any

specific modeling yet. Although some results have been achieved in the studies, the subject has not yet been fully clarified. Therefore, much more work needs to be done. When the process was examined depending on the increase in rolling force, the structures in Figure 13 were obtained.

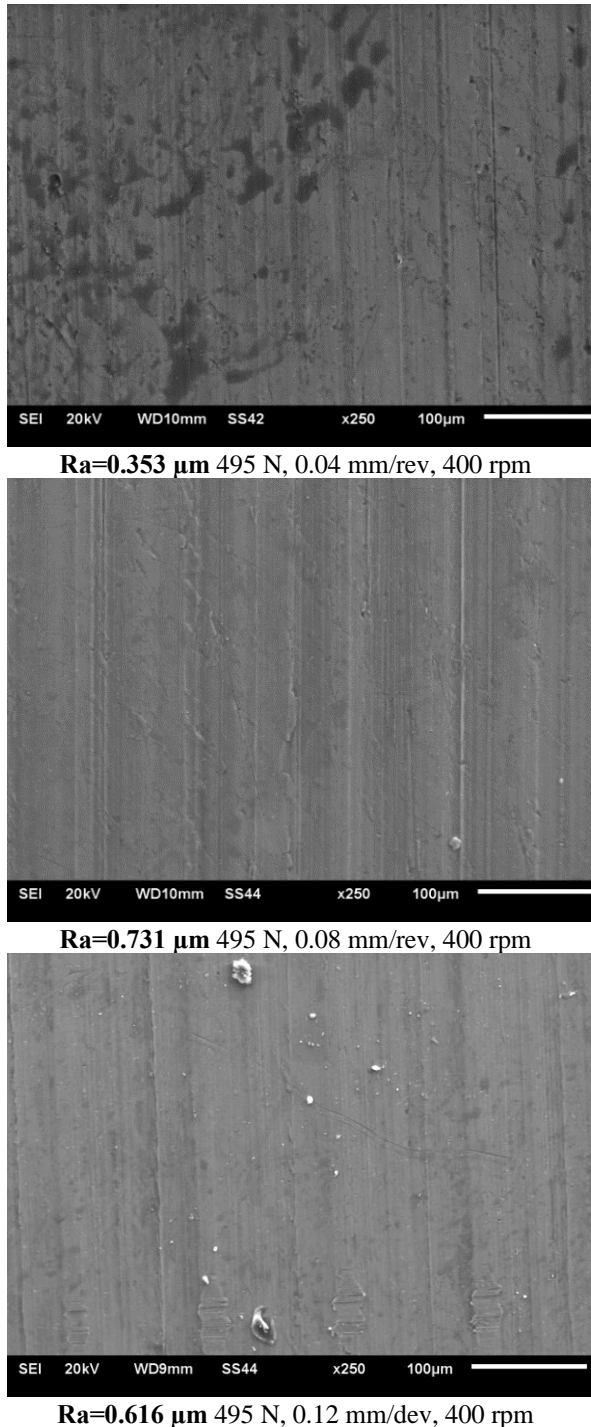


**Figure 14.** SEM images at a deep rolling force of 495 N

When both figure 12 and figure 13 are evaluated together, it can be seen that the surface topography has become more smooth, debris and grooves have decreased, and

accordingly, Ra values have decreased compared to 143 N rolling force. At 330 N rolling force, Ra values have increased depending on the increase in feed rate. In deep rolling, it is the pass in which the peaks remaining from the first finishing pass are filled into the valley parts with the first plastic deformation. The lower rolling force causes fewer peaks to be filled into valleys due to this pass. As the rolling force increases, the pressing force ensures that more material is filled into the valleys, resulting in the formation of a smoother surface. As a result, Ra values are further reduced. Due to the increase in feed, the increase in Ra also increases in parallel with that as in Figure 13. The most important issue that determines Ra values here is that the distance between the lamellar structure increases parallel to the feed rate, as seen in Figure 12, which is reflected in Ra values. SEM images with 495 N rolling force are given in Figure 14.

When the structures in Figure 12 and Figure 13 obtained with rolling forces of 143 N and 330 N are considered, it can be said that the rolling force of 330 N produces the best Ra values. Here, it was concluded that the increase in the rolling force causes excessive plastic deformation due to the increase in feed on the material surface, and the valleys on the surface are filled with more material than their volume causing deformations on the surface. At this point, Ra value, before deep rolling, appears as an important factor. Before the deep rolling process, it is necessary to determine Ra values and accordingly the peak and valley volumes and then determine the parameters of the deep rolling to be applied. In this regard, optimization studies are being carried out, and these should be done. There are studies showing the effectiveness of Ra values before deep rolling [32, 3].

#### 4. Conclusion

In this study, Al6061-T6 aluminum material was burnished by deep rolling method with a burnishing tip that can be used for conical, radius and cylindrical turning operations and can be fixed on the existing tool holder. The results obtained from the analyzes carried out to determine the relationship between microhardness, surface morphology and Ra in the deep rolling method of Al6061-T6 aluminum material can be summarized as follows:

- When the microhardness result was examined, it was revealed that the most ideal parameter on Ra was 495 N in rolling force, 0.08 mm/rev in feed and 400 rpm in speed.
- 200x optical microscope images of the workpieces were taken, thus it was seen that the images were distributed homogeneously.
- When SEM images are analyzed, it was observed that there was a decrease in Ra values due to the decrease in the distance between the lamellar structures with the increase in feed. This result is also compatible with the literature.

- Due to the increase in rolling pressure force and the increase in feed rate on the material surface, excessive plastic deformation occurred and the valleys on the surface were filled with more material than their volumes, causing deformations there. For this reason, the rolling force limit must be determined well.
- Due to the increase in feed, it was observed that debris, grooves and residues on the surfaces increased. Microhardness values were obtained at 140-160 HV<sub>0.03</sub> values and were observed to decrease with distance from the surface.
- It seems difficult to talk about a sufficient trend to reach a conclusion between microhardness and parameters, as in the literature. The issue should be studied and researched further.
- It was observed that there is an inverse proportion between the spindle speed and hardness.

It was concluded that it is an important problem that the optimum criteria for obtaining the desired surface properties have not yet been achieved in deep rolling and ball burnishing processes. Therefore, more research is needed to determine the correct process parameters for this issue.

#### Author's Contributions

**Oktay Adıyaman:** Conducted the experiment and result analysis, and then drafted and prepared the article.

**Feyza Aydın:** Assisted and supervised the study, as well as helped in manuscript preparation.

#### Ethics

There are no ethical issues after the publication of this manuscript.

#### Acknowledgement

In order to carry out the research, Batman University unit of BAP (Scientific Research Projects) provided financial support to this study numbered BTUBAP-2022-YL-05.

#### References

- [1]. Wandra, R., Prakash, C., Singh, S. 2022. Experimental investigation and optimization of surface roughness of  $\beta$ -Phase titanium alloy by ball burnishing assisted electrical discharge cladding for implant applications. *Materials Today: Proceedings*; 48, 975-980, doi: 10.1016/j.matpr.2021.06.070.
- [2]. Kinner-Becker, T., Zmich, R., Sölter, J., Meyer, D. 2021. Combined laser and deep rolling process as a means to study thermo-mechanical processes. *Procedia CIRP*; 102, 369-374, doi: 10.1016/j.procir.2021.09.063.
- [3]. Prabhu, P. R., Kulkarni, S. M., Sharma, S. S. 2011. An experimental investigation on the effect of deep cold rolling parameters on surface roughness and hardness of AISI 4140 steel. *World Academy of Science, Engineering and Technology*; 60, 1594-1598.

- [4]. Başak, H., Sönmez, F., 2015. In Burnishing Process, Inspection of The Burnishing Apparatus (Ball, Roller, Twist Roller) Effects on Surface Roughness and Surface Hardness, *Journal of Polytechnic*; 18(3), 125-132, doi: 10.2339/2015.18.3, 125-132.
- [5]. Mendi, F., Takım tezgâhları teori ve hesapları, ISBN:975-06008-0-3, Ankara, 1996.
- [6]. Özkan, S. 2006. Sürtünme karıştırma kaynağı ile birleştirilen parçalarda haddeleme (burnishing) ile yüzeylerin işlenmesi, haddelemenin yüzey pürüzlülüğüne ve sertleşmeye etkisinin incelenmesi. *M.S. thesis, Gazi Üniversitesi Fen Bilimleri Enstitüsü*, Ankara.
- [7]. Akyüz, M. 2020. Bilyeli haddeleme yönteminde işlem parametrelerinin Al7075-T6 alüminyum alaşımının mekanik özellikleri üzerindeki etkilerinin deneysel olarak araştırılması. *M.S. thesis, Fen Bilimleri Enstitüsü Fırat Üniversitesi*, Elazığ.
- [8]. Hassan A. D., Maqableh A. M., 2000. The effects of initial burnishing parameters on non-ferrous components. *Journal of Materials Processing Technology*; 102(1-3), 115-121, doi: 10.1016/S0924-0136(00)00464-7.
- [9]. Luo H., Wang L., Zhang C. 2011. Study on the aluminum alloy burnishing processing and the existence of the outstripping phenomenon. *Journal of Materials Processing Technology*; 116, 88-90, doi: 10.1016/S0924-0136(01)00847-0.
- [10]. Hassan, A. M. 1997. The effects of ball-and roller-burnishing on the surface roughness and hardness of some non-ferrous metals. *Journal of materials processing technology*; 72(3), 385-391, doi: 10.1016/S0924-0136(97)00199-4.
- [11]. Yu X., Wang L. 1999. Effect of various parameters on the surface roughness of an aluminium alloy burnished with a spherical surfaced polycrystalline diamond tool. *International Journal of Machine Tools & Manufacture*; 39(3), 459-469, doi: 10.1016/S0890-6955(98)00033-9.
- [12]. El-Axir, M.H., El-Khabeery, M.M. 2003. Influence of orthogonal burnishing parameters on surface characteristics for various materials. *Journal of Materials Processing Technology*; 132, 82-89, doi: 10.1016/S0924-0136(02)00269-8.
- [13]. Zhuang, W., Liu, Q., Djugum, R., Sharp, P.K., Paradowska, A. 2014. Deep surface rolling for fatigue life enhancement of laser clad aircraft aluminium alloy. *Applied Surface Science*; 320, 558-562, doi: 10.1016/j.apsusc.2014.09.139.
- [14]. Majzoobi, G.H., Jouneghani, F.Z., Khademi, E. 2016. Experimental and numerical studies on the effect of deep rolling on bending fretting fatigue resistance of Al7075. *Int. J. Adv. Manuf. Technol*; 82, 2137-2148, doi: 10.1007/s00170-015-7542-z.
- [15]. Khabeery M. M., Axir M. H., 2001. Experimental techniques for studying the effects of milling roller-burnishing parameters on surface integrity. *International Journal of Machine Tools & Manufacture*; 41(12), 1705-1719, doi: 10.1016/S0890-6955(01)00036-0.
- [16]. Basak H., Goktas H.H. 2009. Burnishing process on al-alloy and optimization of surface roughness and surface hardness by fuzzy logic. *Materials and Design*; 30, 1275-1281, doi: 10.1016/j.matdes.2008.06.063.
- [17]. Tadic B., Todorovic M. P., Luzanin O., Miljanic D., Jeremic M. B., Bogdanovic B., Vukelic D. 2013. Using specially designed high-stiffness burnishing tool to achieve high-quality surface finish. *The International Journal of Advanced Manufacturing Technology*; 67, 601-611, doi: 10.1007/s00170-012-4508-2.
- [18]. Akkurt, A., Ovalı, İ. 2009. The effects of burnishing and conventional finishing processes on surface roughness and roundness

of the Al 6061 aluminum parts. *Pamukkale Üniversitesi Mühendislik Bilimleri Dergisi*; 15(3), 371-382.

- [19]. Akkurt, A. Delik yüzeylerine uygulanan yüzey iyileştirme işlemlerinin alüminyum alaşımı malzemeler üzerinde araştırılması, 5. Uluslararası İleri Teknolojiler Sempozyumu (IATS'09), Karabük, Turkey, 2009.
- [20]. Başak, H. 2015. Haddeleme (Galetaj) ile 5083 Al-Mg malzeme yüzeyinin işlenmesi, haddeleme parametrelerinin yüzey pürüzlülüğü ve yüzey sertliğine etkilerinin incelenmesi. *GU J Sci Part:C*; 3(2), 471-476.
- [21]. Malyer, E. 2018. Examining the residual stress on the burnished AA7075-T6 aluminum alloy. *Journal of Polytechnic*; 21(3), 565-573, doi: 10.2339/politeknik.389592.
- [22]. Maiß, O., Röttger, K. 2022. Monitoring the surface quality for various deep rolling processes—limits and experimental results. *Procedia CIRP*; 108, 857-862, doi: 10.1016/j.procir.2022.05.199.
- [23]. Oevermann, T., Wegener, T., Liehr, A., Hübner, L., Niendorf, T. 2021. Evolution of residual stress, microstructure and cyclic performance of the equiatomic high-entropy alloy CoCrFeMnNi after deep Rolling. *International Journal of Fatigue*; 153, 106513.
- [24]. Martins, A. M. Leal, C. A. Campidelli, A. F. Abrao, A. M.; Rodrigues, P. C. Magalhães, F. C. Meyer, K. 2022. Assessment of the temperature distribution in deep rolling of hardened AISI 4140 steel. *Journal of Manufacturing Processes*; 73, 686-694, doi: 10.1016/j.jmapro.2021.11.052.
- [25]. Bogachev, I., Knowles, K. M., Gibson, G. J. 2021. Deep cold rolling of single crystal nickel-based superalloy CMSX-4. *Materialia*; 20, 101240, 2021.
- [26]. Hettig, M., Meyer, D. 2020. Sequential multistage deep rolling under varied contact conditions. *Procedia CIRP*; 87, 291-296, doi: 10.1016/j.procir.2020. 02.027.
- [27]. Basak, H., Ozkan, M., Toktas, I. 2019. Experimental research and ANN modeling on the impact of the ball burnishing process on the mechanical properties of 5083 Al-Mg material. *Kovové materiály-Metallic Materials*; 57(1), 61-74, doi: 10.4149/km 2019\_1\_61.
- [28]. Delgado, P., Cuesta, I. I., Alegre, J. M., Díaz, A. 2016. State of the art of Deep Rolling. *Precision Engineering*; 46, 1-10, doi: 10.1016/j.precisioneng.2016. 05.001.
- [29]. Sönmez, F., Başak, H., Baday, Ş. 2016. Haddeleme işleminin yüzey yanıt yöntemi ile analizi. *Gazi University Journal of Science Part C: Design and Technology*, 4(4), 275-283.
- [30]. Adıyaman, O. 2024. Investigation on the Application of Worn Cutting Tool Inserts as Burnishing Tools. *Strojniški vestnik - Journal of Mechanical Engineering*, 70(1-2), 92-102. doi:http://dx.doi.org/10.5545/sv-jme.2023.781
- [31]. Blasón, S., Rodríguez, C., Belzunce, J., Suárez, C. 2017. Fatigue behaviour improvement on notched specimens of two different steels through deep rolling, a surface cold treatment. *Theoretical and Applied Fracture Mechanics*; 92, 223-228, doi: 10.1016/j.tafmec.2017.08.003.
- [32]. Prabhu, P. R., Kulkarni, S. M., Sharma, S. 2020. Multi-response optimization of the turn-assisted deep cold rolling process parameters for enhanced surface characteristics and residual stress of AISI 4140 steel shafts”, *Journal of Materials Research and Technology*; 9(5), 11402-11423, doi: 10.1016/j.jmrt.2020.08.025
- [33]. El-Axir, M. H., Othman, O. M., & Abodiena, A. M. 2008. Improvements in out-of-roundness and microhardness of inner surfaces by internal ball burnishing process. *Journal of materials processing technology*, 196(1-3), 120-128. doi: 0.1016/j.jmatprotec.2007.05.028
- [34]. Aydın, F., Adıyaman, O. 2023. Experimental investigation of new type insert in deep rolling of al6061-t6 material. *Rahva Journal of Technical and Social Studies*; 3(1), 58-72.
- [35]. Aydın, F., Adıyaman, O. 2023. Yeni tip insert uç ile Al6061 malzemeye bilyeli parlatma yöntemi uygulanması ve yüzey özelliklerinin incelenmesi. 2nd International Rahva Technical and Social Researches Congress, Bitlis, Turkey, 171-172.
- [36]. Yüce Teknik, 2023, <https://www.yuceteknik.com/> Mekanik-Kalip-Yaylari-Yesil-Yay.PR-1779.html (accessed: 20/08/2023).
- [37]. Technical Data Sheet, 2024, [https://www.skf.com/binaries/pub12/Images/LubriFluid\\_TD\\_US\\_tcm\\_12-158093.pdf](https://www.skf.com/binaries/pub12/Images/LubriFluid_TD_US_tcm_12-158093.pdf), (accessed :06/03/2024)
- [38]. Lee SH. 2003. Optimization of cutting parameters for burr minimization in face-milling operations. *Int J Prod Res* 41 (3):497 doi:10.1080/0020754021000042382.
- [39]. Lin TR (2002) Optimization technique for face milling stainless steel with multiple performance characteristics. *Int J Adv Manuf Technol* 19:330 doi:10.1007/s001700200021
- [40]. Ross PJ (1996) Taguchi techniques for quality engineering, 2<sup>nd</sup> edn. McGraw-Hill, New York
- [41]. El-Tayeb, N. S. M., Low K. O., Brevern P. V. 2007. Influence of roller burnishing contact width and burnishing orientation on surface quality and tribological behaviour of Aluminium 6061. *Journal of materials processing technology*; 186(3), 272-278, doi: 10.1016/j.jmatprotec.2006.12.044.
- [42]. Egea A.J.S., Rodríguez A., Celentano D., A.Calleja, Lacalle L.N. 2019. Joining metrics enhancement when combining FSW and ball-burnishing in a 2050 aluminium alloy. *Surface & Coatings Technology*; 367, 327–335, doi: 10.1016/j.surfcoat.2019. 04.010.
- [43]. Koçak, H. 2020. Improving the surface properties of Al 6013 and MS 58 materials by ball burnishing process for hole. *GU J Sci, Part C*; 8(4), 972-980, doi: 10.29109/gujsc.821576.
- [44]. Martins, A. M., Oliveira, D. A. D., de Castro Magalhães, F., & Abrão, A. M. (2023). Relationship between surface characteristics and the fatigue life of deep rolled AISI 4140 steel. *The International Journal of Advanced Manufacturing Technology*, 129(3), 1127-1143. doi: 10.1007/s00170-023-12332-x.
- [45]. Shetty, R., Rao, S. S., & Gaitonde, V. N. 2017. Wear resistance enhancement of titanium alloy (Ti-6Al-4V) by ball burnishing process. *Journal of Materials Research and Technology*, 6(1), 13-32. doi: 10.1016/j.jmrt.2016.03.007.
- [46]. Wang, Z., Xiao, Z., Huang, C., Wen, L., & Zhang, W. 2017. Influence of ultrasonic surface rolling on microstructure and wear behavior of selective laser melted Ti-6Al-4V alloy. *Materials*, 10(10), 1203, doi: 10.3390/ma10101203.
- [47]. Attabi, S., Himour, A., Laouar, L., & Motalebzadeh, A. 2021. Mechanical and wear behaviors of 316L stainless steel after ball burnishing treatment. *Journal of Materials Research and Technology*, 15, 3255-3267. doi: 10.1016/j.jmrt.2021.09.081.
- [48]. Herbster, M., Harnisch, K., Haberland, E., Kriegel, P., Döbberthin, C., Heyn, A., Halle, T. 2021. Effect of deep rolling on subsurface conditions of CoCr28Mo6 wrought alloy to improve the wear resistance of endoprostheses. *Journal of the Mechanical Behavior of Biomedical Materials*; 118, 104398, doi: 10.1016/j.jmbbm.2021.104398.



- [49]. Chen, M., He, J., Wang, M., Li, J., Xing, S., Gui, K., Liu, Q. 2022. Effects of deep cold rolling on the evolution of microstructure, microtexture, and mechanical properties of 2507 duplex stainless steel. *Materials Science and Engineering: A*; 845, 143224. doi: 10.1016/j.msea.2022.143224.

## Investigation of Earthquakes in Turkey with Cluster Analysis\*

Ahmet Murat ŞEN<sup>1\*\*</sup> , Zeki YILDIZ<sup>2</sup> 

\*This study is generated from the thesis titled “Investigation of Markovian Structure According to the Magnitudes of Earthquakes in Turkey by Cluster Analysis”, which is being written in the Department of Statistics, Institute of Science and Technology, Eskişehir Osmangazi University, Eskişehir, Turkey.

<sup>1</sup>Department of Statistics, Institute of Science, Eskişehir Osmangazi University, Eskişehir, Turkey

<sup>2</sup>Department of Statistics, Faculty of Science, Eskişehir Osmangazi University, Eskişehir, Turkey

\*\*[501420220002@ogu.edu.tr](mailto:501420220002@ogu.edu.tr)

\*\* Orcid No: 0000-0003-4359-5000

Received: 8 January 2024

Accepted: 24 March 2024

DOI: 10.18466/cbayarfbe.1416472

### Abstract

In this study, earthquakes with a magnitude of 3 and above occurring between 36-42 degrees North latitude and 26-45 degrees East longitude, within and around Turkey from 1980 to 2022, were considered. Turkey and its immediate surroundings were divided into 114-unit squares using latitude and longitude coordinates to investigate seismic similarities. The variables including 50130 earthquake depths and magnitudes in our data set were analyzed using the {K-Means Cluster Analysis} method in the SPSS program. Hierarchical clustering method was used to determine the number of clusters and the number of clusters was determined as 5 with the help of the dendrogram obtained. As a result of the cluster analysis, it was observed that 47% of the earthquakes in Turkey were at a depth of 5 to 10 km. It has been observed that 93% of the earthquake intensities occur between 3 and 4 magnitudes. A cluster analysis was conducted to assess the similarities and dissimilarities among earthquakes within these unit squares in terms of their magnitudes and depths. Due to the large sample size and the analysis involving continuous variables, the earthquake data were grouped into 5 clusters using non-hierarchical clustering methods, and the relationships within and between these clusters were observed.

**Keywords:** Cluster Analysis, Earthquake, Depth, Magnitude.

### 1. Introduction

The two severe earthquakes that occurred in our country on February 6, 2023, followed by the earthquake storm that emerged afterwards, as well as the ongoing earthquakes, have been among the biggest disasters our country has faced. These tragic events have deeply saddened us as a whole country and other countries also shared the same pain. It is not possible to predict the earthquake in terms of time and date. However, in terms of probability, we can scientifically predict in what intensity range and in how many years [1-2-3]. When looking at recent studies that have conducted cluster analysis on earthquake-prone area data; earthquakes occurring near the city of Bengkulu in Indonesia were analyzed using the k-means technique for cluster analysis [15]. Similarly, seismic earthquakes in India were analyzed using the k-means technique for cluster analysis [16]. Earthquakes on the Zagros mountains within the borders of Iran were also examined using the k-means technique, as in previous studies. Based on these studies;

earthquakes in Turkey have been grouped using the k-means technique for cluster analysis based on their depth and magnitude, yielding scientific results. Although Turkey is located in the Alpine-Himalayan fold belt, a large part of it is located in the earthquake zone and is constantly compressed by the Eurasian plate in the north and the African plate in the south due to the inability of Anatolia to complete its evolution.

Due to this compression, the fault lines formed in Anatolia are located in certain sections and these are called the North Anatolian Fault, the South Anatolian Fault, the Aegean Graben System and the Southeastern Anatolian Thrust Belt. Our country is located between (36°-42°) northern latitudes and (26°-45°) eastern longitudes. It includes 19 longitudes and 6 latitudes. As can be seen in Figure 1, 114 regions are visualized on the map of Turkey by dividing them into latitude and longitude squares.

We refer to each of these allocated sections as a unit

square. Earthquake data can be examined through these unit squares and the relationships between these earthquakes can be evaluated.

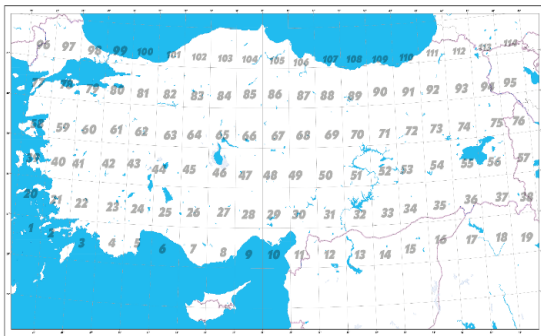


**Figure 1.** Dividing the latitude and longitude coordinates of the Turkey map into unit squares.

## 2. Materials and Methods

### 2.1. Cluster Analysis

If we define cluster analysis, it is a method of dividing the stack of variables into certain groups in terms of their similarities within themselves. It is also a way to find general patterns of distribution in data. It is widely used in statistical analysis [4].

Cluster analysis provides the emergence of certain important features in data analysis. It has the ability to work with unorganized data sets whose dependent variable is uncertain or neglected during the data analysis phase. To measure the distances between units, measurement techniques such as Euclidean distance, Minkowski distance, Manhattan distance, and Jaccard coefficient are used. The main purpose of using these techniques is to ensure the formation of clusters where units exhibit homogeneous properties within themselves. In more general terms, these measurement techniques aim to minimize distances within clusters and maximize distances between clusters [5].

Assumptions that are vital for other statistical methods such as normality, linearity, and constant variance do not have much importance in Cluster Analysis. For this reason, in Cluster Analysis applications, it is recommended to take into account the ability of the data to represent the sample in question and whether it has multiple linked variables. The most important issue to be decided at the stage of choosing clustering analysis will be the degree to which the sample to be examined represents the subgroups in the stack [6].

Cluster analysis is one of the most used techniques as a result of the advancement of technology and is widely used in data mining, especially for large data sets. The

cluster analysis method, which was mostly performed manually in the past, can now be applied to large datasets with the assistance of computer technologies, in parallel with technological advancements. Today, it is widely used primarily in market research, customer portfolios of companies, medicine, etc. [7]. Basically, cluster analysis is an analysis technique that aims to collect data with different characteristics in the same group by making use of certain similarities. There are many algorithms available in cluster analysis. In general, these algorithms are grouped into two groups: hierarchical clustering techniques that create dendrograms and non-hierarchical clustering techniques. The main goal of both of these techniques is to maximize the differences between clusters and intra-cluster similarities. In other words, it is to maximize the similarity situation within the sets and to minimize the similarity between the sets. Which of these techniques is preferred depends on the number of clusters, but it is much more useful to use both techniques together? Thus, it helps us to compare the results of both techniques used and to choose the most appropriate technique to be used [8]. Hierarchical clustering method is used in data sets where the number of clusters is not specified. The number of clusters is determined based on the chosen hierarchical clustering technique. In cases where the number of clusters is known, the K-Average technique, which is one of the non-hierarchical clustering methods, is used. These groupings are made according to the specified number of clusters. When determining the clustering analysis technique, the nature of the data set is generally taken into consideration. In this case, some data are collected by determining the first data, while some data are divided from the total and clustered. Figure 1 illustrates the separation of latitude and longitude of the map of Turkey into unit squares.

#### 2.1.1. Hierarchical Clustering Techniques

Hierarchical techniques start with a matrix of distances between units. At the beginning of the analysis phase, each unit is considered as a single set. Afterwards, the groups that are closest to each other are combined with each other and this merging process is repeated one after the other [8]. Among the hierarchical techniques, the most accepted ones are [12];

- Single Linkage Technique (Nearest Neighborhood)
- Complete Linkage Technique (Farthest Neighborhood)
- Average Group Linkage Technique
- Ward Technique
- Median Technique
- Centroid Technique.

##### 2.1.1.1. Single Linkage Technique

In single linkage technique, the existing distance between

two clusters begins with the minimum distance between the clusters [9].

#### 2.1.1.2. Complete Linkage Technique

In other words, the "Farthest Neighborhood" technique is similar in theory to the single linkage technique. The difference between this technique and the single linkage technique is that it makes use of the maximum distance between two units, instead of the minimum distance between clusters [9].

#### 2.1.1.3. Average Group Linkage Technique

In the Average Group Linkage Technique, the distance between the two groups must be short in order to unite. In other words, the calculation of the difference between two sets is done by taking the average differences between the pairs of units in one set and the pairs of units in another set [9].

#### 2.1.1.4. Ward Technique

It is a general hierarchical clustering technique created by Ward in 1963 to assist with partial problems. It is also called the minimum variance method. The technique aims to combine two sets with a minimum sum of squares within sets (minimum variance within the group) [13].

#### 2.1.1.5. Median Technique

It was developed by Gower in 1967 to determine the calculation point of cluster distances as the midpoint. Thus, for  $n$  clusters, each of which contains a single unit at the beginning, the distance between each cluster will be equal and equal to its median value [13].

#### 2.1.1.6. Centroid Technique

In the centroid technique, the distance between clusters is expressed as the Euclidean distance between cluster averages. Thus, the weighted average of the cluster means is considered to be the cluster center [12].

### 2.1.2 Non-Hierarchical Clustering Techniques

If the researcher has a preliminary knowledge about the number of clusters, in other words, if the number of clusters is decided by the researcher, non-hierarchical techniques are used instead of hierarchical techniques [8]. Non-hierarchical clustering techniques have the advantage of being faster than hierarchical clustering techniques. In addition, the higher the sample size, the more meaningful the results will be. In many non-hierarchical clustering techniques, the number of clusters is predetermined by the researcher as 'k' according to the sample size. In general, it is recommended to use hierarchical techniques and non-hierarchical techniques together [8]. The k-mean technique, which is a

hierarchical clustering technique, was developed by J.A. Hartigan and M.A. Wong, and the purpose of this technique is to create a small number of clusters among a large number of units. Although this technique is used both for units that contain discrete variables, it can also be applied to continuous variables that do not contain extreme values. The primary objective in using this technique is to minimize the sum of squares within clusters, thereby minimizing cluster variability and dividing a  $p$ -dimensional unit into 'k' clusters. [14].

### 3. Cluster Analysis in Earthquake Studies

In the study conducted by [15], earthquakes occurring near the city of Bengkulu in Indonesia were grouped according to seismic classifications, based on location and magnitudes, using cluster analysis to categorize earthquake characteristics. While performing the cluster analysis of the earthquake source regions, weightings were made with the k-means technique. In this study, 19 optimal earthquake clusters were obtained. The data consists of earthquakes of magnitude 5 Ms (surface wave) and above, which occurred from January 1970 to December 2015 in and around Bengkulu, West Sumatra, Lampung, and the Indian Ocean regions. As a result, earthquakes in and around the city of Bengkulu mostly occur in the Indian Ocean, with only minor earthquakes occurring on the mainland. Most earthquakes with a magnitude of 5 ms to 6 ms are tectonic earthquakes that occur at a depth of less than 100 km. Among the earthquake clusters created, the most striking is the earthquake that occurred around the Mentawai Islands of West Sumatra province, and another in the seas of Lampung Province.

In the study conducted by [16], cluster analysis was performed using the k-means method based on the spatial and positional magnitudes of seismic earthquakes that occurred in India over the last 10 years. The performance of the study is calculated using the sum of the squares of the intra-cluster error coefficients. In the current study, 6 earthquake clusters were obtained. The applied dataset consists of 1657 seismic events that occurred in India between January 1, 2005 and December 31, 2015. Each seismic event includes the year, month, day, hour, latitude, longitude, and magnitude. The focus of the study has been on the magnitude of the earthquake rather than its time. As a result, other variables have been excluded from the research, and only earthquake magnitudes have been included in the cluster analysis. Euclidean distances were used to calculate the distance between the two clusters. As a result, the k-means method has a strong potential to provide a superior tool in earthquake cluster analysis. In the study conducted by [17], earthquakes occurring on the Zagros Mountains within the borders of Iran were investigated and categorized into seismic zones based on their respective faults. The k-means technique was used for clustering these regions, with the dataset

containing 554 earthquakes of magnitude 4 and above that occurred between 2006 and 2019. By including outlier values, a total of 13 clusters have emerged, and it is observed that the clusters are more homogeneous as a result of the weighting process performed using the k-means technique. Examples of widespread studies of cluster analyses in the field of earthquakes are [15-16-17-18-19-20-22]. In the data sets consisting of earthquake data, aftershocks and precursor shocks were determined as dependent variables, and these variables formed distributions according to probability laws and parameters. These distributions are estimated by statistical methods [21].

Since non-hierarchical clustering methods generally contain large data sets and the earthquake data in question consists of continuous variables, it would be more appropriate to group them with the non-hierarchical clustering method in accordance with the data set we have. Although it is expected for us that the intra-group homogeneity is maximum and the similarity between the groups is minimum in order to create ideal clusters, it is aimed to create optimal groups by using the K-Mean technique for the number of clusters determined by us and then to examine the heterogeneity of the said groups with the Euclidean Distance. In the stages of cluster analysis, while determining certain objectives and after the selection of variables, the specific questions that the researcher should answer are as follows [24];

- Is the sample size large enough?
- Are there outliers in the data and can these outliers be removed from the research?
- How can the similarities between observations be determined?
- Is there a need for standardization of the data?

Many different approaches can be used to answer the above questions. But none of these questions is sufficient to be a definitive answer. For this reason, each different approach will produce different results for the same data. For this reason, just like factor analysis, cluster analysis will be more affected by the design of the research and the method selection process compared to other multivariate methods [25]. The main purpose of cluster analysis is the similarity and distances between units. For this reason, the first step of the analysis in question is the creation of a similarity or distance matrix. However, one of the most important decision points is whether standardization of the data is necessary before calculating similarity measurements. The reason for this is that these measurements are sensitive to size differences between different scales and variables [25]. Various units of distance measurement are proposed to calculate the distances of units to variables and between each other. The measurement units in question also vary according to the measurement units of the variables present in the

data matrix. If the variables are obtained by proportional or intermittent scales, distances or relationship type measures are used. If the measurements are made according to binary observations, the existing similarity and difference measurements between the units are beneficial. [11]. In order to obtain reliable results in cluster analysis, the number of clusters must be accurately determined after the variables are included in the model. The researcher's initiative is important in deciding the number of clusters, but certain methods have been developed to minimize bias. The most practical formula for determining the number of clusters is as follows [8-10].

$$k = \left(\frac{n}{2}\right)^{1/2} \quad (3.1)$$

k: Number of clusters  
n: Sample size

The above formula is mostly used in small volume data sets. Its use in large samples creates difficulties for the researcher in reaching healthy results.

The second method for determining the number of clusters is the one proposed by Marriot;

$$M = k^2|W| \quad (3.2)$$

W = Within -Groups Sum of squares and Cross Products Matrix

M = Number of clusters

The third method of determining the number of clusters is the method developed by Calinsky and Harabasz;

$$C = [Iz(B)/(k - 1)] / [Iz(W)/(n - k)] \quad (3.3)$$

W = Within -Groups Sum of squares and Cross Products Matrix

B = Between-Groups Sum of squares and Cross Products Matrix

The fourth method of determining the number of clusters was proposed by Lewis and Thomas. In this method, two criteria are taken into account when deciding on the number of clusters. The first of these criteria is the explanatory power of the total variance, and the second is that the addition of a new set increases the set variance. Apart from these methods, there are also some informative and advisory rules when deciding on the number of clusters [8].

-Theoretical and practical considerations can suggest a certain number of sets.

- In hierarchical clustering, the distances at which the clusters converge can be used critically. This information can be obtained from the dendrogram.

-In non-hierarchical clustering, the ratio of total Between-Groups variance to Within-Groups variance can be graphed against the number of clusters. The point at which a certain break occurs indicates the appropriate number of clusters. After this point, it is not beneficial to increase the number of clusters.

-Considering the total number of units and the number of variables, the number of clusters obtained should be significant.

#### 4. Data

This study includes earthquake data covering the year 1900 and after, which is published on the website of Boğaziçi University Kandilli Observatory Regional Earthquake-Tsunami Monitoring and Evaluation Center [23]. In this data set, since the earthquake data measured between 1900 and 1980 did not contain significant results, a study was carried out on earthquakes of 3 and above that occurred between 01.01.1980 and 31.12.2022. The dataset contains a total of 50130 earthquake records. Specific concepts related to our data set are as follows;

**Magnitude:** "xM" The concept of Magnitude, which is used as the unit of measurement of earthquakes, is used instead of the Richter scale.

**Depth:** It is the shortest distance from the point where the energy is released in the earthquake to the earth.

**Latitude:** The angular distance of any point north or south of the Equator to the Equator is called Latitude.

**Longitude:** The angular distance of any point east or west of the initial meridian is called Longitude.

When we examine the earthquake data from 1980 to 2022, we reach the following conclusions:

- ❖  $5 \leq M$  "There have been 306 earthquakes with a magnitude of 5 or higher."
- ❖  $4 \leq M < 5$  "There have been 3355 earthquakes between magnitude 4 and 5."
- ❖  $3 \leq M < 4$  "There have been 46469 earthquakes between magnitude 3 and 4."

#### 5. Results and Discussions

50130 earthquake depths and earthquake intensities in our data set were considered as variables and the "K-Means Cluster Analysis" method was used in the SPSS program. First of all, the Hierarchical Clustering Method was used to calculate the optimal number of clusters, and as a result of the dendrogram obtained, it is seen that in figure 2 we need to continue the analysis with 5 clusters.

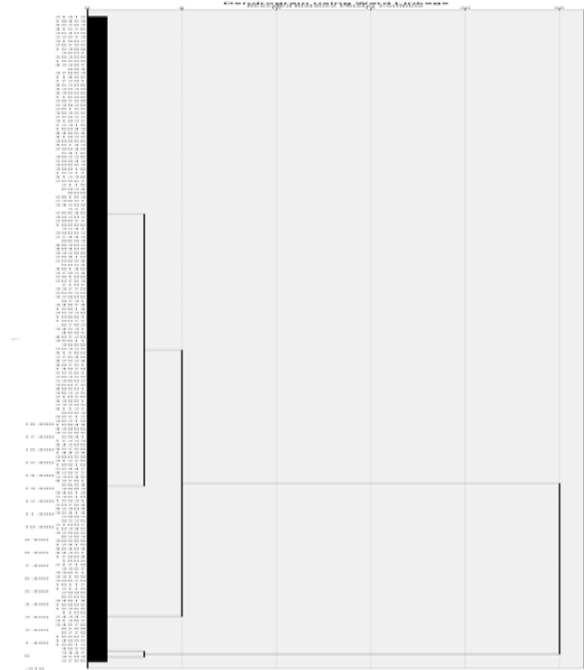


**Figure 2.** Dendrogram representation of depth and magnitudes

Different cluster element membership in dendrograms emerges as a result of differentiation in the sub-dendrogram and is determined by calculating the maximum number of edges [26].

Due to the large volume of our dataset, we will be using the Non-Hierarchical Clustering Method. When we analyze the results obtained by incorporating the 5 clusters identified in the dendrogram, the frequency values of each cluster are presented in Table 1 below;

**Table 1.** Frequency Distribution of 5 Formed Clusters

<b>Clusters</b>	1	487
	2	164
	3	340
	4	42070
	5	7069
<b>Total Frequency</b>		50130

As can be seen Table 1; the most agglomeration occurs in the 4th cluster. When the center depth and magnitude values of each cluster are examined, the following results are obtained.

**Table 2.** 5 Average depth and magnitude of cluster centers

<b>Clusters</b>	1	2	3	4	5
<b>Depth(km)</b>	63.7	136.2	97.7	6.3	20.5
<b>xM</b>	3.6	3.7	3.5	3.3	3.3

47% of the earthquakes in Turkey occurred at a depth of 5 to 10 km and 19% of the earthquakes occurred at a depth of 0 to 5 km as seen in Table 2. When we look at the earthquake intensities, it was observed that 93% of them occurred between 3 and 4 magnitudes. Based on these data, it seems that the most earthquakes are concentrated in the center of the 4th cluster as seen in Table 2.

**Table 3.** 5 Distances of cluster centers relative to each other

Clusters	1	2	3	4	5
1		72.49	34.06	57.33	43.21
2	72.49		38.43	129.82	115.70
3	34.06	38.43		91.39	77.27
4	57.33	129.82	91.39		14.13
5	43.21	115.70	77.27	14.13	

As can be seen from Table 3; it is seen that the earthquakes observed in the 2nd cluster differ from the earthquakes observed in the other clusters at the distance of the concluded earthquake centers from each other. The 1st, 2nd, 3rd, 6th, 24th and 25th regions included in the 2nd cluster are the regions where earthquake faults and earthquake intensities are low and occur deeply. Therefore, there are 302 earthquakes that occur at a depth of 100 km or more. 285 of them occur in these regions. Clusters 4 and 5 have close average magnitudes of 3.3 at their centers, while depths are 6.3 km in cluster 4 and 20.5 km in cluster 5. In this respect, it has been observed that they differ from other clusters.

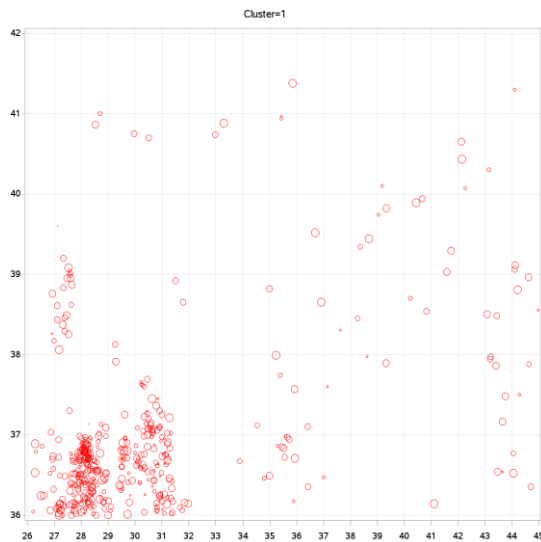


**Figure 3.** The 1st distribution of cluster between northern latitudes (36°-42°) and eastern longitudes (26°-45°)

The center of the 1st cluster was 3.6 magnitude and 63.7 km deep. As can be seen from Figure 3; the 2nd, 3rd, 4th, 5th regions of the 1st cluster are observed intensively and some cluster data are observed in the 39th region.

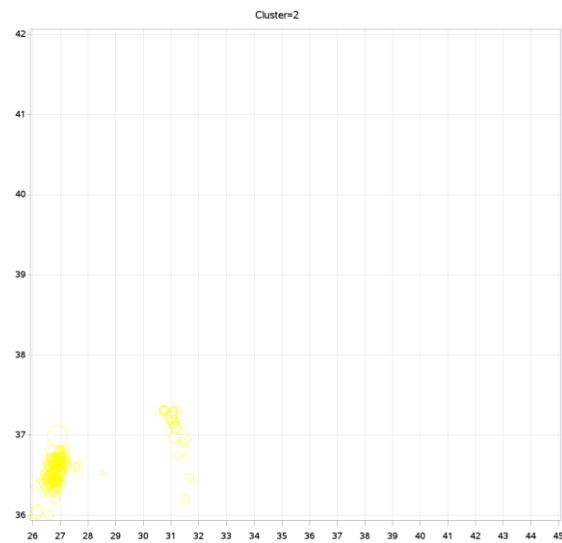


**Figure 4.** The 2nd distribution of the cluster between northern latitudes (36°-42°) and eastern longitudes (26°-45°)

The 2nd cluster formed was centered at a magnitude of 3.7 and a depth 136.2 km. As can be seen from Figure 4; the 2nd cluster, which is clustered around this center, is densely populated by 1st, 2nd, 3rd, 6th, 24th and 25th regions. It has been observed that it consists of data in regions. 2.3% of the earthquakes that occurred in Turkey occurred at depths of more than 35 km.

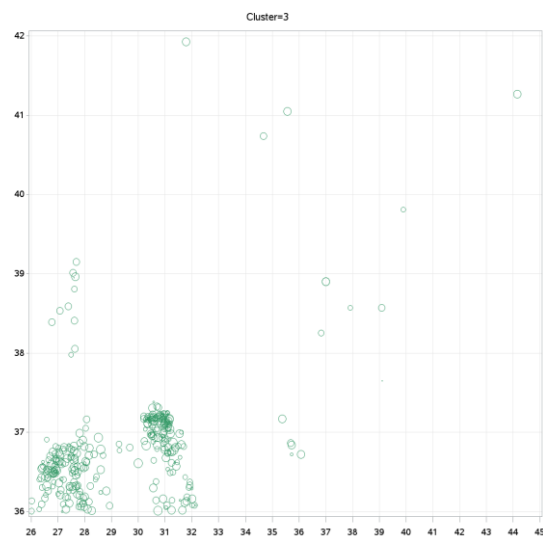


**Figure 5.** The 3rd distribution of the cluster between northern latitudes (36°-42°) and eastern longitudes (26°-45°)

The 3rd cluster formed was centered at 3.5 magnitude and 97.7 km deep. The 3rd cluster, clustered around this center, is densely populated by 1st, 2nd, 3rd, 5th, 6th and 24th regions. It has been observed that it consists of data in regions. As can be seen from Figure 5 and as can be understood from these 3 clusters we have observed, the

potential for earthquakes at every depth and magnitude is seen in the 1st, 2nd, 3rd, 6th and 24th regions. It is seen that these regions we examined on the map are in the Mediterranean, off the coast of Antalya and Datça, as well as in Datça, Marmaris and Burdur. We can say that the Burdur Grabeni in these regions and the Selimiye and Taşlıca Faults in Marmaris produce earthquakes at all depths [27].

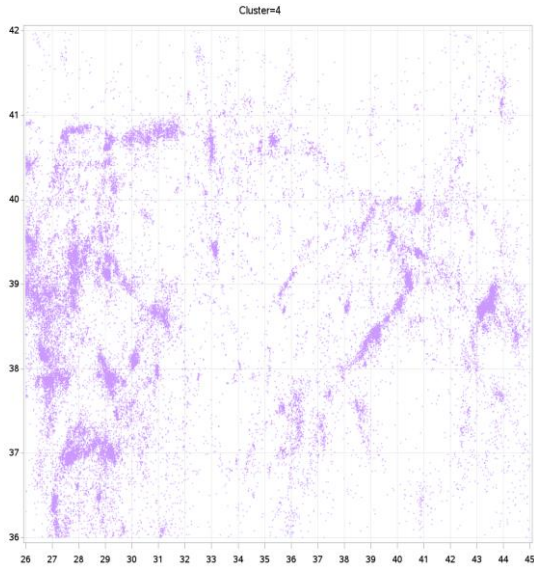


**Figure 6.** The 4th distribution of cluster ( $36^{\circ}$ - $42^{\circ}$ ) between northern latitudes and ( $26^{\circ}$ - $45^{\circ}$ ) eastern longitudes

The 4th cluster formed was centered at 3.3 magnitude and 6.3 km deep. As can be seen from Figure 6; the 4th cluster, which is clustered around this center, generally contains observations from every region. However, some regions where the density is evident stand out. It can be said that the Aegean region, Southern Marmara, Malatya and Lake Van are observed more intensely. The geological structure of the fault lines of the regions in these clusters is also a separate research topic.

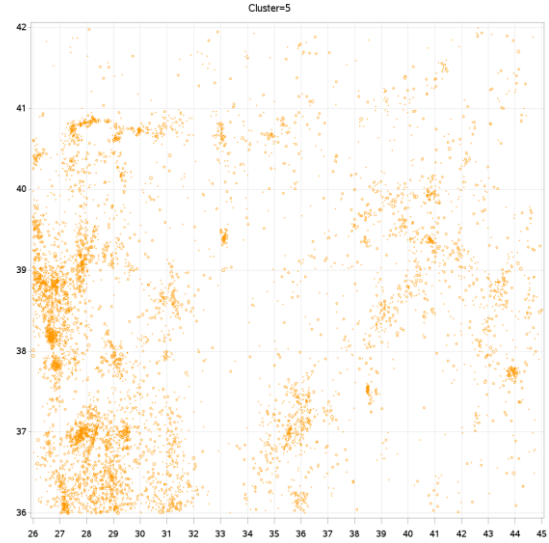


**Figure 7.** The 5th distribution of cluster ( $36^{\circ}$ - $42^{\circ}$ ) between northern latitudes and ( $26^{\circ}$ - $45^{\circ}$ ) eastern longitudes

The 5th cluster formed was centered at 3.3 magnitude and 20.5 km deep. As can be seen from Figure 7; the 5th cluster, which is clustered around this center, is similar to the 4th cluster, and the depth centers are different. In this study, it was observed that certain fault lines became evident in the clustering of earthquakes with magnitude 3 and above that occurred between 1980 and 2022 depending on their depth and magnitude.

## 6. Conclusions

Although this study does not have any limitations, unlike previous studies, cluster analysis was performed on depth and magnitude values and consistent information was obtained. On similar subjects, it has been contributed that clustering analysis can obtain consistent and strong results for numerical variables such as depth, magnitude, etc.

This study was conducted on earthquakes of 3 and above that occurred in Turkey between 01.01.1980 and 31.12.2022. The results of the cluster analysis performed by grouping 5 clusters with non-hierarchical cluster analysis of earthquake data show that intra-group and inter-group relationships were detected. In addition, the density varies between regions, and at this point, examining the geological structures of the fault lines of the regions considered in the clusters constitutes a separate research topic.

Clustering analysis studies in earthquakes can be detailed by diversifying the techniques and methods or certain region used in following studies.

## Author's Contributions

**Ahmet Murat ŞEN:** Conducted the literature review, performed analysis, evaluated the results, and wrote the manuscript.

**Zeki YILDIZ:** Contributed to the analysis advancement, manuscript preparation, interpreted findings.

## Ethics

There are no ethical issues after the publication of this manuscript.

## References

- [1]. Özel, G., Solmaz, A. (2012). Estimation of earthquake recurrence time in Turkey and investigation of seismicity according to neotectonic regions with Markov chain. *Çankaya University Journal of Science and Engineering*, 9(2), 125-138.
- [2]. Doğaner, A., Çalık S. (2012). Investigation of the relationship between seismic activities in and around Elazığ and earthquake parameters. *Firat University Journal of Science*, 26(1), 73-77.
- [3]. Kasap, R., Gürlen, Ü. (2003). Obtaining recurrence years for earthquake magnitudes: The case of Marmara Region. *Journal of Doğuş University*, 4(2), 157-166.
- [4]. Orman, F. (2021), Investigation of Eurasian Countries in terms of Economic Freedom with Cluster Analysis. *International Conference on Eurasian Economies: 24-25 August 2021, Istanbul: p.79-86.*
- [5]. Boehmke, B., & Greenwell, B. (2020). Hands-on machine learning with R. Boca Raton: CRC Press, Taylor and Francis Group.
- [6]. Alpar, R. (2022). Applied Statistics and Validity-Reliability with Examples from Sports. *Health and Educational Sciences 7th Edition. Detay Publishing*, 2022.
- [7]. Demircioğlu M., Eşiyok, S. (2019). Classification of countries by cluster analysis in the fight against the Covid-19 pandemic. *Istanbul Commerce University Journal of Social Sciences*, 37, 369-389.
- [8]. Koldere Akın, Y. (2008). Clustering Algorithms and Clustering Analysis in Data Mining. *Marmara University Doctoral Thesis*, 8, 10, 16, 26-29.
- [9]. Lean, L., Ricardo ve Powers L, Thomas. (1997). A Taxonomy of Countries Based on Inventive Activity. *International Marketing Review*, Volume 14, No.6, 1997, ss.445-460.
- [10]. Tatlıdil, Hüseyin. Applied Multivariate Statistical Analysis. Ankara: Ziraat Printing House, 2002, ss 330-341.
- [11]. Özdamar, Kazım. Statistical Data Analysis with Package Programs. *Eskisehir: Kaan Bookstore*, 1999.
- [12]. Ravinda, Khattree ve Naik N. Dayanand. Multivariate Data Reduction and Discrimination. *First Edition. North Caroline: Cary*, 2002.
- [13]. Latin, M. James, Carroll J. Douglas ve Paul E. Green. Analyzing Multivariate Data. *United States: Thomson Brooks-Cole*, 2003.
- [14]. NCSS. User Guide, Kaysville, *National Council for the Social Studies Incorporated*, 2001
- [15]. Novanti P., Setyorini D., Rafflesia U., 2017. K-Means Cluster Analysis in Earthquake Epicenter Clustering. *International Journal of Advances in Intelligent Informatics*, 3(2). 2017.
- [16]. Kamat R.K. ve Kamat R.S., 2017. Earthquake Cluster Analysis: K-Means Approach, 2017. *Journal of Chemical and Pharmaceutical Sciences*, 10(1). 2017.
- [17]. Samadi et al. (2020), Robust Earthquake Cluster Analysis Based On K-Nearest Neighbor Search, 2020. *Pure and Applied Geophysics*, ISSN 0033-4553. 2020.
- [18]. Scitovski, R., Scitovski, S. (2013). A fast partitioning algorithm and its application to earthquake investigation. *Computers & Geosciences Volume 59*, 124-131.
- [19]. Morales-Esteban, A., Martínez-Alvarez, F., Scitovski, S., Scitovski, R., (2014). A fast partitioning algorithm using adaptive Mahalanobis clustering with application to seismic zoning. *Computers & Geosciences Volume 73*, 132-141.
- [20]. Prozorov, A. G., Dziewonski, A. M. (1982). A Method of Studying Variations in the Clustering Property of Earthquakes: Application to the Analysis of Global Seismicity. *Journal of Geophysical Research*, Volume 87, No. B4, pp. 2829-2839.
- [21]. Yan Y. Kagan, David D. Jackson (1991). Long-term earthquake clustering. *Geophysical Journal International*, Volume 104, 117-133.
- [22]. Scitovski, S. (2018). A density-based clustering algorithm for earthquake zoning. *Computers & Geosciences Vol.110*, 90-95.
- [23]. Kandilli observatory and earthquake research institute website active fault maps accessed on 17.11.2023. <http://www.koeri.boun.edu.tr/sismo/zeqdb/>
- [24]. Hair, J.F., Anderson, R. E., Tatham, R. L., & Black, W. C., (1995). Multivariate Data Analysis with Readings. *New Jersey: Prentice Hall (1995)*.
- [25]. Yalçın, N., (2013). Clustering Analysis and Application. *Firat University Institute of Natural and Applied Sciences Master Thesis*, 21,
- [26]. Jafarzadegan, M., Safi-Esfahani, F.ve Beheshti, Z. (2019). Combining hierarchical clustering approaches using the PCA method, *Expert Systems with Applications*, 137(15), 1-10. <https://doi.org/10.1016/j.eswa.2019.06.064>.
- [27]. General Directorate of Mining Technical Exploration website active fault maps accessed on 04.12.2023. <https://www.mta.gov.tr/v3.0/sayfalar/hizmetler/diri-fay-haritalari/>

# Comparative Anatomy, Pollen and Seed Morphology of Two *Verbascum* Varieties (Scrophulariaceae) and Their Taxonomic Significance

Murat KILIÇ<sup>1\*</sup> , Fatma MUNGAN KILIÇ<sup>1</sup> 

<sup>1</sup> Department of Crops and Animal Production, Mardin Artuklu University, 47200 Mardin, Artuklu, Turkey

\*[muratkiloc04@gmail.com](mailto:muratkiloc04@gmail.com)

\* Orcid No: 0000-0002-6408-9660

Received: 7 February 2024

Accepted: 25 March 2024

DOI: 10.18466/cbayarfb.1433245

## Abstract

In this study, the anatomical, palynological, and seed micromorphological traits of two *Verbascum* varieties found in the Southeastern Anatolia Region were investigated. These variations are *V. sinuatum* subsp. *sinuatum* var. *adenosepalum* Murb. and *V. sinuatum* subsp. *sinuatum* var. *sinuatum* L. Cross-sections from the taxa's roots, stems, and leaves were viewed under a light microscope for anatomical study. The xylem components play a significant role in the taxonomic root portions. The pith area is a broad region in stem sections, and the upper portion of the epidermis cells is encircled by a distinct indented cuticle layer. The leaves' primary vein is represented by open collateral bundles. Pollen grains in *Verbascum sinuatum* subsp. *sinuatum* var. *adenosepalum* are tricolporate-tricolpate, prolate-spheroidal, and have reticulate exine ornamentation. Similarly, pollen grains in *V. sinuatum* subsp. *sinuatum* var. *sinuatum* are tricolporate-tricolpate, prolate, and have reticulate exine ornamentation. The brown seeds of *V. sinuatum* subsp. *sinuatum* var. *adenosepalum* and *V. sinuatum* subsp. *sinuatum* var. *sinuatum* have an alveolate, deep and wide posterior region, a truncated beak, and a prismatic-oblong shape. The ornamentation of the seed coat is made up of irregular polygonal cells that have noticeable and dense vesicles. The importance of a few traits in the *Verbascum* variety delimitation has been investigated in this study. For the purpose of supporting ancestral traits in the infrageneric classification and helping with genus systematics, some pollen and seed characters which are typically connected to pollen and seed micromorphological and anatomical patterns can be applied.

**Keywords:** anatomy, pollen, seed, SEM, Southeastern Anatolia, Turkey *Verbascum*

## 1. Introduction

*Verbascum* L. contains approximately 360 species in the World [1]. Although it is extensively dispersed throughout Eurasia and North Africa, a sizable region that includes Anatolia, the southern Balkans, the Middle East, the Caucasus, and northwest Iran has the highest diversity of species [2]. It has been split into 13 artificial groups and is represented by 257 species and 132 additional hybrids and with 202 endemic species (80% of the total), the genus has an extremely high endemism ratio in Flora of Turkey [3-6]. The genus *Verbascum* presents taxonomic challenges, and its infrageneric categorization is somewhat contrived and informal. Moreover, the challenges of producing a practical key may make taxonomic identification tough as well. Many scientists in Turkey and around the world are studying

the morphology and systematics of *Verbascum* taxa in order to achieve this goal [7].

Many SEM investigations [7-15]. are based on the pollen morphology of some *Verbascum* species taxa. Juan et al. [8], Attar et al. [9], Kheiri et al. [16], Karaveliogullari et al. [11], Kılıç [14], Mungankılıç & Kılıç [15], Cabi et al. [17], and Duman et al. [18] have studied the seed micromorphology of the genus *Verbascum*. The genus has had very few anatomical research [12-16, 19-22], and there are still unexplored taxa in Turkey. The anatomical features for *Verbascum sinuatum* subsp. *sinuatum* var. *adenosepalum* Murb. and *V. sinuatum* subsp. *sinuatum* var. *sinuatum* L. (group H) are absent, as is the palynological and seed micromorphology. The purpose of this study was to determine the relationships between two *Verbascum* varieties that are found throughout the Southeastern Anatolia Region. This information was obtained

through comparative analysis, which helped to highlight the significance of anatomical characteristics as well as the fine structure of the surfaces of the pollen and seeds. The information gathered should be used to categorize the group and genus in further research or to offer strong support for its assessment.

## 2. Materials and Methods

A number of locations in Diyarbakır, Mardin, and Şanlıurfa were used to gather the specimens of *Verbascum sinuatum* subsp. *sinuatum* var. *adenosepalum* and *V. sinuatum* subsp. *sinuatum* var. *sinuatum* (Figure 1). The voucher samples were kept in the herbarium of the Kızıltepe Vocational School, Mardin Artuklu University, Turkey's Department of Plants and Animal Production. The collection locations, the collector's number, and the habitat of the samples that were examined for their micromorphological characteristics list in the table 1. The plant's taxonomic description was established in accordance with Davis et al. [4] and Karaveliogulları [5].

For use in anatomical research, collected specimens were stored in falcon tubes with 70% alcohol. Using a razor, sections were cut from the plant's root, stem, and leaf sections. They were then prepared by staining them with safranin-fast green, viewed under a light microscope, and taken pictures of [23]. The anatomy uses terms that correspond to those of Metcalfe and Chalk [24].

All of the pollen grains were subjected to light (LM) and (SEM) palynological studies using the conventional techniques outlined by Erdtman [25]. In accordance

with Wodehouse's [26] standard protocol, pollen grains were prepared for LM examination. They were examined under an Isolab standard microscope in glycerin-water. For the purposes of the palynological analysis, thirty pollen grains per specimen were considered sufficient [16-17, 26]. Pollen washed with distilled water, allowed to air dry, then immediately mounted on stubs using double-sided tape and covered in gold for SEM. A ZEISS EVO 50 scanning electron microscope was used to capture the photomicrographs. Under a light microscope, the measurements of P (Polar axis length), E (Equatorial diameter), Clg (Colpus length), Clt (Colpus width), Plg (Porus length), Plt (Porus width), Ex (Exine thickness), and In (Intine thickness) for thirty pollen grains were made. The P/E ratio was also computed. The nomenclature used for the pollen is in accordance with Punt et al. [27]. As seen in Table 2, the data are given as the minimum, maximum, and mean.

Using an Isolab stereomicroscope, the seeds were initially inspected to make sure they were developed and of a reasonable size. Thirty mature seeds were measured in order to get the average seed sizes. After treating the seeds with distilled water to remove any dirt, the air-dried seeds were placed on stubs and covered for SEM. The ZEISS EVO 50 scanning electron microscope was used to take the photomicrographs. The terms used to describe the morphological traits of the seeds are based on those found in Juan et al. [8], and Attar et al. [28]. The capsule uses terminology that is consistent with Attar et al. [28].



**Figure 1.** General and flower close-up view of plants belonging to *Verbascum* varieties from the area, (A) *Verbascum sinuatum* subsp. *sinuatum* var. *adenosepalum*, (B) *V. sinuatum* subsp. *sinuatum* var. *sinuatum*.

**Table 1.** *Verbascum sinuatum* subsp. *sinuatum* var. *adenosepalum* and *V. sinuatum* subsp. *sinuatum* var. *sinuatum* species used for anatomy and morphology studies and collected localities.

Species	Collection areas and habitat	Collector number	
<i>V. sinuatum</i> subsp. <i>sinuatum</i> var. <i>adenosepalum</i>	Mardin: Artuklu, road side, 37°21'47"N 40°44'11"E, 893 m.	M.Kılıç 270	
	Mardin: Artuklu, road side, creek edge, 37°21'37"N 40°40'26"E, 930 m.	M.Kılıç 305	
	Mardin: Midyat, road side, 37°27'55"N 41°10'53"E, 985 m.	M.Kılıç 310	
	Mardin: Yeşilli, creek edge, 37°17'45"N 40°50'37"E, 694 m.	M.Kılıç 329	
	Mardin: Savur, road side, stony area, 37°32'47"N 40°53'35"E, 833 m.	M.Kılıç 339-2	
	Diyarbakır: Çınar, road side, 37°42'08"N 40°26'02"E, 716 m.	M.Kılıç 347-1	
	Diyarbakır: Yenişehir, road side, damp and wet area, 747 m.	M.Kılıç 348	
	Mardin: Artuklu, road side, next to water channel, 37°11'44"N 40°57'27"E, 607 m.	M.Kılıç 360-1	
	Mardin: Artuklu, road side, rocky slope, 37°13'02"N 40°57'58"E, 674 m.	M.Kılıç 362	
	Mardin: Artuklu, road side, creek edge, 37°22'11"N 40°41'10"E, 983 m.	M.Kılıç 367	
	Mardin: Yeşilli, road side, cultivated area, 37°18'37"N 40°49'49"E, 737 m.	M.Kılıç 368	
	<i>V. sinuatum</i> subsp. <i>sinuatum</i> var. <i>sinuatum</i>	Mardin: Yeşilli, road side, rocky slope, 37°18'31"N 40°49'54"E, 733 m.	M.Kılıç 328-2
		Mardin: Savur, road side, 829 m.	M.Kılıç 337-2
		Mardin: Savur, road side, 37°32'32"N 40°51'19"E, 834 m.	M.Kılıç 338-2
Diyarbakır: Çınar, road side, 37°42'08"N 40°26'02"E, 716 m.		M.Kılıç 347-2	
Mardin: Artuklu, road side, 37°20'49"N 40°39'03"E, 932 m.		M.Kılıç 366	
Şanlıurfa: Karaköprü, road side, stony area, 37°19'54"N 38°48'00"E, 676 m.		M.Kılıç 389	
Mardin: Savur, road side, 37°32'32"N 40°51'19"E, 834 m.		M.Kılıç 408-2	

### 3. Results and Discussion

Several anatomical, pollen, and seed structural characteristics of *Verbascum sinuatum* subsp. *sinuatum* var. *adenosepalum* and *V. sinuatum* subsp. *sinuatum* var. *sinuatum* are reported in this work. The root, stem, and leaf tissues and cells' biometric measurements are listed in Table 2 and displayed in Figures 2, 3, and 4. Table 3 and Figure 5 present a summary of the properties of pollen grains. Table 4 summarizes the morphological properties of the seed grains, which include their size, shape, color, and surface features. Figure 6 illustrates these properties. Table 5 summarizes the morphological properties of the capsule grains,

which include their size, shape, and color features. Figure 7 illustrates these properties.

#### 3.1. Anatomy Characteristics

##### 3.1.1. Root anatomy

The periderm layer on the outermost surface of *Verbascum sinuatum* subsp. *sinuatum* var. *adenosepalum* is irregularly shaped and measures 13.49-43.56 x 9.14-34.97 µm (micrometer) in cross-sections taken from the root. A multi-layered parenchyma measuring 6.88-40.95 x 8.14-20.29 µm is located beneath the periderm. Phloem cells with 3-5

layers and sizes of 5.80-17.00 x 5.90-12.87  $\mu\text{m}$  are seen beneath the parenchyma. There is unclear cambium. The center of the root is filled with xylem, which occupies a greater area. Trachea cells measure between 20.11 and 94.49 x 22.50 and 89.61  $\mu\text{m}$  and are larger than tracheid cells. They are also sporadically placed. The xylem has a wider coverage area than the phloem. The two to six rows of rectangular cells that make up its pith rays. Polygonal or circular parenchymatous cells make up the pith (Figure 2, Table 2).

*V. sinuatum* subsp. *sinuatum* var. *sinuatum* cross-sections show that the periderm layer on the outermost surface of the root has irregularly shaped cells and measures 9.83-40.80 x 7.64-21.01  $\mu\text{m}$ . A multi-layered parenchyma measuring 8.47-52.69 x 8.71-40.60  $\mu\text{m}$  is located beneath the periderm. Phloem cells with three to four layers and dimensions of 5.79 to 15.14 x 4.06 to 15.73  $\mu\text{m}$  are found beneath the parenchyma. There is unclear cambium. The center of the root is filled with xylem, which occupies a greater area. Trachea cells range in size from 14.86-65.96 x 25.63-56.19  $\mu\text{m}$ , are larger than tracheid cells, and are sporadically distributed. The xylem has a wider coverage area than the phloem. Its pith rays are made up of two to four rows of rectangular cells. Polygonal or circular parenchymatous cells make up the pith (Figure 2, Table 2).

### 3.1.2. Stem anatomy

The stem of *V. sinuatum* subsp. *sinuatum* var. *adenosepalum* has cross-sections measuring 4.88-9.57  $\mu\text{m}$  that show a single-layered epidermis coated in an undulate cuticle. Oval or rectangular cells measuring 6.34-19.99 x 6.03-12.47  $\mu\text{m}$  make up the epidermis. The epidermis contains branch multicellular hairs. Three to five rows of collenchyma cells measuring 7.16 to 25.19 x 7.49 to 20.41  $\mu\text{m}$  are located beneath the epidermis. Ovular and orbicular parenchymatous cells arranged in 7-10 rows and measuring 10.10-37.83 x 8.86-27.09  $\mu\text{m}$  make up parenchyma tissue. Underneath the parenchyma are 4-8 rows of sclerenchyma layers. There is a thin cambium. Phloem measures 2.53-7.87 x 2.41-5.14  $\mu\text{m}$ , but xylem is greater than phloem and measures 12.98-44.61 x 15.09-59.81  $\mu\text{m}$ . The parenchymatous cells that make up the pith are hexagonal or circular, and their intercellular gaps have dimensions of 10.33-26.46 x 9.72-29.28  $\mu\text{m}$  (Figure 3, Table 2).

*V. sinuatum* subsp. *sinuatum* var. *sinuatum* cross-sections measuring 6.14-10.49  $\mu\text{m}$  showed a single-layered epidermis coated in an undulating cuticle. Oval or rectangular cells measuring 9.95-30.91 x 5.37-17.22  $\mu\text{m}$  make up the epidermis. The epidermis contains complicated multicellular hairs. Three to four rows of 5.25-21.63 x 5.18-23.93  $\mu\text{m}$  collenchyma cells lie beneath the epidermis. Oval orbicular parenchymatous

cells arranged in 5-7 rows and measuring 11.25-43.77 x 7.98-23.34  $\mu\text{m}$  are the constituents of parenchyma tissue. Underneath the parenchyma are 2-4 rows of sclerenchyma layers. There is no difference in the cambium. Size-wise, phloem measures 4.56-14.26 x 3.99-9.40  $\mu\text{m}$ , whereas xylem is larger than phloem and measures 7.35-23.55 x 11.38-35.29  $\mu\text{m}$ . The parenchymatous cells that make up the pith are hexagonal or circular, and their intercellular gaps range in size from 17.20 to 65.10 x 16.94 to 64.43  $\mu\text{m}$  (Figure 3, Table 2).

### 3.1.3. Leaf anatomy

*V. sinuatum* subsp. *sinuatum* var. *adenosepalum*'s lamina of the adaxial and abaxial epidermis cross-sections revealed that both epidermises have a single row of rectangular or oval cells, are covered in branched, glandular, and eglandular multicellular hairs, and have a cuticle that is 3.50-5.40  $\mu\text{m}$  thick. There are open collateral vascular bundles. Parenchymal cells encircle the bent vascular bundle. A single layer is formed by the radial arrangement of the xylem components. The midrib is fully grown. A sizable portion of the vascular bundle's surrounding parenchyma layer is covered. Parenchymal tissue cells are organized firmly and in polygons. The diameters of the cells in the lower epidermis are 5.57-25.84 x 7.59-26.56  $\mu\text{m}$ , whereas the cells in the upper epidermis are 12.89-21.96 x 13.03-23.98  $\mu\text{m}$ . The epidermis on top is bigger than that on the bottom. The hypodermis is located beneath the top and lower epidermis. Palisade and spongy parenchyma make up the 144.38-242.77  $\mu\text{m}$  thick mesophyll tissue, which is composed of 1-2 layers of palisade parenchyma above the lower epidermis and 2-3 layers below the upper epidermis. Palisade parenchyma cells are long, uneven, cylindrical or quadrangular, and measure 11.85-19.68 x 18.98-43.66  $\mu\text{m}$ . Spongy parenchyma cells, which are made up of two to three rows of cells, are located between the lower and upper palisade parenchyma cells. The oval or polygonal cells of spongy parenchyma measure 11.24-20.70 x 11.36-31.60  $\mu\text{m}$  and have greater intercellular spacing. Additionally, idioblasts have been found in the leaf mesophyll tissue (Figure 4, Table 2).

In *V. sinuatum* subsp. *sinuatum* var. *sinuatum*, cross-sections of the lamina of the adaxial and abaxial epidermis revealed that both epidermises have a single row of rectangular or oval cells, are covered in multicellular hairs that are glandular, eglandular, and branched, and have a cuticle that is 4.69-9.19  $\mu\text{m}$  thick. There are open collateral vascular bundles. Parenchymal cells encircle the bent vascular bundle. A single layer is formed by the radial arrangement of the xylem components. The midrib is fully grown. A sizable portion of the vascular bundle's surrounding parenchyma layer is covered. Parenchymal tissue cells are organized firmly and in polygons. The cell

diameters of the upper and lower epidermis are 6.89-21.23 x 7.76-16.92  $\mu\text{m}$  and 8.12-21.27 x 3.63-18.41  $\mu\text{m}$ , respectively. The epidermis on top is bigger than that on the bottom. The hypodermis is located beneath the top and lower epidermis. Mesophyll tissue has a thickness of 178.27–270.57  $\mu\text{m}$  and is composed of 1-2 layers of palisade parenchyma above the lower epidermis and 2-3 layers of spongy parenchyma below the upper epidermis. Palisade parenchyma cells are irregular,

long, cylindrical or quadrangular, and measure 9.86-19.49 x 29.45-48.46  $\mu\text{m}$ . Spongy parenchyma cells, which are made up of two to three rows of cells, are located between the lower and upper palisade parenchyma cells. The oval or polygonal cells of spongy parenchyma measure 12.25–24.00 x 16.36–33.43  $\mu\text{m}$  and have greater intercellular spacing. Additionally, idioblasts have been found in the leaf mesophyll tissue (Figure 4, Table 2).

**Table 2.** The anatomical measurements of varieties *Verbascum* ( $\mu\text{m}$ ).

Species / Tissues	Width			Length		
	Min.	Mak.	Mean $\pm$ S.	Min.	Mak.	Mean $\pm$ S.
<i>V. sinuatum</i> subsp. <i>sinuatum</i> var. <i>adenosepalum</i>						
Root						
Peridermis cell	13.49	43.56	26.67 $\pm$ 8.91	9.14	34.97	19.65 $\pm$ 6.17
Parenchyma cell	6.88	40.95	21.91 $\pm$ 9.36	8.14	20.29	14.87 $\pm$ 3.14
Phloem cell	5.80	17.00	9.83 $\pm$ 2.94	5.90	12.87	9.26 $\pm$ 1.87
Trachea cell	20.11	94.49	54.11 $\pm$ 19.70	22.50	89.61	56.84 $\pm$ 19.38
<i>V. sinuatum</i> subsp. <i>sinuatum</i> var. <i>sinuatum</i>						
Peridermis cell	9.83	40.80	19.27 $\pm$ 7.76	7.64	21.01	14.22 $\pm$ 3.92
Parenchyma cell	8.47	52.69	29.65 $\pm$ 12.11	8.71	40.60	22.11 $\pm$ 8.07
Phloem cell	5.79	15.14	9.48 $\pm$ 2.50	4.06	15.73	6.61 $\pm$ 2.52
Trachea cell	14.86	65.96	41.45 $\pm$ 16.39	25.63	56.19	40.38 $\pm$ 10.60
<i>V. sinuatum</i> subsp. <i>sinuatum</i> var. <i>sinuatum</i>						
Stem						
Cuticle	-	-	-	4.88	9.57	7.46 $\pm$ 1.43
Epidermis cell	6.34	19.99	12.85 $\pm$ 3.59	6.03	12.47	9.08 $\pm$ 1.68
Collenchyma cell	7.16	25.19	14.69 $\pm$ 4.45	7.49	20.41	12.82 $\pm$ 3.44
Parenchyma cell	10.10	37.83	20.49 $\pm$ 8.03	8.86	27.09	16.26 $\pm$ 5.69
Phloem cell	2.53	7.87	4.80 $\pm$ 1.32	2.41	5.14	3.62 $\pm$ 0.81
Trachea cell	12.98	44.61	30.89 $\pm$ 8.04	15.09	59.81	40.12 $\pm$ 12.40
Pith cell	10.33	26.46	18.53 $\pm$ 4.62	9.72	29.28	18.13 $\pm$ 4.84
<i>V. sinuatum</i> subsp. <i>sinuatum</i> var. <i>sinuatum</i>						
Cuticle	-	-	-	6.14	10.49	8.28 $\pm$ 1.33
Epidermis cell	9.95	30.91	17.19 $\pm$ 4.82	5.37	17.22	10.64 $\pm$ 3.62
Collenchyma cell	5.25	21.63	13.12 $\pm$ 3.77	5.18	23.93	11.59 $\pm$ 4.19
Parenchyma cell	11.25	43.77	24.45 $\pm$ 8.38	7.98	23.34	14.00 $\pm$ 4.00
Phloem cell	4.56	14.26	8.79 $\pm$ 2.34	3.99	9.40	6.79 $\pm$ 1.52
Trachea cell	7.35	23.55	16.42 $\pm$ 4.81	11.38	35.29	22.37 $\pm$ 6.35
Pith cell	17.20	65.10	38.76 $\pm$ 14.39	16.94	64.43	38.07 $\pm$ 14.53
<i>V. sinuatum</i> subsp. <i>sinuatum</i> var. <i>sinuatum</i>						
Leaf						
Cuticle	-	-	-	3.50	5.40	4.31 $\pm$ 0.60
Upper epidermis cell	12.89	21.96	16.50 $\pm$ 2.92	13.03	23.98	16.63 $\pm$ 4.00
Palisade parenchyma	11.85	19.68	15.05 $\pm$ 2.19	18.98	43.66	30.23 $\pm$ 5.61
Spongy parenchyma	11.24	20.70	15.60 $\pm$ 2.33	11.36	31.60	24.20 $\pm$ 5.01
Mesophyll layer	-	-	-	144.38	242.77	181.71 $\pm$ 20.68
Lower epidermis cell	5.57	25.84	12.66 $\pm$ 4.69	7.59	26.56	12.78 $\pm$ 4.13
<i>V. sinuatum</i> subsp. <i>sinuatum</i> var. <i>sinuatum</i>						
Cuticle	-	-	-	4.69	9.19	6.29 $\pm$ 1.12
Upper epidermis cell	6.89	21.23	14.72 $\pm$ 4.16	7.76	16.92	11.54 $\pm$ 3.07
Palisade parenchyma	9.86	19.49	14.20 $\pm$ 2.48	29.45	48.46	40.82 $\pm$ 4.94
Spongy parenchyma	12.25	24.00	17.34 $\pm$ 3.01	16.36	33.43	23.74 $\pm$ 4.13
Mesophyll layer	-	-	-	178.27	270.57	205.50 $\pm$ 20.93
Lower epidermis cell	8.12	21.27	12.40 $\pm$ 3.36	3.63	18.41	9.71 $\pm$ 3.06

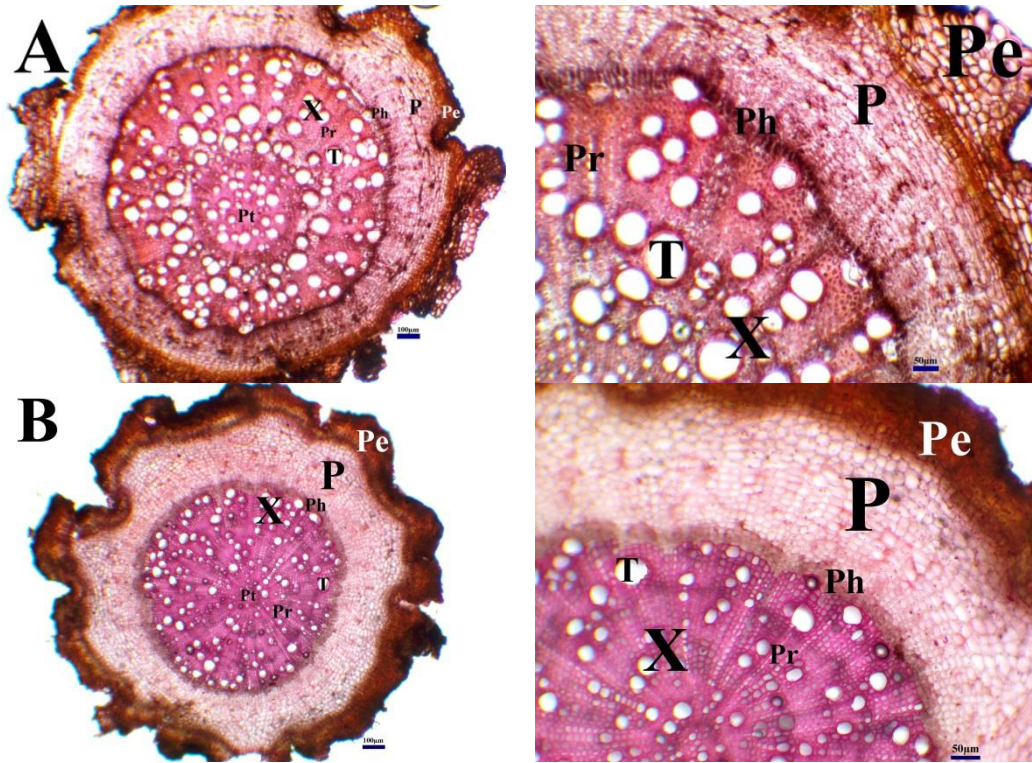


**Figure 2.** Cross-section of the root of A: *V. sinuatum* subsp. *sinuatum* var. *adensepalum*, B: *V. sinuatum* subsp. *sinuatum* var. *sinuatum*. Pe: Periderm, P: Parenchyma, Ph: Phloem, X: Xylem, Pr: Pith ray, T: Trachea, Pt: Pith region.

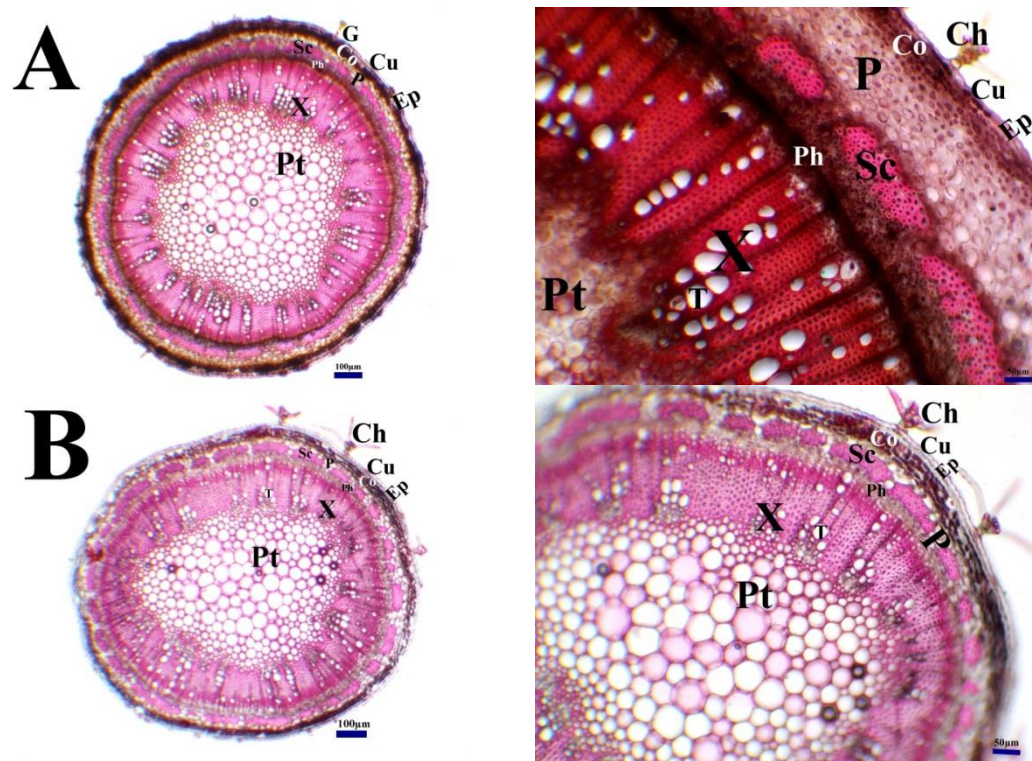


**Figure 3.** Cross-section of the stem of A: *V. sinuatum* subsp. *sinuatum* var. *adensepalum*, B: *V. sinuatum* subsp. *sinuatum* var. *sinuatum*. G: Glandular hair, Ch: Candelabra hair, Cu: Cuticle, Ep: Epidermis, Co: Collenchyma, P: Parenchyma, Sc: Sclerenchyma, Ph: Phloem, X: Xylem, T: Trachea, Pt: Pith region.

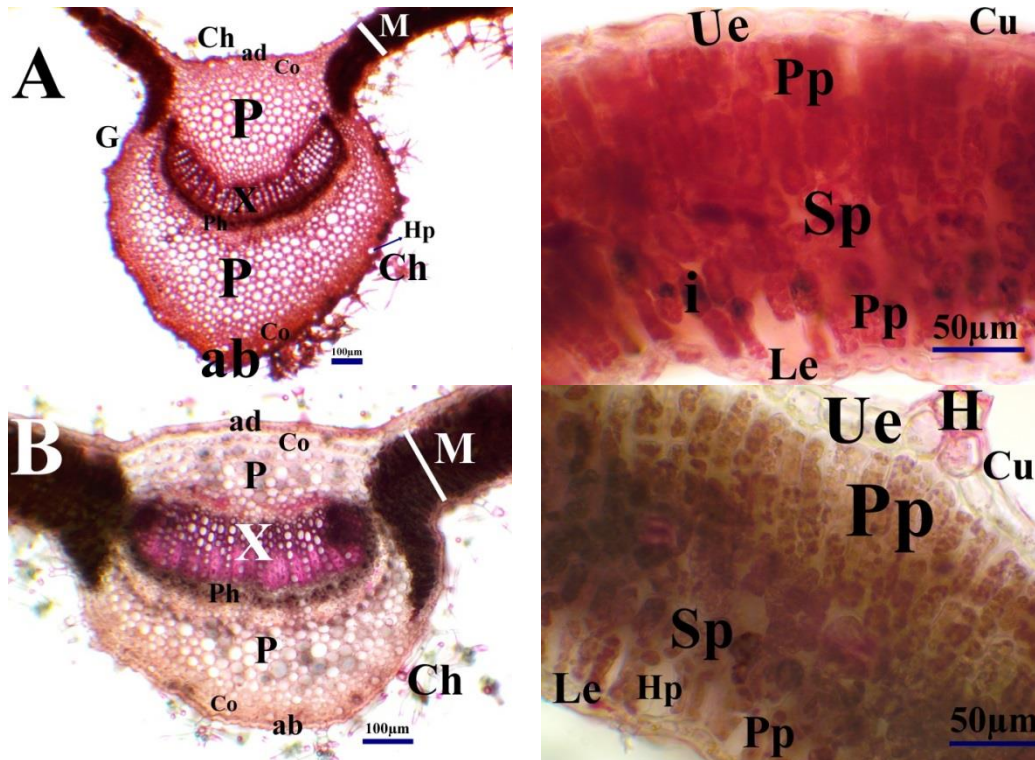


**Figure 4.** Cross-section of the leaves of A: *V. sinuatum* subsp. *sinuatum* var. *adenosepalum*, B: *V. sinuatum* subsp. *sinuatum* var. *sinuatum*. G: Glandular hair, H: Hair, Ch: Candelabra hair, M: Mesophyll layer, ad: Adaxial surface, Co: Collenchyma, P: Parenchyma, X: Xylem, Ph: Phloem, ab: Abaxial surface, Ue: Upper epidermis, Le: Lower epidermis, Pp: Palisade parenchyma, Sp: Spongy parenchyma, Hp: Hypodermis, i: idioblast.

### 3.2. Pollen morphology

#### 3.2.1. Size, symmetry and Shape

*Verbascum* pollen grains have radial symmetry and are isopolar. The prolate-spheroidal and prolate pollens of the variations have an equatorial diameter of 4.41-18.11 µm and a polar axis of 10.18-16.61 µm. According to Table 3 and Figure 5, they are larger in *V. sinuatum* subsp. *sinuatum* var. *adenosepalum* and smaller in *V. sinuatum* subsp. *sinuatum* var. *sinuatum*.

#### 3.2.2. Apertures

*Verbascum* pollen grains are tricolporate (eighty-three percent of *V. sinuatum* subsp. *sinuatum* var. *sinuatum* and seven percent of *V. sinuatum* subsp. *sinuatum* var. *adenosepalum* are tricolporate). The dimensions of the colpus are length (7.58-14.78 µm) and breadth (1.74-4.61 µm), with sharp edges and defined, regular margins. The porus measures 1.19–5.59 µm in width and 2.15–6.31 µm in length. (Figure 5, Table 3).

#### 3.2.3. Exine, intine and ornamentation

The thickness of the exine varies between 0.44 and 1.23 µm. Intine thickness ranges from 0.20 to 0.83 µm (Table 3). In the two examined types, exine sculpturing is reticulate (Table 3, Figure 5).

### 3.3. Seed morphology

#### 3.3.1. Seed size

The measurements show that the dimensions range from 0.57 to 1.11 mm in length and 0.31 to 0.68 mm in width for each species. According to Table 4 and Figure 6, they are larger in *V. sinuatum* subsp. *sinuatum* var. *sinuatum* and smaller in *V. sinuatum* subsp. *sinuatum* var. *adenosepalum*.

#### 3.3.2. Seed Shape

Within the genus *Verbascum*, species and infra-specific taxa can be distinguished by their seed morphology. Among the examined species, the morphologies of the seeds were found to be prismatic-oblong with ±shallow alveolate and alveolate (Table 4, Figure 6).

#### 3.3.3. Apex of the seeds

In *V. sinuatum* subsp. *sinuatum* var. *sinuatum* and *V. sinuatum* subsp. *sinuatum* var. *adenosepalum*, the seeds have large beaks and a deep-broad back (Table 4, Figure 6).

#### 3.3.4. Seed color

Two distinct seed colors were detected in this study: light brown and brown (Table 4, Figure 6).

### 3.3.5. Seed ornamentation

The seed coat has an alveolate or longitudinally ridged appearance due to the irregular polygonal cells with distinct and tightly packed vesicles (Table 4, Figure 6).

### 3.4. Capsule morphology

The measurements show that the length and width of *Verbascum sinuatum* subsp. *sinuatum* var. *adenosepalum* range from 3.33 to 4.75 mm and 2.48 to 3.46 mm, respectively, while the dimensions of *V. sinuatum* subsp. *sinuatum* var. *sinuatum* range from 1.76 to 2.52 mm and 2.11 to 2.21 mm, respectively.

While the capsules of *V. sinuatum* subsp. *sinuatum* var. *sinuatum* are spheroidal and ovate, those of *V. sinuatum* subsp. *sinuatum* var. *adenosepalum* are ovate and rectangular in shape. Brown-light brown capsules belong to *V. sinuatum* subsp. *sinuatum* var. *adenosepalum*, while light brown capsules belong to *V. sinuatum* subsp. *sinuatum* var. *sinuatum*. Stellate and glandular hairs cover *V. sinuatum* subsp. *sinuatum* var. *adenosepalum*, whereas densely stellate and glandular hairs cover *V. sinuatum* subsp. *sinuatum* var. *sinuatum* (Table 5, Figure 7).

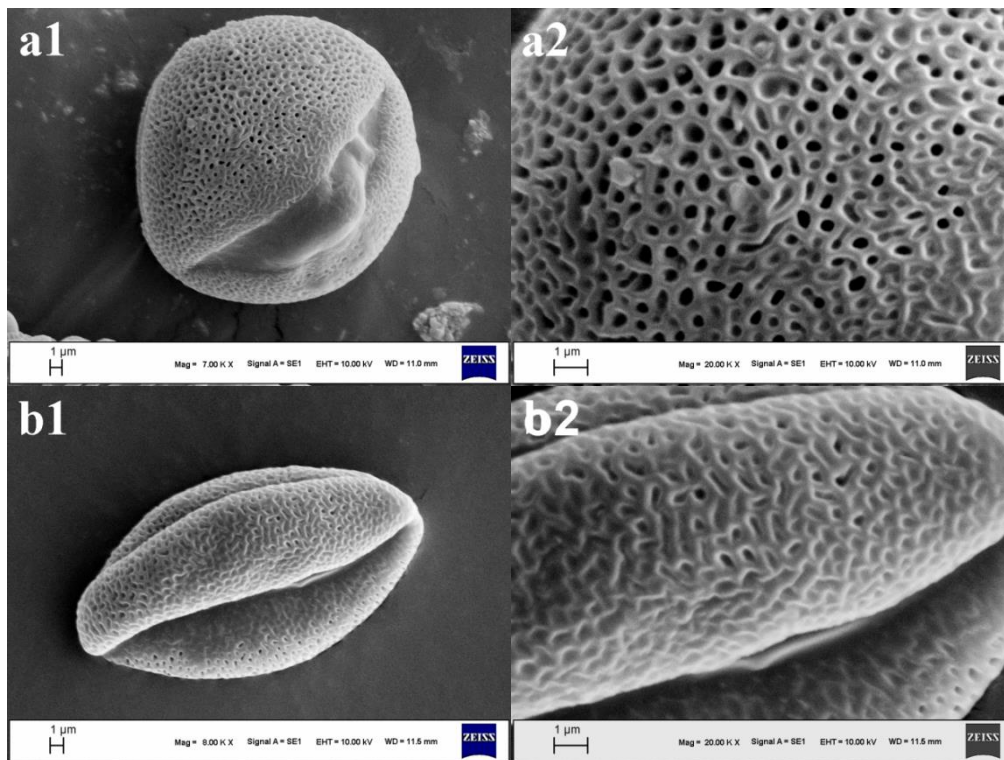


**Figure 5.** Pollen photographs of *Verbascum* varieties (SEM). 1- Equatorial view, 2- Exine sculpturing. (a1-a2) *V. sinuatum* subsp. *sinuatum* var. *adenosepalum*, (b1-b2) *V. sinuatum* subsp. *sinuatum* var. *sinuatum*.

**Table 3.** Pollen morphological characters of *Verbascum* varieties ( $\mu\text{m}$ ) (min (mean) max).

Species	P	E	P/E	Shape	Clg	Clt	Plg	Plt	Ex	In	Apt	Or
<i>V. sinuatum</i> subsp. <i>sinuatum</i> var. <i>adenosepalum</i>	11.68 (14.25)	12.39 (13.97)	1.02	Prolate-spheroidal	9.24 (11.73)	2.31 (3.22)	3.30 (4.86)	2.49 (3.84)	0.59 (0.88)	0.32 (0.52)	93 % Tricolporate	Reticulate
<i>V. sinuatum</i> subsp. <i>sinuatum</i> var. <i>sinuatum</i>	16.61	18.11			14.78	4.61	6.31	5.59	1.23	0.83	7 % Tricolporate	
<i>V. sinuatum</i> subsp. <i>sinuatum</i> var. <i>sinuatum</i>	10.18 (11.38)	4.41 (7.12)	1.59	Prolate	7.58 (8.85)	1.74 (2.59)	2.15 (2.61)	1.19 (1.74)	0.44 (0.63)	0.20 (0.43)	17 % Tricolporate	Reticulate
<i>V. sinuatum</i> subsp. <i>sinuatum</i> var. <i>sinuatum</i>	13.46	9.46			10.83	3.76	3.55	2.25	0.88	0.54	83 % Tricolporate	

**Table 4.** Seed morphological characters in varieties of *Verbascum* (mm) (min (mean) max).

Species	Group <sup>a</sup>	Length	Width	Color	Shape	Seed surface
<i>V. sinuatum</i> subsp. <i>sinuatum</i> var. <i>adenosepalum</i>	H	0.57 (0.87) 1.08	0.32 (0.52) 0.68	Brown	Prismatic-oblong, deep and broad back, broad beaks	alveolate, broad Irregular, polygonal and rectangular cells with densely and distinct vesicles. Inside the cells are 3-6 transverse lines
<i>V. sinuatum</i> subsp. <i>sinuatum</i> var. <i>sinuatum</i>	H	0.61 (0.83) 1.11	0.31 (0.52) 0.68	Brown	Prismatic-oblong, shallow alveolate, deep and broad back, broad beaks	± ovate, Irregular, polygonal and long rectangular cells with densely and distinct vesicles. Inside the cells are 4-8 transverse lines

**Table 5.** Capsules morphological characters -of *Verbascum* varieties (mm).

Species	Group <sup>a</sup>	Length	Width	Color	Shape	Hair
<i>V. sinuatum</i> subsp. <i>sinuatum</i> var. <i>adenosepalum</i>	H	3.33 (3.97) 4.75	2.98 (3.06) 3.46	Brown-light brown	Ovate, oblong	Stellate, glandular
<i>V. sinuatum</i> subsp. <i>sinuatum</i> var. <i>sinuatum</i>	H	1.76 (2.14) 2.52	2.11 (2.16) 2.21	Light brown	Spheroidal, ovate	Densely stellate, glandular

<sup>a</sup> According to Huber-Morath (1978)

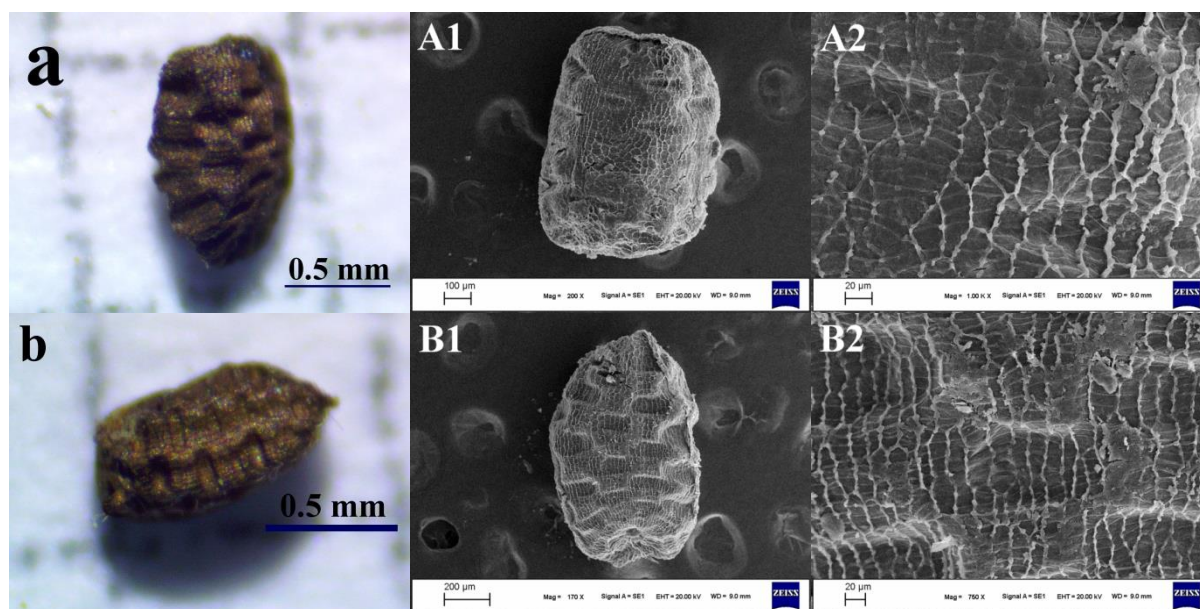


**Figure 6.** Seed micrographs of *Verbascum* varieties (SEM). a: *V. sinuatum* subsp. *sinuatum* var. *adenosepalum*, b: *V. sinuatum* subsp. *sinuatum* var. *sinuatum*, 1- General appearance, 2- Surface ornamentation. (A1-A2) *V. sinuatum* subsp. *sinuatum* var. *adenosepalum*, (B1-B2) *V. sinuatum* subsp. *sinuatum* var. *sinuatum*.

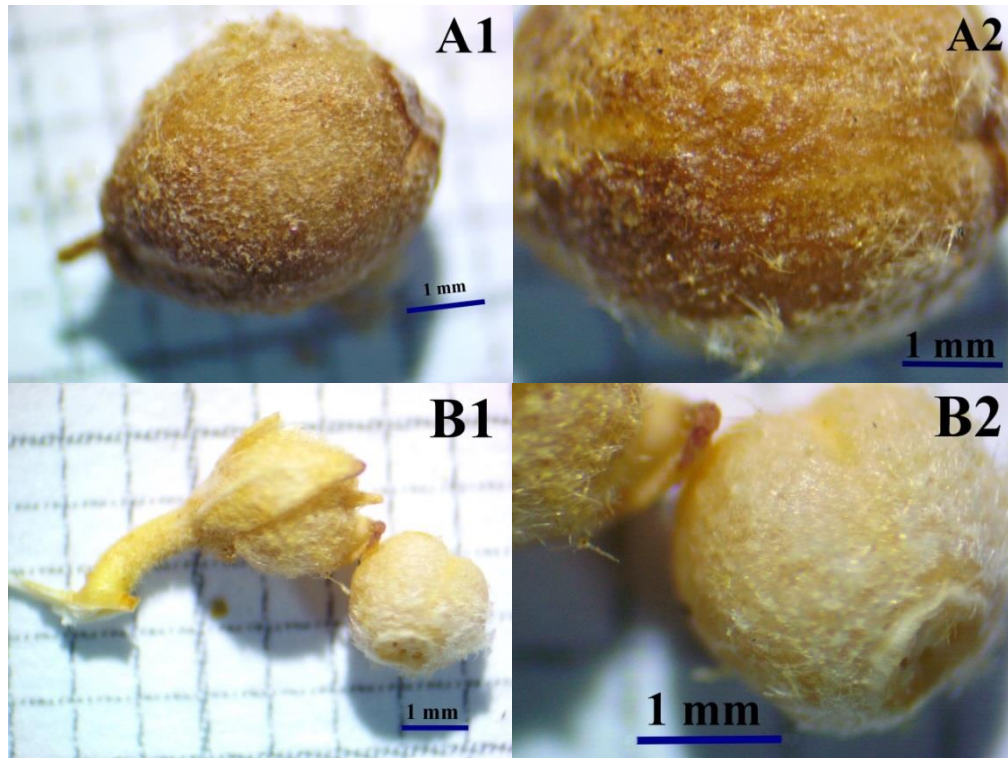


**Figure 7.** Capsule photographs of *Verbascum* varieties (Stereo microscopy). 1- General appearance, 2- Close view. (A1-A2) *V. sinuatum* subsp. *sinuatum* var. *adenosepalum*, (B1-B2) *V. sinuatum* subsp. *sinuatum* var. *sinuatum*.

#### 4. Conclusion

In this study, the anatomy, pollen and seed analyzes of *Verbascum sinuatum* subsp. *sinuatum* var. *adenosepalum* and *V. sinuatum* subsp. *sinuatum* var. *sinuatum* varieties distributed in the Southeastern Anatolia Region were examined for the first time, ensuring that they are comparable to other *Verbascum* members examined.

A very large xylem area at the root and a thick cuticle layer on the stem were observed in both varieties. Moreover, prior research [12-15, 19-22] have found similar characteristics. The cambium in the vascular bundle of the root was reported to be indeterminate in several studies [13], yet this study indicated that the root exhibited similar features for the varieties. Cross-sectional studies of the leaf's epidermal cells revealed densely glandular, eglandular, and branching multicellular hairs. Comparable outcomes have been documented for several *Verbascum* species under investigation [13]. Identification within the genus *Verbascum* may be aided by the presence of idioblasts in the leaf's mesophyll tissue [29]. Idioblasts were found in the leaf mesophyll in this study, and other studies have also reported this trait [20].

Anatomical research in vascular plants are primarily conducted on the stem since it is less subject to environmental variables [30]. This information is

supported by the stem anatomy of these types, which displays unique characteristics.

The two *Verbascum* varieties examined in this study are similar to some of the other *Verbascum* members examined based on analyses of their pollen, seeds, and capsules.

The exine of two *Verbascum* types has a tectate structure and reticulate ornamentation, and the pollen is isopolar, radially symmetric, prolate-spheroidal, prolate, and tricolporate (there is tricolpate). The pollen grain was identified as tricolpate by Aktas et al. [13] in their investigation of the endemic *Verbascum* species. Aktas [12] observed in his study on *Verbascum* species that the pollen grain was tricolpate. Öztürk et al. [7] found that *Verbascum bithynicum* (H group) tricolporate and tricolpate aperture types in their pollen analysis. According to Al-Hadeethy et al. [10], *Verbascum* species (20 species) had tricolporate aperture types. In their investigation, Tricolporate aperture type is the reported aperture type of *Verbascum* [9]. Two varieties under investigation have prolate-spheroidal and prolate shaped pollen. However, the prolate pollen morphology in the endemic *Verbascum* species under investigation was noted by Aktas et al. [13]. According to Aktas [12], the species he studied exhibits subprolate pollen shapes. According to Öztürk et al. [7], the species under investigation had prolate- and oblate-spheroidal pollen morphologies. According to Asmat et al. [9], *V. thapsus* pollen grains were oblate-spheroidal. Furthermore, Al-

Hadeethy et al. [10] noted that *Verbascum* (20 species) included both oblate and prolate-spheroidal pollen. According to Al-Hadeethy et al. [10], there was minimal taxonomic significance for this trait because the taxa under study had similarities in exine thickness. The current study's findings are consistent with earlier research on a few *Verbascum* species [7, 9-10, 13]. All of the taxa in our research, however, displayed a consistent reticulate exine sculpturing pattern.

When fully grown, the seeds were brown. There were differences in the seed shapes of the varieties under study. The size of the seed usually ranged between 0.57 to 1.11 mm in length and 0.31 to 0.68 mm in wide. The experimental variation design in size was limited among the species, despite Attar et al. [28] showing that the size of the seed displayed variability among the various populations of the same species, even among seeds in the same capsule. The current study's measurements agreed with those of the common species found in Cabi et al.'s [17] investigations. However, the measurements in this study were more than those of the species that were frequently studied in the studies by Attar et al. [28] and Kheiri et al. [16]. The longest seeds in this study were found in *V. sinuatum* subsp. *sinuatum* var. *sinuatum*, while the shortest seeds were found in *V. sinuatum* subsp. *sinuatum* var. *adenosepalum*. Within the genus *Verbascum*, there is enough variation in seed form to distinguish between species and subtaxa within the species.

The importance of a few traits in the *Verbascum* variety delimitation has been investigated in this study. The systematics of the genus can benefit from the use of certain pollen and seed traits, which are typically connected to pollen and seed micromorphological and anatomical patterns. These ancestral characters can also support the infrageneric categorization. This study examines the systematic significance of certain morphological, anatomical, and pollen characteristics of the genus *Verbascum*. More comprehensive research involving all genus taxa will be beneficial in elucidating the systematic issues facing the genus *Verbascum*.

**Acknowledgements** We wish to thank Scientific Investigation Project to Coordinate of Mardin Artuklu University (Project No. MAÜ.BAP.22.KMY.011) for financial support.

**Author contributions** MK and FMK conducted the field work. MK conducted anatomical analysis. MK and FMK wrote and gave comments to the manuscript. Authors read and approved the final version of the manuscript.

**Compliance with Ethical Standards**

**Conflict of Interest** The authors declare that they have no conflict of interest.

**Research involving Human Participants and/or Animals** Not applicable.

**Informed consent** Not applicable.

## References

- [1]. Mabberley, DJ. 2008. Mabberley's plant book: a portable dictionary of plants, their classifications and uses. Cambridge Univ. Press.
- [2]. Murbeck, S. 1939. Weitere Studien über die Gattungen *Verbascum* und *Celsia*. *Acta Universitatis Lundensis*; 2: 1-70.
- [3]. Huber-Morath, A. 1978. *Verbascum* L. In: Davis, P. H. (ed.), *Flora of Turkey and the East Aegean Islands*. Edinburgh University Press, Edinburgh, England, Vol. 6, pp. 461-603.
- [4]. Davis, PH, Mill, RR, Tan, K. 1988. *Flora of Turkey and the East Aegean Islands (Suppl. 1)*. Edinburgh University Press, Edinburgh, England, Vol. 10, pp. 191-193.
- [5]. Karaveliogulları, FA. 2012. *Verbascum* L. In: Güner, A. et al. (eds), *Türkiye Bitkileri Listesi (Damarlı Bitkiler)*. Nezahat Gökyiğit Botanik Bahçesi ve Flora Araştırmaları Derneği Yayını, İstanbul, pp. 850-870.
- [6]. Firat, M. 2022. *Verbascum zerdust (Scrophulariaceae)*, a new species from Bitlis province (Turkey) belonging to section *Bothrosperma*. *Nordic Journal of Botany*. doi: 10.1111/njb.03649
- [7]. Öztürk, A, Güney, KB, Bani, B, Güney, K, Karaveliogulları, FA, Pinar, NM, Çeter, T. 2018. Pollen morphology of some *Verbascum (Scrophulariaceae)* taxa in Turkey. *Phytotaxa*; 333(2): 209-218. <https://doi.org/10.11646/phytotaxa.333.2.4>
- [8]. Juan, R, Fernandez, I, Pastor, J. 1997. Systematic consideration of microcharacters of fruits and seeds in the genus *Verbascum (Scrophulariaceae)*. *Annals of Botany*; 80: 591-598. <https://doi.org/10.1006/anbo.1997.0472>
- [9]. Asmat, T, Khan, MA, Ahmed M, Zafar, M, Manzoor, F, Munir, M, Akhtar, K, Bashir, S, et. al. 2011. Pollen morphology of selected species of *Scrophulariaceae* of District Dir Upper, Pakistan. *Journal of Medicinal Plants Research*; 5: 6423-6428. <https://doi.org/10.5897/JMPR11.723>
- [10]. Al-Hadeethy, M, Al-Mashhadani, A, Al-Khesraji, T, Barusrux, S, Al-Jewari, H, Theerakulpisut, P, Pornpongrungrueng, P. 2014. Pollen morphology of *Verbascum* L. (*Scrophulariaceae*) in Northern and Central Iraq. *Bangladesh Journal of Plant Taxonomy*; 21: 159-165. <https://doi.org/10.3329/bjpt.v21i2.21355>
- [11]. Karaveliogulları, FA, Yüce, E, Başer, B. 2014. *Verbascum duzgunabadagensis (Scrophulariaceae)*, a new species from eastern Anatolia, Turkey. *Phytotaxa*; 181: 47-53.
- [12]. Aktas, K. 2019. Morphology, Anatomy, Palynology and Seed Micromorphology of Turkish Endemic *Verbascum X splendidum* Boiss. (*Scrophulariaceae*). *Fresenius Environmental Bulletin*; 28(12): 10004-10010.
- [13]. Aktas, K., Özdemir, C. & Özdemir, B. 2020: Morphology, Anatomy, Palynology and Seed Micromorphology of Turkish Endemic *Verbascum exuberans* Hub.-Mor. (*Scrophulariaceae*). *Planta Daninha*. v38:e020191125
- [14]. Kılıç, M. 2023. Anatomy, Pollen and Seed Morphology of Endemic Species *Verbascum globiferum* Hub.-Mor. and *V. lysiosepalum* Hub.-Mor. (*Scrophulariaceae*) In Diyarbakır, Turkey and Their Taxonomic Importance. *Bangladesh Journal of Plant Taxonomy*; 30(2): 201-212. <https://doi.org/10.3329/bjpt.v30i2.70497>

- [15]. Mungankılıç, F, Kılıç, M. 2024. Anatomy, palynology and seed micromorphology of Turkish rare *Verbascum racemiferum* Boiss. & Hausskn Ex Boiss. (Scrophulariaceae). *Biological Diversity and Conservation*; 17(1): 63-71. <https://doi.org/10.46309/biodicon.2023.1367629>
- [16]. Kheiri, S, Khayami, M, Mahmoudzadeh, A. 2009. Micromorphological and anatomical studies of certain species of *Verbascum* (Scrophulariaceae) in West Azerbaijan, Iran. *Iran Journal of Botany*; 15: 105-13.
- [17]. Cabi, E, Baser, B, Yavru, A, Polat, F, Toprak, U, Karaveliogullari, FA. 2011. Scanning electron microscope (SEM) and Light microscope (LM) studies on the seed morphology of *Verbascum* taxa (Scrophulariaceae) and their systematic implications. *Australian Journal of Crop Science*; 5: 660-667.
- [18]. Duman, H, Uzunhisarcikli, ME, Tan, K. 2017. *Verbascum mughlaeum* (Scrophulariaceae), a new species from SW Anatolia, Turkey. *Phytotaxa*; 291: 231-6.
- [19]. Özdemir, C, Altan, Y. 2007. Some morphological and anatomical properties of endemic *Verbascum oreophilum* C. Koch var. *oreophilum* (Scrophulariaceae). *Afyon Kocatepe Univ J Sci*; 7: 429-437.
- [20]. Tekin, M, Yılmaz, G. 2018. Anatomical and Palynological Studies on Endemic *Verbascum weidemannianum* Fisch. & Mey. (Scrophulariaceae) In Turkey. *International Journal of Agriculture, Forestry and Life Science*; 2(2): 6-15.
- [21]. Küçük, S, Elmaskaya, A, Göktürk, RS. 2021. Endemic *Verbascum deterrentum* Boiss. & Heldr.'s (Scrophulariaceae) Anatomical Features. *Biological Diversity and Conservation*; 14(3): 390-395. doi: 10.46309/biodicon.2020.863066.
- [22]. Mungankılıç, F, Kılıç, M. 2023. Anatomical studies on endemic *Verbascum stepporum* Murb., and *Verbascum tenue* Hub.-Mor., (Scrophulariaceae) species distributed in Şanlıurfa. *Biological Diversity and Conservation*; 165(2): 132-139.
- [23]. Bozdağ, B, Kocabaş, O, Akyol, Y, Özdemir, C. 2016. A New Staining Method for Hand-Cut in Plant Anatomy Studies. *Marmara Pharmaceutical Journal*; 20: 184-190.
- [24]. Metcalfe, CR, Chalk, L. 1950. Anatomy of Dicotyledons. Clarendon Press, Oxford, 1st edition, Vol. 2.
- [25]. Erdtman, G. 1952. Pollen Morphology and Plant Taxonomy: Angiosperms. Massachusetts, USA. Chronica Botanica Co., pp. 1-553.
- [26]. Wodehouse, RP. 1935. Pollen Grains, their structure, identification and significance in science and medicine. Hafner Publishing Company, New York.
- [27]. Punt, W, Hoen, PP, Blackmore, S, Nilsson, S, Le-Thomas, A. 2007. Glossary of pollen and spore terminology. *Review of Palaeobotany and Palynology*; 143: 1-81.
- [28]. Attar, F, Keshvari, A, Ghahreman, A, Zarre, S, Aghabeigi, F. 2007. Micromorphological studies on *Verbascum* (Scrophulariaceae) in Iran with emphasis on seed surface, capsule ornamentation and trichomes. *Flora*; 202: 169-175. <https://doi.org/10.1016/j.flora.2006.04.001>
- [29]. Lersten, N.R., & Curtis, J.D. 2001. Idioblasts and other unusual internal foliar secretory structures in Scrophulariaceae. *Plant Systematics and Evolution*; 227: 63-73.
- [30]. Lopes, LKC, Góes-Neto, LAA, Feio, AC. 2020. Stem anatomy and its relevance for the Taxonomic survey of *Selaginella* subg. *Gymnogynum* (Selaginellaceae). *Plant Systematics and Evolution*; 306: 13. doi:10.1007/s00606-020-01655-x

# Rhodamine B Hazardous Dye Removal via Adsorption Using Hg(II) Coordination Polymer

Afranur PENDAR<sup>1</sup> , Derya DAVARCI<sup>1\*</sup> 

<sup>1</sup> Department of Chemistry, Gebze Technical University, 41400, Gebze, Kocaeli, Türkiye

\*[ddavarci@gtu.edu.tr](mailto:ddavarci@gtu.edu.tr)

\* Orcid No: 0000-0002-0407-9604

Received: 3 January 2024

Accepted: 26 March 2024

DOI: 10.18466/cbayarfbe.1413938

## Abstract

Herein, we have reported the Hg(II) coordination polymer, (Hg-CP), formulated  $\{[\text{Hg}(\text{L})](\text{Cl}_2)(\text{CH}_3\text{CN})_2\}_n$ , behaved as adsorbent against Rhodamine B dye stuff. UV-Vis absorption spectroscopy was used to conduct dye adsorption investigations on coordination polymers. Adsorption experiments were carried out in acidic (pH=3) and neutral (pH=6) media and the results showed that the compound removed the cationic Rhodamine B from water. In acidic media, the adsorption capacity of the Hg-CP was more than neutral media. Also, Hg-CP could selectively adsorb Rhodamine B dye from the Rhodamine B/Methyl orange dye mixture. The colour of the Hg-CP was white before adsorption, whereas it changed after adsorption as Rhodamine B adhered to the surface of Hg-CP.

**Keywords:** Coordination polymers, cyclotriphosphazene, benzimidazole, dye adsorption, Rhodamine B.

## 1. Introduction

In recent years, studies on coordination polymers have been very popular because they can be synthesized with metal salts in a short time. At the same time, the fact that coordination polymers have many application areas such as gas storage, magnetism, sensing, luminescence, catalysis, and dye adsorption increases their importance [1-6]. Especially studies on dye adsorption using coordination polymers have attracted attention day by day because organic dyestuffs cause considerable impurities when involved in water resources [7,8]. Rhodamine B (RhB) dye is one of the synthetic aromatic dyes, and it is extensively utilised as a colouring agent in the production of food and textile products (Figure 1). RhB poses hazardous environmental and health risks. It has been proven that if a source of water is contaminated with even small amounts of RhB, it can cause subcutaneous tissue-derived sarcomas, which are highly carcinogenic [9]. Therefore, it is very important to remove RhB from the wastewater.

Cyclotriphosphazenes are important inorganic heterocyclic compounds that are composed of phosphorus and nitrogen atoms. They easily undergo nucleophilic substitution reactions because they contain an active six P-Cl bond.

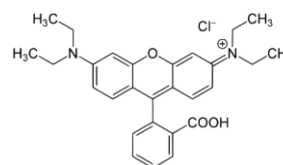
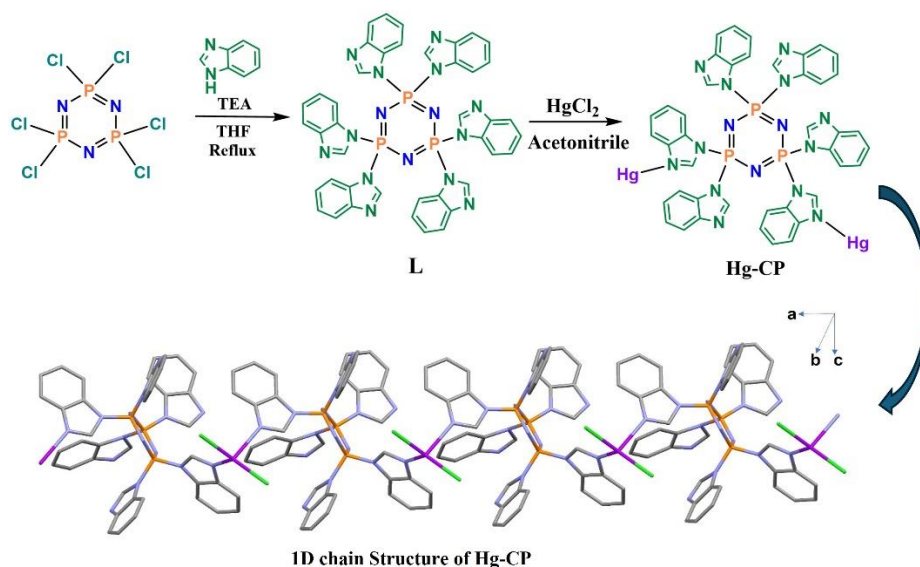


**Figure 1.** Structure of RhB dye.

There has been a discernible surge in research on coordination polymers based on cyclotriphosphazene in the last several years. The cyclotriphosphazene derivatives, which have six arms bearing donor N atoms, act as multidentate ligands, which allow the formation of 2- and 3-dimensional coordination polymers [10,11-16]. Owing to the d10 configuration of the group 12 metal, which provides flexible coordination geometries, coordination polymer studies with these metals have attracted important attention [17]. The formation of Hg(II) complexes is rare compared to other group 12 metal complexes. Dye adsorption studies with cyclophosphazene polymers and composites are available in the literature [14,15,18-22]. However, when the literature is examined, the number of studies on the dye adsorption of cyclotriphosphazene-based coordination polymers is quite limited [14,15]. A study was conducted wherein a completely 2-methylimidazole-substituted cyclotriphosphazene ligand was used to create 2D and 3D Ag (I) coordination polymers.

Adsorption experiments showed that  $\{[Ag_3(MeIm-Cp)_2](NO_3)_3\}_n$ , which is a 3D coordination polymer, removed the anionic methyl orange (MO) and tartrazine (E102) from water but showed no adsorption behaviour against the cationic methylene blue (MB) [14]. In our previous study, cyclotriphosphazene ligand that was fully substituted with benzimidazole (**L**) was synthesised as a starting material and prepared into two coordination polymer, namely  $\{[Ag(L)](CH_3PhSO_3)](CH_3CN)_4\}_n$  and  $\{[Hg(L)](Cl_2)](CH_3CN)_2\}_n$ . While both coordination polymers did not show adsorption against anionic MO and E102, they showed adsorption against cationic MB dye [15]. Some adsorption experiment results from the literature are given in part of results and discussion.

In this work, we synthesised **Hg-CP**,  $\{[Hg(L)](Cl_2)](CH_3CN)_2\}_n$ , according to literature [15] (Scheme 1) and investigated the adsorption ability against cationic RhB dye. Furthermore, we examined whether the compound selectively adsorbs RhB from the RhB/MO (cationic/anionic dye mixture). The results clearly demonstrated that **Hg-CP** easily adsorbed RhB from the aqueous solution and dye mixture, especially in acidic media.



Scheme 1. Synthetic pathways and structure of Hg-CP.

## 2. Materials and Methods

Hexachlorocyclotriphosphazene and benzimidazole (99%) was obtained from Aldrich.  $HgCl_2$  was purchased from Merck. Acetonitrile ( $\geq 99.0\%$ ) was bought from Merck. Adsorption studies were performed by Shimadzu 1900i UV-Vis. spectrometer. Zeta potential analyser (Malvern-Zetasizer nano ZS) was used to analyse the surface charges of samples. PXRD analyses were performed at room temperature up to resolution of  $2\theta = 2.0-50^\circ$  on a Rigaku X-ray diffractometer D-Max Rint 2200 Series instrument using  $Cu K\alpha$  radiation at 40 kV and 40mA.

### 2.1. Dye adsorption studies

Synthetic dye manufacturing is rising steadily alongside the everyday increase in its application in industry. An enormous ecological risk arises when wastewater and these dangerous pigments are mixed. For this reason, there is an increasing amount of research focused on the removal of dyes from wastewater through the adsorption method.

The adsorption behaviour of **Hg-CP** against RhB was investigated in batch experiments. First, the UV absorbency of the standard RhB and MO solutions at various known concentrations was tested to create a working curve, and then calibration graphics were achieved with a correlation coefficient (R) higher than 0.999. RhB solutions at a concentration 10 mg/L in distilled water were prepared as a standard stock solution. 10 mg of the **Hg-CP** were immersed in a 25 mL aqueous dye solution. For acidic conditions, a 0.6 M HCl solution was added to aqueous dye solutions until the pH value was 3.

Afterwards, to prepare the RhB+MO dye mixture, 25 ml of RhB dye solution, and 25 ml of MO dye solution were taken from stock solutions and mixed together. Subsequently, 20 mg of coordination polymer was added to this mixture. For pH 3 media, a 0.6 M HCl solution was added to the dye mixture. Dye solutions containing **Hg-CP** were monitored at different time intervals using UV-visible spectroscopy and measured in the 300-800 nm wavelength range.

The adsorption capacity ( $q_e$ ) and the percentage of removal efficiency (R%) of **Hg-CP** were calculated using the following equations:

$$q_e = \left( \frac{C_0 - C_e}{m} \right) \times V \quad (1)$$

$$R\% = \left( \frac{C_0 - C_e}{C_0} \right) \times 100 \quad (2)$$

$C_0$  is the first concentration of dye (mg/L) and  $C_e$  is the amount of dye still present in the solution following adsorption (mg/L).  $V$  is the volume of solution (L),  $m$  is the mass of adsorbent used (g).

### 3. Results and Discussion

The acquired spectra from UV-visible spectroscopy were compared to the absorption bands of the pure dye solutions at 464 nm (MO) and 554 nm (RhB) wavelengths [23]. The natural pH of RhB aqua solution containing **Hg-CP** is 6. The UV graphic obtained from the adsorption study performed on this media can be seen in Figure 2a. **Hg-CP** exhibited dye removal behaviour towards RhB from water in neutral media (pH=6). In the adsorption study, after adjusting the

pH to 3, it was observed that the colour of the dye solution became entirely clear, indicating an increased amount of RhB adsorbed (Figure 2b). The measurements clearly indicate that **Hg-CP** adsorbed the RhB from water with saturated adsorption amounts of 4.89 mg/g (pH 6) and 18.14 mg/g (pH 3) through complicated adsorption processes (Figures 2c and 2d).

We studied the kinetics of RhB adsorption of **Hg-CP**. Due to showing good linearity and a coefficient  $R^2$  value closer to 1, the pseudo second order and pseudo-first-order kinetics model is more suitable for pH 6 and pH 3 media, respectively (Table1). This result revealed that chemical interactions were slightly more dominant in the pH=6 medium, but when pH was lowered to 3, physical interactions became more dominant because of the significant change in surface charges.

**The pseudo-first order rate equation:**

$$\log(q_e - q_t) = \log(q_e) - \frac{k_1}{2.303} t \quad (3)$$

**The pseudo-second order rate equation:**

$$\frac{t}{q_t} = \frac{1}{k_2 q_e^2} + \frac{t}{q_e} \quad (4)$$

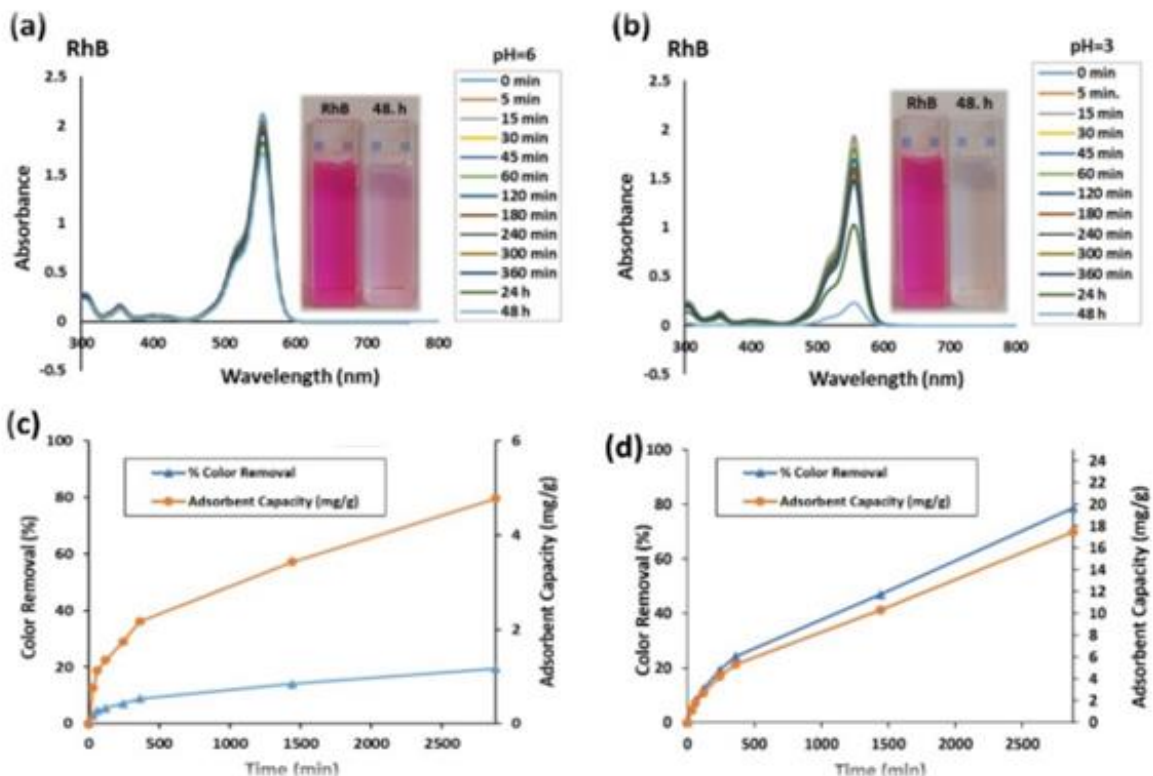
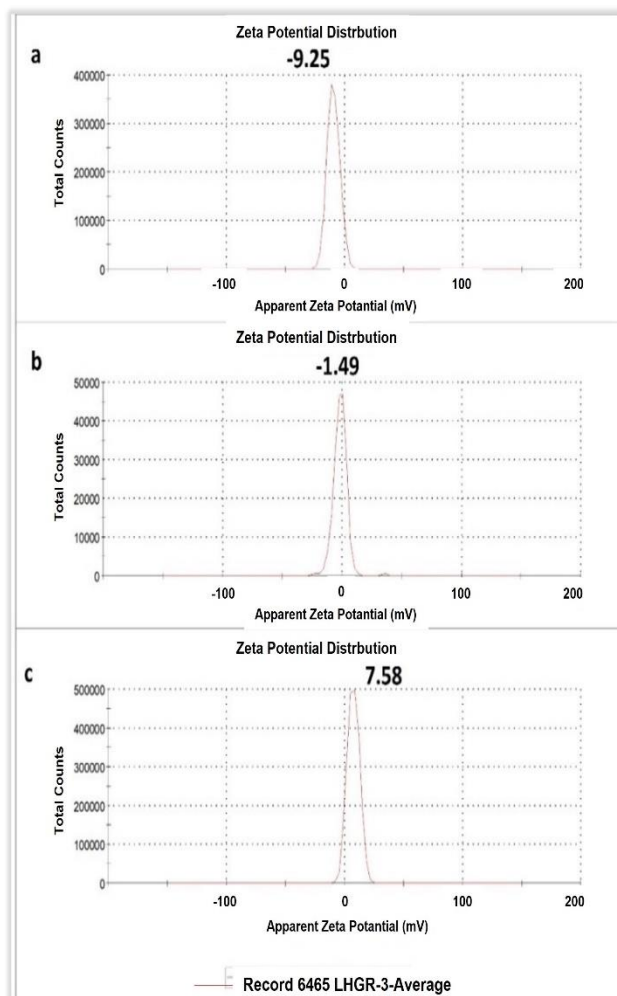


**Figure 2.** Time-dependent UV-Vis spectra of the aqueous solution of RhB treated by at pH=6 (a), pH=3 (b) and time-dependence of adsorption profiles of RhB over at pH 6 (c) and pH=3 (d).

**Table 1.** Kinetic parameters of RhB adsorption of **Hg-CP** at pH 6 and pH 3.

pH	Pseudo-first order model			Pseudo-second order model		
	$k_1$	$q_e$	$R^2$	$k_2$	$q_e$	$R^2$
6	0.0006909000	3.937313537	0.93	0.00072465	4.894762604	0.956
3	0.0004606000	18.14261982	0.94	0.000061871	21.36752137	0.841

Here,  $q_e$  is the quantity of material adsorbed per unit of adsorbent at equilibrium (mg/g),  $q_t$  is the amount of substance adsorbed per unit adsorbent at any given moment (mg/g),  $t$  is the adsorption time (min),  $k_1$  is the rate constant of the pseudo first order model ( $\text{min}^{-1}$ ),  $k_2$  is the rate constant of the pseudo second order model ( $\text{g mg}^{-1} \text{min}^{-1}$ ). The surface charge measurement for **Hg-CP** was carried out in deionized water, and the surface charge was found to be negative (approximately -9.25 mV) at pH=6 (Figure 3a). Because of the negative surface charge's tendency to reject anionic dyes and adsorb cationic dyes through electrostatic interaction, the surface charge was crucial for adsorption and separation processes.



The surface value of **Hg-CP** after RhB adsorption in pH = 6 media is -1.49 mV (Figure 3b). As RhB, a cationic dye, was adsorbed on the surface, the surface charge was affected positively. In the adsorption experiment conducted in a medium with pH = 3, the surface charge was observed to shift to a positive value (7.58 mV) (Figure 3c) which indicates that the amount of cationic RhB adsorbed on the surface increases. This can be seen from the UV graphics in Figure 2b and the color change in the bathtub pictures.

In the study, it was also investigated whether **Hg-CP** selectively adsorbs RhB dye from the RhB/MO (1:1) mixture or not. For this purpose, firstly, the adsorption of the compound against MO dyestuff was examined. We have shown in our previous study that this compound does not adsorb MO dye in a neutral environment. Therefore, we only examined the situation in an acidic environment and checked its adsorption in pH 3 media. It can be seen that **Hg-CP** did not exhibit any adsorption behaviour against MO in acidic media (Figure 4). Namely, in the adsorption experiment for MO, it was determined that **Hg-CP** did not adsorb the dye in either pH = 6 or pH = 3 media.

Therefore, we only examined the situation in an acidic environment and checked its adsorption in pH 3 media. It can be seen that **Hg-CP** did not exhibit any adsorption behaviour against MO in acidic media (Figure 4). Namely, in the adsorption experiment for MO, it was determined that **Hg-CP** did not adsorb the dye in either pH = 6 or pH = 3 media.

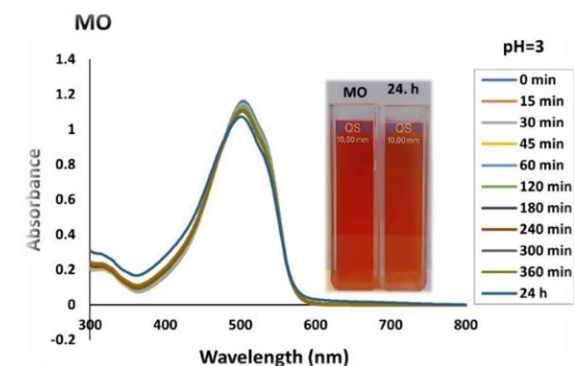


**Figure 4.** UV-Vis absorption spectra of the aqueous solution of MO treated by **Hg-CP** with time dependence at pH=3.

When the UV-Vis graph in Figure 5a is examined, it is seen that **Hg-CP** selectively adsorbs RhB from the RhB/MO mixture. **Hg-CP** adsorbed the RhB from water with a saturated adsorption amount of 15.45 mg/g at pH 3 (Figure 5b).

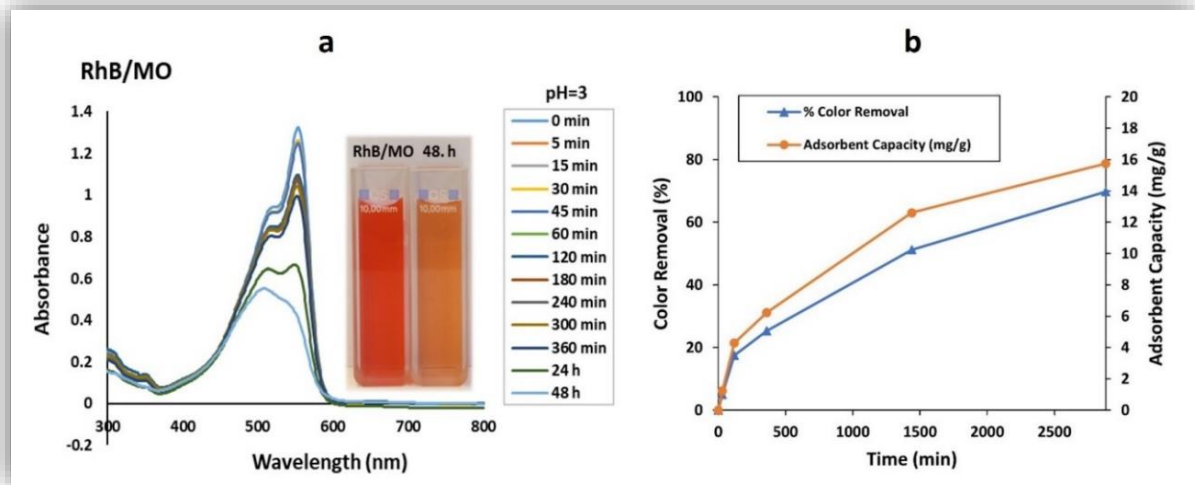


**Figure 5.** a) Time-dependent UV-Vis absorption spectra of the aqueous solution of RhB/MO treated by **Hg-CP** at pH=3. b) Time-dependence of adsorption profiles of RhB/MO over **Hg-CP** at pH 3.

**Table 2.** Kinetic parameters of RhB/MO adsorption of **Hg-CP** at pH 3.

Pseudo-first order model			Pseudo-second order model		
$k_1$	$q_e$	$R^2$	$k_2$	$q_e$	$R^2$
0.0009212000	15.4525444	0.9643	0.000115705	18.72659176	0.9312

According to kinetic studies on the adsorption of dye mixtures, the adsorption model is compatible with the pseudo-first-order model (Table 2).

The images of the before and after adsorption are given in Figure 6. As an indicator of adsorption, **Hg-CP** that was white before the adsorption process turned the colour of RhB after adsorption. When examined carefully, it can be seen with the naked eye that, after adsorption, the colour appearing at pH = 3 is darker than pH = 6.

The stability of the adsorbent is important for adsorption studies. The diffractogram of **Hg-CP** gained by the PXRD technique before dye adsorption studies was compared with the diffractograms obtained after RhB adsorption in pH 3 media. It is seen that the peaks are largely matched, and it was observed that the structure of **Hg-CP** remained intact after adsorption in an acidic environment. Likewise, there was also no change in the PXRD pattern after the adsorption of RhB dye from the RhB/MO mixture. As a result, the coordination polymer maintained its first structure before adsorption, and its structure did not change (Figure 7).

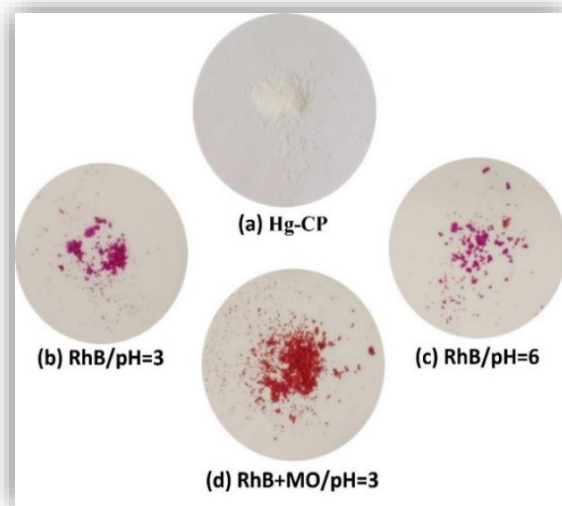


**Figure 6.** For **Hg-CP** (a) before adsorption, (b) after RhB adsorption at pH=3, (c) after RhB adsorption at pH=6, (d) after RhB+MO adsorption at pH=6.

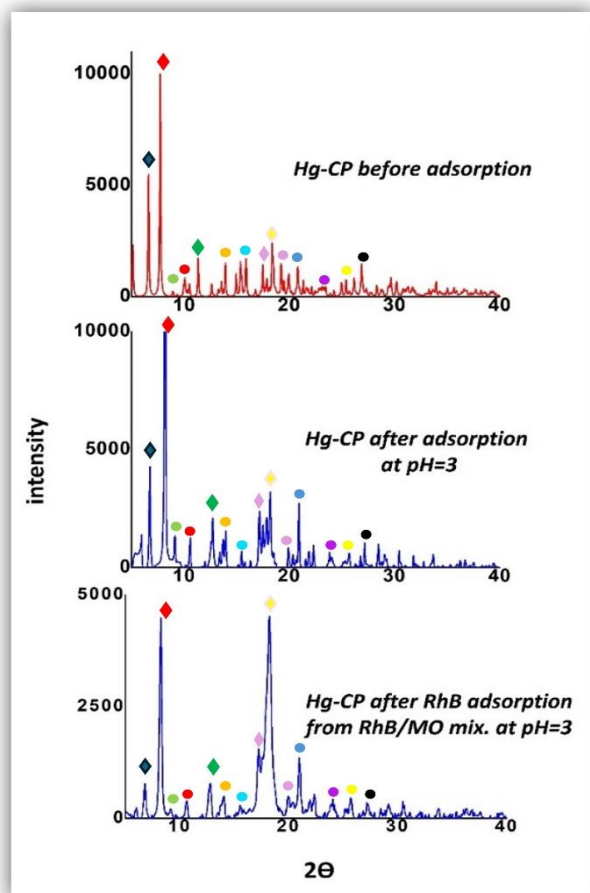


**Figure 7.** Matched-PXRD diffractogram of **Hg-CP** before and after adsorption.

The surface morphologies of the adsorbent before and after adsorption were also investigated and shown in Fig. 8. When comparing the SEM images of **Hg-CP** before and after adsorption (Figs. 8a and 8b), it is seen that the morphology of the surface of the complexes changed. The analyses support dye stuff adsorbed on the surfaces of the **Hg-CP**.

When the literature is reviewed, studies on dye adsorption are generally carried out with cyclotriphosphazenes or polyphosphazene composites. Most of these studies are about MB dye adsorption. There are a few studies on cyclophosphazene-based coordination polymers. A comparison of the MB dye adsorption capacities of some cyclophosphazene derivatives in the literature is given in Table 3. Considering the results of the studies, it can be seen that the dye adsorption capacities of the materials prepared as composites are better. In addition, the dye adsorption capacities of the coordination polymers synthesised by our group, which are lined 5th and 6th in table 3, are also promising.

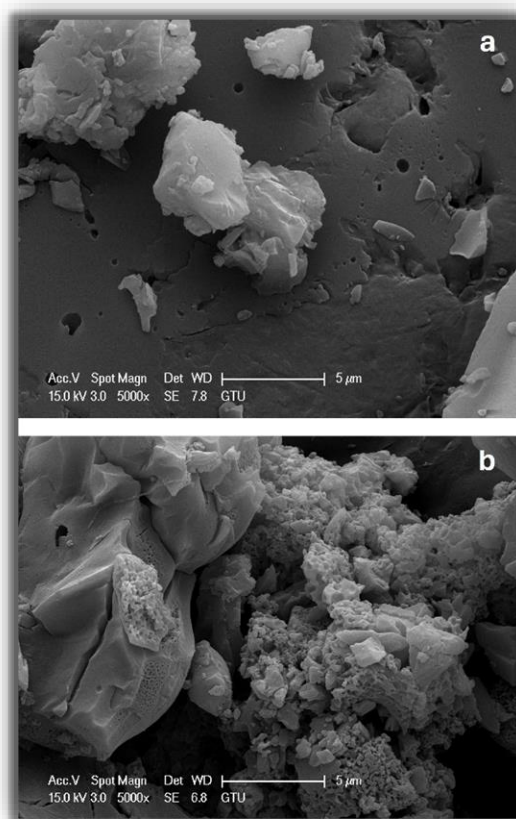


**Figure 8.** SEM image of **Hg-CP** before (a) and after (b) adsorption.

**Table 3.** MB dye adsorption capacities of some cyclophosphazene derivatives.

Compounds	MB	
	Max. adsorption capacities (mg/g)	Ref.
HCP-TPP	504	[18]
PCS-OP-3	151	[19]
PZD	96	[20]
(PZS)	20	[21]
$\{[\text{Ag}(\text{L})](\text{CH}_3\text{PhSO}_3)(\text{CH}_3\text{CN})_4\}_n$	18	[15]
$\{[\text{Hg}(\text{L})](\text{Cl}_2)(\text{CH}_3\text{CN})_2\}_n$	19	[15]
PHPP	11	[22]

Among these compounds, the adsorption capacity of the  $\{[\text{Hg}(\text{L})](\text{Cl}_2)(\text{CH}_3\text{CN})_2\}_n$  (**Hg-CP**) against cationic RhB dye was found to be 18.14 mg/g in pH 3 media and 4.89 mg/g in pH 6 media in this study. The same compound showed 19.2 mg/g dye adsorption capacity against the cationic MB dye in a pH 6 environment in our previous work. From the results, it can be said that the compound has a higher ability to adsorb against MB dye than RhB.

#### 4. Conclusion

In this study, it was investigated whether **Hg-CP**, which we synthesised in our previous study, could adsorb or not RhB dye. Adsorption studies were performed in two different pH environments: pH = 6, which is the natural pH of **Hg-CP** in water, and pH = 3, which is a more acidic medium. The results show that the dye adsorption capacity of **Hg-CP** increases from 4.89 mg/g to 18.14 mg/g when the pH value decreases from 6 to 3. 81% of the RhB is removed from the solution of **Hg-CP** in pH 3 media. Also, it was found that **Hg-CP** could selectively adsorb RhB dye with an adsorption capacity of 15.45 mg/g from the RhB/MO dye mixture. This experiment was carried out under these conditions because the adsorption result for RhB was higher in the pH = 3 medium. The surface charge values of **Hg-Cp** (before adsorption and after adsorption) obtained from zeta potential measurements support the adsorption experiment results. According to the PXRD results, Hg-CP used as an adsorbent saved its structure after the adsorption. As a result, the pH change increased the adsorption of the cationic RhB dye, and the surface charges played an important role on the adsorption phenomena.

#### Acknowledgments

This work has been supported by The Scientific and Technological Research Council of Turkey (TUBITAK) (Project number 121Z236).

#### Author's Contributions

**Afranur Pendar:** Synthesing and UV Vis Experiments

**Derya Davarci:** Supervised the progress of the experiment, the interpretation of the results, drafted the manuscript.

#### Ethics

There is no ethical problem regarding the publication of this manuscript.

#### References

- [1]. Bureekaew S, Shimomura S, Kitagawa S. 2008. Chemistry and application of flexible porous coordination polymers. *Science and Technology of Advanced Materials*.
- [2]. Kurmoo M. 2009. Magnetic metal-organic frameworks. *Chemical Society Reviews*, 38:5: 1353-1379.
- [3]. Zhang X, Wang W, Hu Z, Wang G, Uvdal K. 2015. Coordination polymers for energy transfer: Preparations, properties, sensing applications, and perspectives. *Coordination Chemistry Reviews*, 284: 206-235.
- [4]. Liu JQ, Luo ZD, Pan Y, Singh AK, Trivedi M, Kumar A. 2020. Recent developments in luminescent coordination polymers: Designing strategies, sensing application and theoretical evidence. *Coordination chemistry reviews*, 406: 213145.
- [5]. Janiak, C. 2003. Engineering coordination polymers towards applications. *Dalton Transactions*, 14: 2781-2804.
- [6]. Davarci D, Duyar C, Zorlu Y. 2023. 3D Ag (I) coordination polymer constructed from a flexible pyridyloxycyclotriphosphazene linker: Synthesis, crystal structure and dye adsorption properties. *Polyhedron*, 231: 116250.
- [7]. Karmakar A, Paul A, Santos IRM, Santos PMR, Sabatini EP, Gurbanov AV, Guedes da Silva MFC, Pombeiro AJL. 2022. Highly efficient adsorptive removal of organic dyes from aqueous solutions using polyaromatic group-containing Zn(II)-based coordination polymers. *Cryst. Growth Des.* 22: 2248–2265.
- [8]. Zhuang Y, Zhua Q, Lia G, Wanga Z, Zhana P, Renb C, Sia Z, Li S, Caia D, Qinb P. 2022. Photocatalytic degradation of organic dyes using covalent triazine-based framework. *Mater. Res. Bull.* 146: 111619.
- [9]. Jain R, Mathur M, Sikarwar S, Mittal A. 2007. Removal of the hazardous dye rhodamine B through photocatalytic and adsorption treatments, *J. Environ. Manage.*, 85: 956-964.
- [10]. Jeevananthan V, Thangavelu SAG, Loganathan P, Shanmugan S. 2021. Multisite coordination ligands on cyclotriphosphazene core for the assembly of metal clusters and porous coordination polymers. *ChemistrySelect* 6(7): 1478-1507.
- [11]. Narayanan, RS, and Chandrasekhar V. 2016. Molecular, 1D and 2D assemblies from hexakis (3-pyridyloxy) cyclophosphazene containing 20-membered metallamacrocyclic motifs." *Dalton Transactions* 45(5):2273-2283.
- [12]. Davarci D, Gür R, Beşli S, Şenkuytu E, Zorlu Y. 2016. Silver (I) coordination polymers assembled from flexible cyclotriphosphazene ligand: structures, topologies, and investigation of the counteranion effects. *Acta Crystallographica Section B: Structural Science, Crystal Engineering and Materials*, 72(3): 344-356.
- [13]. Davarci D, Zorlu Y. 2017. Group 12 metal coordination polymers built on a flexible hexakis (3-pyridyloxy) cyclotriphosphazene ligand: Effect of the central metal ions on the construction of coordination polymers. *Polyhedron*, 127: 1-8.
- [14]. Duyar C, Pendar A, Bektaş N, Zorlu Y, Davarci D. 2023. 2D and 3D Ag (I) coordination polymers with a 2-methylimidazole substituted cyclotriphosphazene ligand: Structures and dye adsorption properties. *Polyhedron*, 244: 116589.
- [15]. Pendar A, Duyar C, Zorlu Y, Davarci D., 2023. Ag(I) and Hg(II) Coordination Polymers Decorated from Fully Benzimidazole Substituted Cyclotriphosphazene Ligand and Adsorption Behaviour Against Methylene Blue, *Journal of Inorganic and Organometallic Polymers and Materials*, (doi: 10.1007/s10904-023-02949-6)
- [16]. Erkovan AO, Seifi A, Aksoy BT, Zorlu Y, Khataee A, Çoşut B. 2023. Catalytic Activity of Zn (II) Coordination Polymer Based on a Cyclotriphosphazene-Functionalized Ligand for Removal of Organic Dyes. *Catalysts*, 13(4): 756.
- [17]. Morsali A, Masoomi MY. 2009. Structures and properties of mercury (II) coordination polymers. *Coordination Chemistry Reviews*, 253(13-14):1882-1905.
- [18]. Xiong, G., Gao, S., Zhang, Q., Ren, B., You, L., Ding, F., Sun, Y. 2022. High porosity cyclotriphosphazene-based hyper-crosslinked polymers as efficient cationic dye MB adsorbents. *Polymer*, 247, 124787.
- [19]. Wang, Y., Soldatov, M., Wang, Q., & Liu, H. 2021. Phosphazene functionalized silsesquioxane-based porous polymers for absorbing I<sub>2</sub>, CO<sub>2</sub> and dyes. *Polymer*, 218, 123491.
- [20]. Zou, J., Liao, K., Xiang, L., Liu, M., Xie, F., Liu, X., Wang, Y. 2020. Synthesis of poly (cyclotriphosphazene-co-4, 4'-



diaminodiphenylsulfone) microspheres and their adsorption properties for cationic dyes (methylene blue). *Journal of Inorganic and Organometallic Polymers and Materials*, 30, 976-985.

[21]. Chen, Z., Fu, J., Wang, M., Wang, X., Zhang, J., & Xu, Q. 2014. Adsorption of cationic dye (methylene blue) from aqueous solution using poly (cyclotriphosphazene-co-4, 4'-sulfonyldiphenol) nanospheres. *Applied Surface Science*, 289, 495-501.

[22]. Wang, Y., Yang, N., Soldatov, M., & Liu, H. 2022. A novel phosphazene-based amine-functionalized porous polymer with high adsorption ability for I<sub>2</sub>, dyes and heavy metal ions. *Reactive and Functional Polymers*, 173, 105235.

[23]. Huang J-H, Huang K-L, Liu S-Q, Wang A-T, Yan C. 2008. Adsorption of Rhodamine B and methyl orange on a hypercrosslinked polymeric adsorbent in aqueous solution, *Colloids and Surfaces A: Physicochemical and Engineering Aspects*, 330 (1): 55-61.